PETROVIETNAM JOURNAL

An Official Publication of The Vietnam National Oil and Gas Group Vol 6 - 2012

ISSN-0866-854X

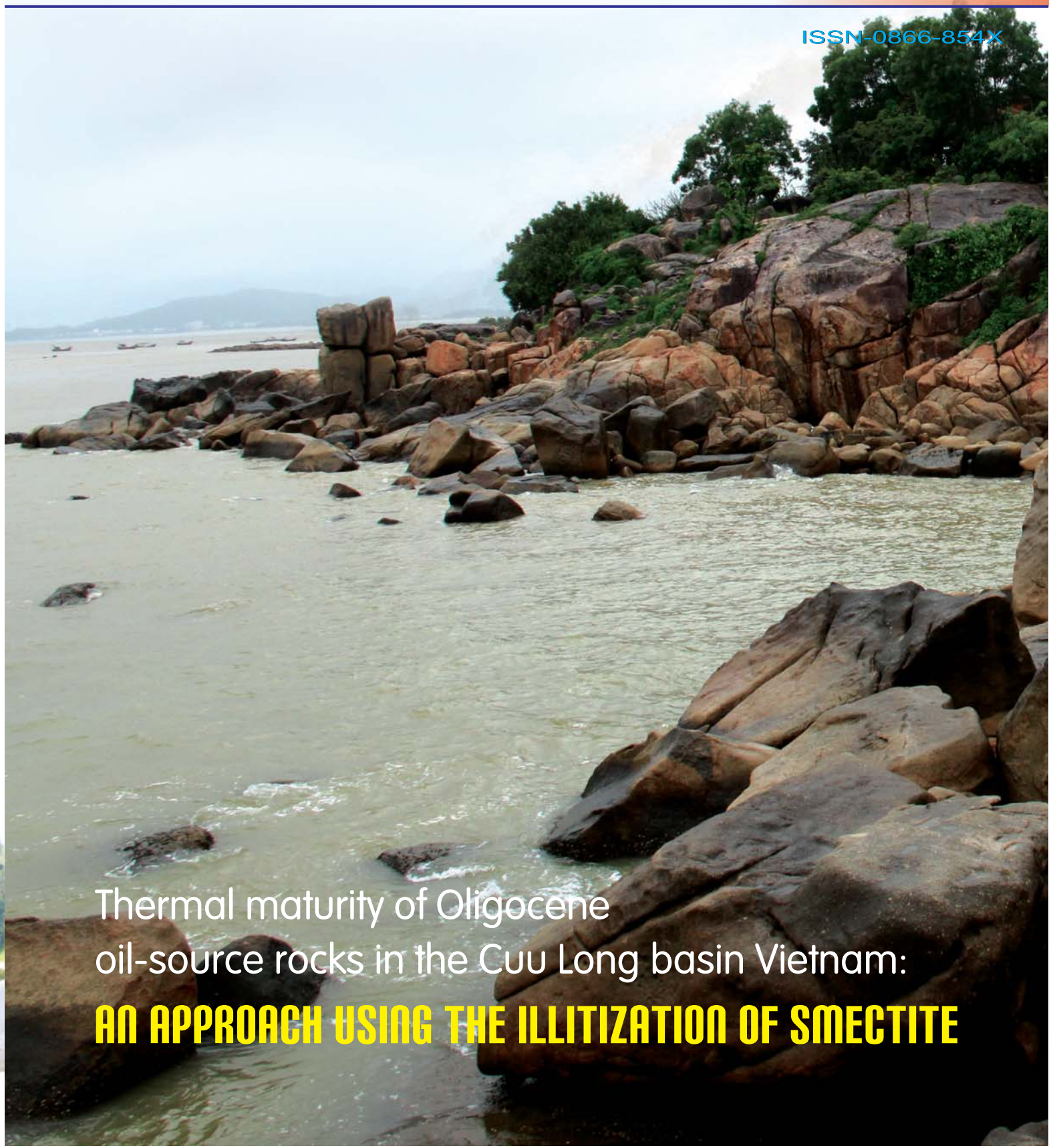

Thermal maturity of Oligocene oil-source rocks in the Cuu Long basin Vietnam: AN APPROACH USING THE ILLITIZATION OF SMECTITE

PETROVIETNAM JOURNAL IS PUBLISHED MONTHLY BY VIETNAM NATIONAL OIL AND GAS GROUP

PETROVIETNAM JOURNAL

Editor-in-chief
Dr. Sc. Phung Dinh Thuc

Deputy Editor-in-chief
Dr. Nguyen Van Minh
Dr. Phan Ngoc Trung
Dr. Vu Van Vien

Editorial Board Members
Dr. Sc. Lam Quang Chien
Dr. Hoang Ngoc Dang
Dr. Nguyen Minh Dao
BSc. Vu Khanh Dong
Dr. Nguyen Anh Duc
MSc. Tran Hung Hien
Dr. Vu Thi Bich Ngoc
MSc. Le Ngoc Son
MSc. Nguyen Van Tuan
Dr. Le Xuan Ve
Dr. Phan Tien Vien
Dr. Nguyen Tien Vinh
Dr. Nguyen Hoang Yen

Secretary
MSc. Le Van Khoa
BSc. Nguyen Thi Viet Ha

Contact Address
16th Floor, VPI Tower, Trung Kinh Street,
Yen Hoa Ward, Cau Giay District, Ha Noi
Tel: (+84-04) 37727108
Fax: (+84-04) 37727107
Email: tapchidk@vpi.pvn.vn
Mobile: 0982288671

Designed by
Le Hong Van

Cover photo: Outcrop of fractured granite basement - Hòn Chồng (Nha Trang, Khanh Hoa, Vietnam). Photo: Van Khoa

Publishing Licences No. 170/GP - BVHTT dated 24/04/2001; No. 20/GP - SĐBS dated 01/07/2008

PETROVIETNAM JOURNAL

Contents

SCIENTIFIC & TECHNOLOGICAL PAPERS

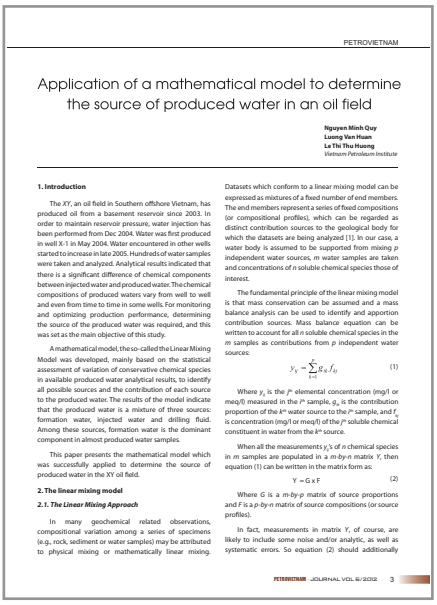

PETROVIETNAM

Application of a mathematical model to determine the source of produced water in an oil field

Nguyen Minh Quy
Luong Van Huan
Le Thi Thu Huong
Vietnam Petroleum Institute

1. Introduction

The XY, an oil field in Southern offshore Vietnam, has produced oil from a basement reservoir since 2003. In order to maintain reservoir pressure, water injection has been performed from Dec 2004. Water was first produced in well X-1 in May 2004. Water encountered in other wells started to increase in late 2005. Hundreds of water samples were taken and analyzed. Analytical results indicated that there is a significant difference of chemical components between injected water and produced water. The chemical compositions of produced waters vary from well to well and even from time to time in some wells. For monitoring and optimizing production performance, determining the source of the produced water was required, and this was set as the main objective of this study.

A mathematical model, the so-called the Linear Mixing Model was developed, mainly based on the statistical assessment of variation of conservative chemical species in available produced water analytical results, to identify all possible sources and the contribution of each source to the produced water. The results of the model indicate that the produced water is a mixture of three sources: formation water, injected water and drilling fluid. Among these sources, formation water is the dominant component in almost produced water samples.

This paper presents the mathematical model which was successfully applied to determine the source of produced water in the XY oil field.

2. The linear mixing model

2.1. The Linear Mixing Approach

In many geochemical related observations, compositional variation among a series of specimens (e.g., rock, sediment or water samples) may be attributed to physical mixing or mathematically linear mixing. Datasets which conform to a linear mixing model can be expressed as mixtures of a fixed number of end members. The end members represent a series of fixed compositions (or compositional profiles), which can be regarded as distinct contribution sources to the geological body for which the datasets are being analyzed [1]. In our case, a water body is assumed to be supported from mixing p independent water sources, m water samples are taken and concentrations of n soluble chemical species those of interest.

The fundamental principle of the linear mixing model is that mass conservation can be assumed and a mass balance analysis can be used to identify and apportion contribution sources. Mass balance equation can be written to account for all n soluble chemical species in the m samples as contributions from p independent water sources:

$$y_{iy} = \sum_{k=1}^{p} g_{ik} f_{ky} \quad (1)$$

Where y_{iy} is the i^{th} elemental concentration (mg/l or meq/l) measured in the i^{th} sample, g_{ik} is the contribution proportion of the k^{th} water source to the i^{th} sample, and f_{ky} is concentration (mg/l or meq/l) of the i^{th} soluble chemical constituent in water from the k^{th} source.

When all the measurements y_{iy}'s of n chemical species in m samples are populated in a m-by-n matrix Y, then equation (1) can be written in the matrix form as:

$$Y = G \times F \quad (2)$$

Where G is a m-by-p matrix of source proportions and F is a p-by-n matrix of source compositions (or source profiles).

In fact, measurements in matrix Y, of course, are likely to include some noise and/or analytic, as well as systematic errors. So equation (2) should additionally

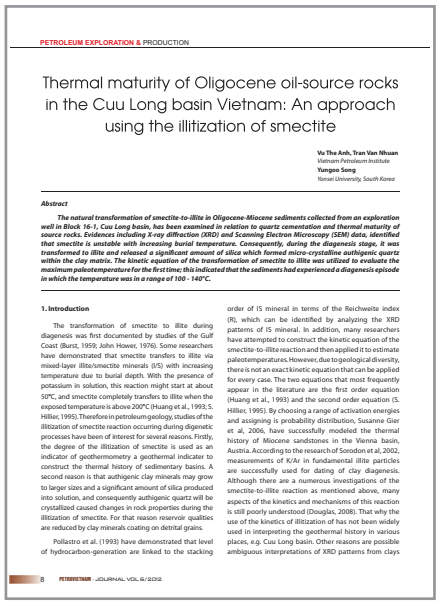

PETROLEUM EXPLORATION & PRODUCTION

Thermal maturity of Oligocene oil-source rocks in the Cuu Long basin Vietnam: An approach using the illitization of smectite

Vu The Anh, Tran Van Nhuan
Vietnam Petroleum Institute
Yungoo Song
Yonsei University, South Korea

Abstract

The natural transformation of smectite-to-illite in Oligocene-Miocene sediments collected from an exploration well in Block 16-1, Cuu Long basin, has been examined in relation to quartz cementation and thermal maturity of source rocks. Evidences including X-ray diffraction (XRD) and Scanning Electron Microscopy (SEM) data, identified that smectite is unstable with increasing burial temperature. Consequently, during the diagenesis stage, it was transformed to illite and released a significant amount of silica which formed micro-crystalline authigenic quartz within the clay matrix. The kinetic equation of the transformation of smectite to illite was utilized to evaluate the maximum paleotemperature for the first time; this indicated that the sediments had experienced a diagenesis episode in which the temperature was in a range of 100 - 140°C.

1. Introduction

The transformation of smectite to illite during diagenesis was first documented by studies of the Gulf Coast (Burst, 1959; John Hower, 1976). Some researchers have demonstrated that smectite transfers to illite via mixed-layer illite/smectite minerals (I/S) with increasing temperature due to burial depth. With the presence of potassium in solution, this reaction might start at about 50°C, and smectite completely transfers to illite when the exposed temperature is above 200°C (Huang et al., 1993; S. Hillier, 1995). Therefore in petroleum geology, studies of the illitization of smectite reaction occurring during digenetic processes have been of interest for several reasons. Firstly, the degree of the illitization of smectite is used as an indicator of geothermometry a geothermal indicater to construct the thermal history of sedimentary basins. A second reason is that authigenic clay minerals may grow to larger sizes and a significant amount of silica produced into solution, and consequently authigenic quartz will be crystallized caused changes in rock properties during the illitization of smectite. For that reason reservoir qualities are reduced by clay minerals coating on detrital grains.

Pollastro et al. (1993) have demonstrated that level of hydrocarbon-generation are linked to the stacking order of I/S mineral in terms of the Reichweite index (R), which can be identified by analyzing the XRD patterns of I/S mineral. In addition, many researchers have attempted to construct the kinetic equation of the smectite-to-illite reaction and then applied it to estimate paleotemperatures. However, due to geological diversity, there is not an exact kinetic equation that can be applied for every case. The two equations that most frequently appear in the literature are the first order equation (Huang et al., 1993) and the second order equation (S. Hillier, 1995). By choosing a range of activation energies and assigning is probability distribution, Susanne Gier et al, 2006, have successfully modeled the thermal history of Miocene sandstones in the Vienna basin, Austria. According to the research of Sorodon et al, 2002, measurements of K/Ar in fundamental illite particles are successfully used for dating of clay diagenesis. Although there are a numerous investigations of the smectite-to-illite reaction as mentioned above, many aspects of the kinetics and mechanisms of this reaction is still poorly understood (Douglas, 2008). That why the use of the kinetics of illitization of has not been widely used in interpreting the geothermal history in various places, e.g. Cuu Long basin. Other reasons are possible ambiguous interpretations of XRD patterns from clays

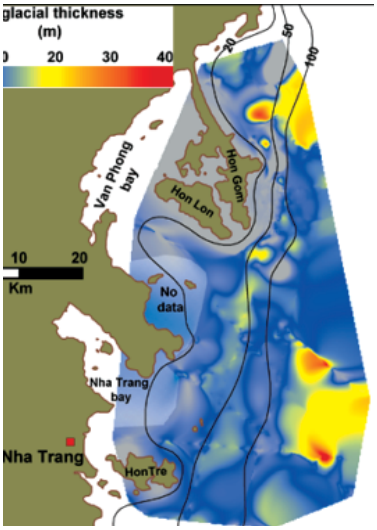

16 ◆ Late Pleistocene - Holocene seismic stratigraphy of Nha Trang Shelf, Central Vietnam

27 ◆ The Vietnam carbon dioxide storage capacity

31 ◆ The 4D Experience in TOTAL

36 ◆ Numerical simulation of bottomhole flow filed of PDC bit with side nozzles

40 ◆ Contributions of Acid and Metal Sites to Propane Aromatisation over Fresh Ga, H-ZSM-5 Catalyst

46 ◆ Synthesis of some dibenzothiophene-derived sulfur compounds

50 ◆ In situ XANES studies of Titanium sites and their reactivities in nanoporous Titanosilicate frameworks

58 ◆ A two-phase model for the development of positive surface discharge in air

70 ◆ The impact of biorhythms in safety management in Vietsovpetro

NEWS

72 ◆ Vietnam, Peru, Venezuela boost energy cooperation

73 ◆ *World Gas Conference 2012:* Gas sustaining future global growth

74 ◆ PVEP expands operations in South America

75 ◆ Successful load-out Vietnam's largest jacket

Application of a mathematical model to determine the source of produced water in an oil field

Nguyen Minh Quy
Luong Van Huan
Le Thi Thu Huong
Vietnam Petroleum Institute

1. Introduction

The *XY*, an oil field in Southern offshore Vietnam, has produced oil from a basement reservoir since 2003. In order to maintain reservoir pressure, water injection has been started from Dec 2004. Water was first appeared in produced fluid from the well X-1 in May 2004. Water encountered in other wells started to increase in late 2005. Hundreds of water samples were taken and analyzed. Analytical results indicated that the chemical compositions of produced waters vary from well to well and even from time to time in some wells. For monitoring and optimizing production performance, determining the source of the produced water was required, and this was set as the main objective of this study.

A mathematical model, the so-called the Linear Mixing Model was developed, mainly based on the statistical assessment of variation of conservative chemical species in available produced water analytical results, to identify all possible sources and the contribution of each source to the produced water. The results of the model indicate that the produced water is a mixture of three sources: formation water, injected water and drilling fluid. Among these sources, formation water is the dominant component in almost produced water samples.

This paper presents the mathematical model which was successfully applied to determine the source of produced water in the XY oil field.

2. The linear mixing model

2.1. The Linear Mixing Approach

In many geochemical related observations, compositional variation among a series of specimens (e.g., rock, sediment or water samples) may be attributed to physical mixing or mathematically linear mixing. Datasets which conform to a linear mixing model can be expressed as mixtures of a fixed number of end members. The end members represent a series of fixed compositions (or compositional profiles), which can be regarded as distinct contribution sources to the geological body for which the datasets are being analyzed [1]. In our case, a water body is assumed to be supported from mixing *p* independent water sources, *m* water samples are taken and concentrations of *n* soluble chemical species are those of interest.

The fundamental principle of the linear mixing model is that mass conservation can be assumed and a mass balance analysis can be used to identify and apportion contribution sources. Mass balance equation can be written to account for all *n* soluble chemical species in the *m* samples as contributions from *p* independent water sources:

$$y_{ij} = \sum_{k=1}^{p} g_{ik} f_{kj} \quad (1)$$

Where y_{ij} is the j^{th} elemental concentration (mg/l or meq/l) measured in the i^{th} sample, g_{ik} is the contribution proportion of the k^{th} water source to the i^{th} sample, and f_{kj} is concentration (mg/l or meq/l) of the j^{th} soluble chemical constituent in water from the k^{th} source.

When all the measurements y_{ij}'s of *n* chemical species in *m* samples are populated in a *m-by-n* matrix *Y*, then equation (1) can be written in the matrix form as:

$$Y = G \times F \quad (2)$$

Where *G* is a *m-by-p* matrix of source proportions and *F* is a *p-by-n* matrix of source compositions (or source profiles).

In fact, measurements in matrix *Y*, of course, are likely to include some noise and/or analytic, as well as systematic errors. So equation (2) should additionally

include an error term *E* (a *m-by-n* matrix), then equation (2) can be rewritten as:

$$Y = G \times F + E \quad (3)$$

There exist a set of natural physical constraints on the solution that must be considered in developing any model for identifying and apportioning the sources of water contribution. The fundamental, natural physical constraints that must be obeyed are:

- The original data must be reproduced by the model; this means the error term *E* must be minimized and values in the matrix *E* would be distributed in certain and explainable patterns.

$$minimize \left\|E\right\|^2 \quad (4)$$

- All values in matrices *G* and *F* must be non-negative; a water source cannot have a negative concentration of chemical species or a water source cannot contribute negative proportions to any water sample.

$$G \geq 0 \text{ and } F \geq 0 \quad (5)$$

- When all possible water sources are taken into account, the sum of source proportion contributions to each water sample must be constant (e.g. equal to unit or a hundred percent).

$$sum(G) = 100\% \quad (6)$$

It is assumed that the concentrations of a series of chemical species have been measured for a set of samples from the water body so that the matrix *Y* is always known. If the number of sources *p* that contribute to those water samples can be identified and their compositional profiles measured, then only the contributions of the sources to each sample need to be determined. These calculations are generally made without much difficulty, using standard linear equation or more effective alternatives, such as non-negative least-square techniques [2].

There is situation in which the chemical composition of the water body is believed to have been produced by mixing from some water sources, but the number of water sources and their chemical composition are unknown. In this case, the objective of the linear mixing modeling is to determine the number of water sources *p*, the chemical profile of each water source and the proportion that each of the *p* sources contributes to each water sample. Recasting the chemical compositions of water samples into a linear mixing model in the absence of *a priori* knowledge about the water sources requires a solution of the bilinear (or explicit) mixing problem. The multivariate data analysis methods that are used to solve this problem are generally referred to as factor analysis.

2.2. Principal Component Analysis (PCA)

The conventional approach to solve the bilinear mixing problem is the most common form of factor analysis named Principal Components Analysis (PCA). This method is generally calculated using an eigenvector analysis of a correlation matrix.

The matrix *Y* can always be defined in terms of the *singular value decomposition*.

$$Y = U \times S \times V' \quad (7)$$

Characteristics of singular value decomposition are that: *U* and *V* matrix are orthogonal, and singular values *S* are always ordered so that those with the largest variation come first. When only the first *p* columns of the *U* and *V* matrices and the first *p* values of *S* are take into account, which are denoted as $\overline{U}$, $\overline{V}$ and $\overline{S}$ respectively, and an error terms *E* is added, then equation (7) will be:

$$Y = \overline{U} \times \overline{S} \times \overline{V} + E \quad (8)$$

Error matrix *E* represents the part of the data variance un-modeled by the linear mixing model with *p* factors. It can be shown [2] that the first term on the right side of equation (8) estimates *Y* in the least-squares sense that it gives the lowest possible value for $\left\|E\right\|^2$ when the data matrix *Y* is approximated by the linear mixing model with *p* factors.

Equation (8) is a mathematically feasible solution for the bilinear mixing problem which was addressed in equation (3). The problem can be solved, but it does not produce an *unique* solution. It is always possible to include a transformation into the equation:

$$Y = G \times T \times T^{-1} \times F \quad (9)$$

where *T* is one of the potential infinity of transformation matrices. This transformation is called a rotation and is generally included in order to produce factors that appear to be closer to physically real source profiles.

In fact, *G* and *F* are usually consisting of many negative values. However, the rotation matrix T cannot, in most cases, eliminate all negativity in *G* and *F*, and constant-sum constraints (6) is hardly satisfied in customary PCA.

2.3. Matrix Factorization with Non-Negativity and Constant-Sum Constraints

There are various approaches available to impose nonnegativity constraints in factor analysis. One of the alternatives for positive matrix factorization is Lee and Seung's Euclidean Update algorithm which is preferably called Non-Negativity Matrix Factorization (NNMF). This algorithm is preferred because it is rather clear, simple easily computable, but more important is of its guarantee of convergence, although it is somehow expensive in CPU time [3].

This algorithm minimize *Euclidean distance* $\| X - GF \|^2$ with respect to *G* and *F*, subject to the constraints $G, F \geq 0$.

- *G* and *F* are initialized to be two random non-negative matrices or two roughly-estimated matrices.

- *G* and *F* are continuously kept updating until $\| X - GF \|^2$ converges. The multiplicative update rules are as the following:

$$F_{a\mu} = F_{a\mu} \frac{(G^T X)_{a\mu}}{(G^T GF)_{a\mu}}, \; G_{ia} = G_{ia} \frac{(XF^T)_{ia}}{(G^T FF^T)_{ia}} \quad (10)$$

This means that each element of *F* is multiplied by corresponding element of matrix G^TX then divided by corresponding element of matrix G^TGF.

During the above updates, *G* will be updated column-wise while *F* will be updated row-wise, and *G* and *F* should be "simultaneously" updated. This means, after updating one row of *F*, the corresponding column of *G* needs to be updated subsequently; so actually we update *F* and *G* alternately.

The whole algorithm scheme of this *NNMF* model is given out in Fig. 1. Updating elements of *G* and *F* in each iteration is carried out in the inner loop, while calculating *Euclidean distance* $\| X - GF \|^2$ and checking criteria of its convergence is carried out in the outer loop.

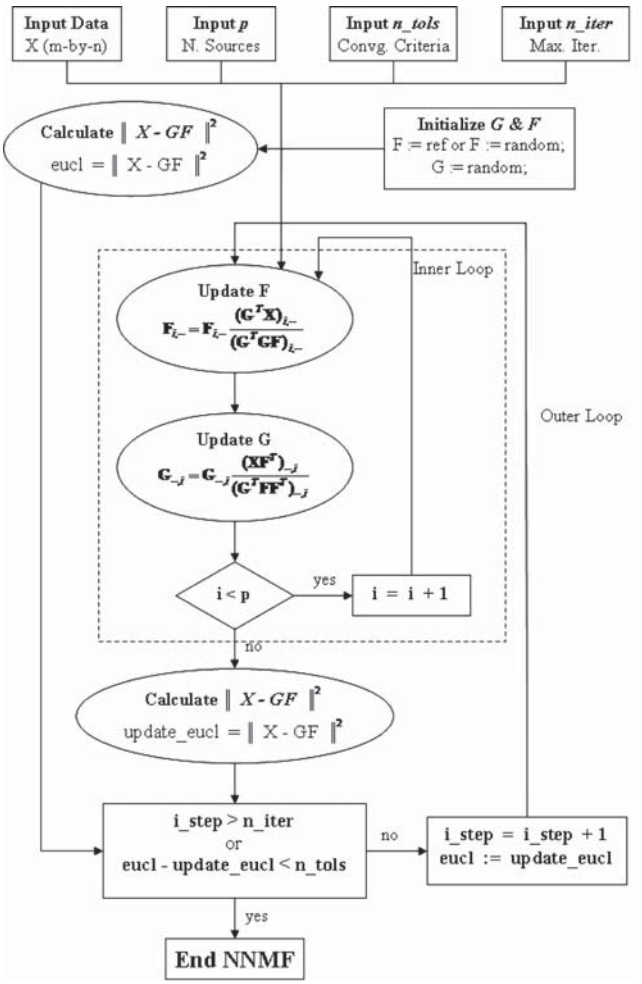

Fig. 1. *Algorithm Scheme of Lee and Seung's NNMF*

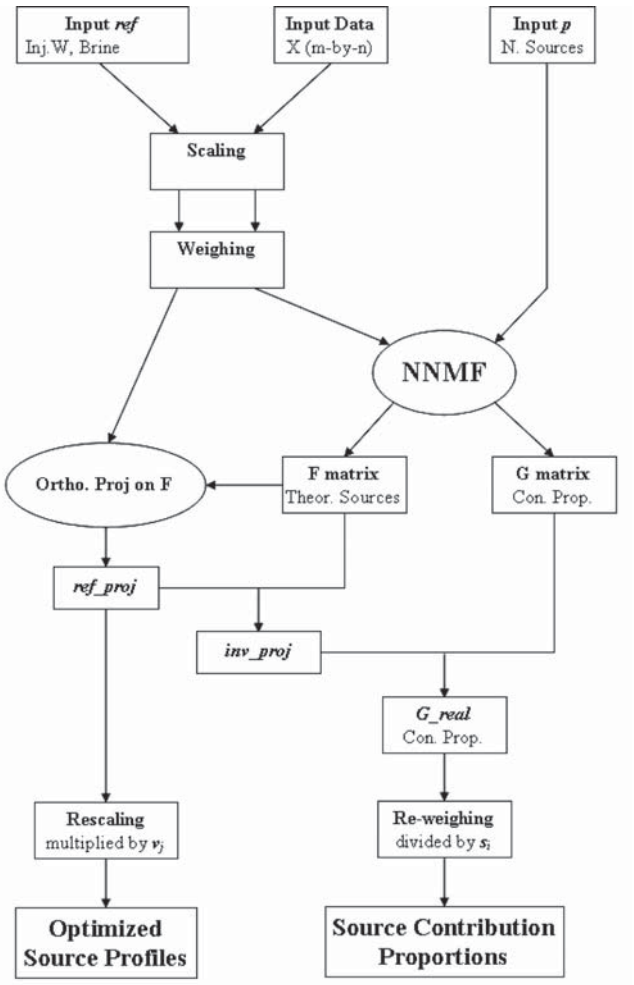

Fig. 2. *Outline of Source Unmixing Calculation*

3. Computations for produced water of XY field

3.1. Preparing Data Input

The water-rock physico-chemical interaction was conducted and the results showed that: there are 5 chemical components including bromide, chlorite, sulfate, sodium and total ion which are necessarily stable in the *XY* basement reservoir and are considered as conservative components or chemical "fingerprints" to clarify the contribution of each water source to produced water. Chemical data of produced waters are assembled into a matrix X, samples are arranged row-wise, and parameters are arranged column-wise. A total number of 177 produced water samples were taken in to account so data matrix will have 177 rows and 5 columns.

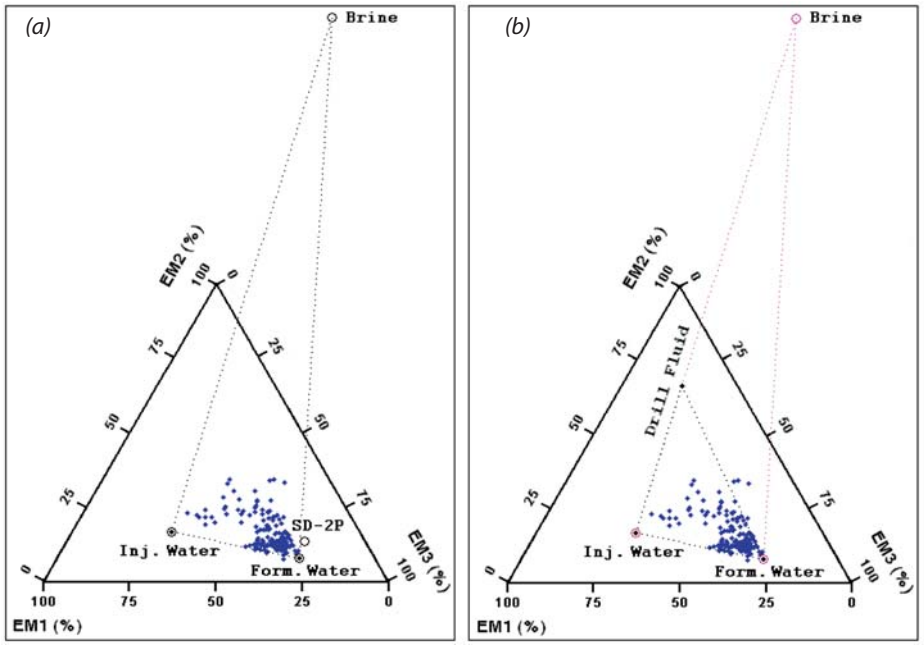

Fig. 3. *Expression of produced water as mixtures of mathematical EMs*

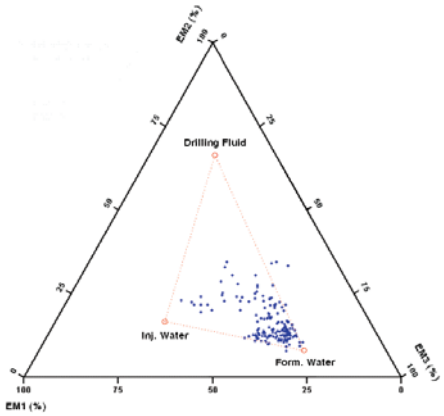

Fig. 4. *Positions of realistic end-members in space of mathematical EMs*

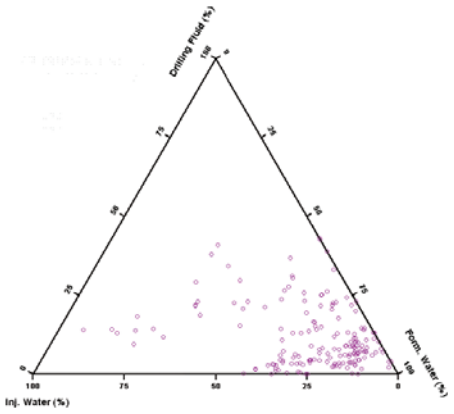

Fig. 5. *Expression of produced water as mixtures of water sources*

3.2. Computational Scheme

Input data, after eliminating extremely eliminating, scaling and/or weighting, are assembled in matrix *X* (177-by-5), including 177 produced water samples and 5 chemical parameters. This input matrix is trained in a computational process in which an outline of the computational scheme is given in Fig. 2.

3.3. Computational Output

In this study, the computation process was optimized with three water sources. The PMF computation produced three mathematical profiles (EM1-3), the expressions of all water samples, injected water, brine and formation water sample as mixtures of these 3 mathematical profiles are represented in Fig. 3b. The representations of produced water samples by these mathematical profiles show a clear acute angle at formation water. This clue indicates that all produced water samples are actually mixtures of 3 realistic water sources with unique chemical profiles.

Initially, it is believed that produced water is mixing from formation water, injected water and brine, but computational results show that no produced water sample is distributed in the large area spreading from the brine position (Fig. 3b). Moreover, there exists also a clear upper edge of the acute angle from the optimized position of formation water. This evidence allows the conclusion that produced water was mixed from an intermediate composition between brine and injected water (sea water) rather than directly from a pure brine composition. This intermediate composition, so-called *drilling fluid*, is positioned in the line from brine to injected water and its position, as shown in Fig. 3b, can be determined by

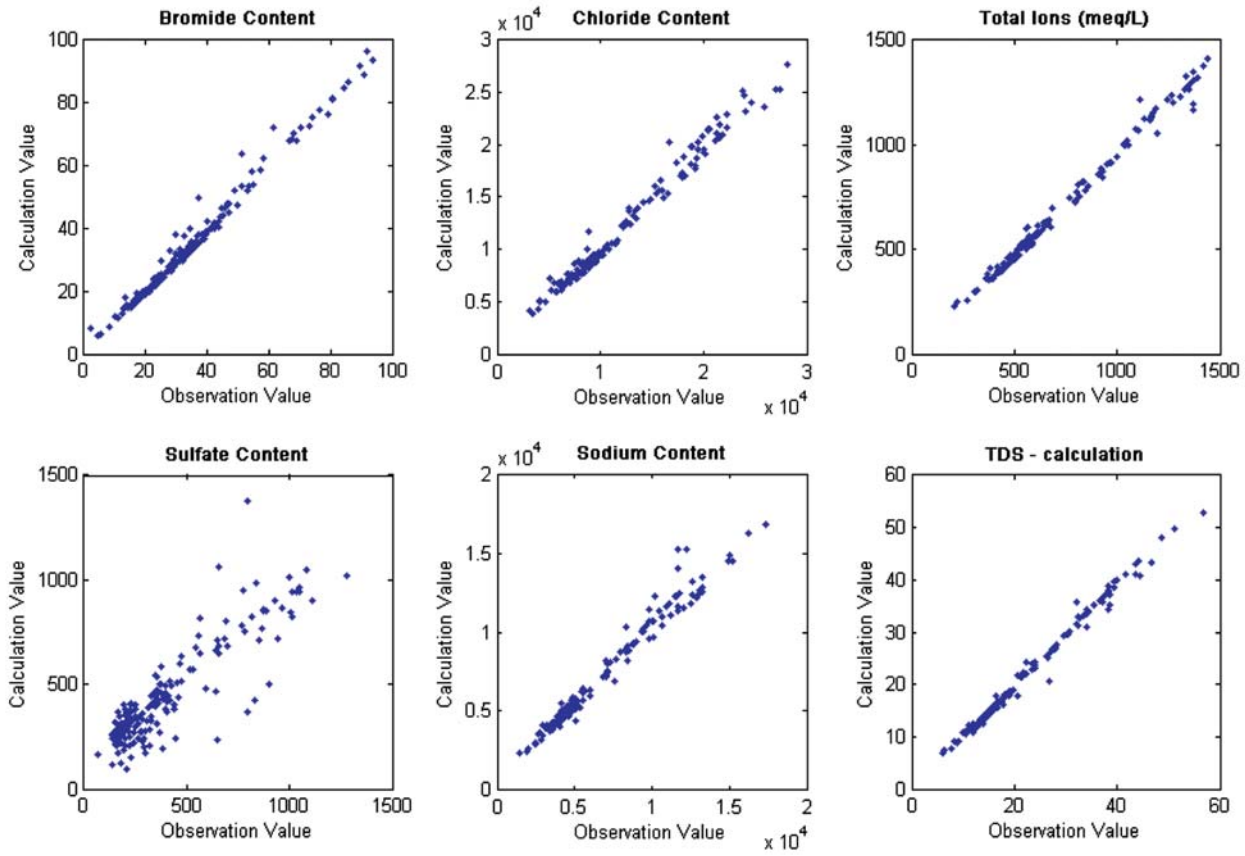

Fig. 6. *Calculation versus Observation of Chemical Components*

convexity optimization. The convexity optimization gives a proportion of 28.7% brine in drilling fluid. This value is agreeable with the proportion of about 30% brine in total mudlosses which include brine and seawater.

Finally, three realistic end-members which contribute to produced water are positioned in the mixing space of three mathematical end-members as shown in Fig. 4. It can be realized that all produced water samples and their natural trends, including acute angle and sharp edges, are enclosed well by three realistic end-members. A spatial base transformation or rotation to these realistic end-members will give the expressions of all produced water samples as mixtures of three realistic water sources as shown in Fig. 5.

In order to validate the model, an inverting model was performed. The recalculated values of chemical components of water samples obtained by the inverting model are in good agreement with the observation as shown in Fig. 6.

Conclusions

In summary, all computational results have definitely confirmed the appropriateness and accuracy of applying a linear mixing model to identify water sources and their contributions to produced water. The results of the model indicate that the produced water is a mixture of three sources: formation water, injected water and drilling fluid. Among these sources, formation water is the dominant component in almost all produced water samples.

The application of the mathematical models is the fundamental factor for the success of this study.

References

1. Weltje, G. J. *End-member modeling of compositional data: numerical-statistical algorithms for solving the explicit mixing problem*. Journal of Mathematical Geology. 1997; Vol. 29: p. 503 - 549.

2. Lawson, C.L. and Hanson, R.J. *Solving Least Squares Problems*. Prentice-Hall Press. 1974.

3. Lee, D.D. and Seung, H.S. *Algorithms for nonnegative matrix factorization, in Advances in Neural Information Processing 13*. MIT Press. 2001: p. 556 - 562.

Thermal maturity of Oligocene oil-source rocks in the Cuu Long basin Vietnam: An approach using the illitization of smectite

Vu The Anh, Tran Van Nhuan
Vietnam Petroleum Institute
Yungoo Song
Yonsei University, South Korea

Abstract

The natural transformation of smectite-to-illite in Oligocene-Miocene sediments collected from an exploration well in Block 16-1, Cuu Long basin, has been examined in relation to quartz cementation and thermal maturity of source rocks. Evidences including X-ray diffraction (XRD) and Scanning Electron Microscopy (SEM) data, identified that smectite is unstable with increasing burial temperature. Consequently, during the diagenesis stage, it was transformed to illite and released a significant amount of silica which formed micro-crystalline authigenic quartz within the clay matrix. The kinetic equation of the transformation of smectite to illite was utilized to evaluate the maximum paleotemperature for the first time; this indicated that the sediments had experienced a diagenesis episode in which the temperature was in a range of 100 - 140°C.

1. Introduction

The transformation of smectite to illite during diagenesis was first documented by studies of the Gulf Coast (Burst, 1959; John Hower, 1976). Some researchers have demonstrated that smectite transfers to illite via mixed-layer illite/smectite minerals (I/S) with increasing temperature due to burial depth. With the presence of potassium in solution, this reaction might start at about 50°C, and smectite completely transfers to illite when the exposed temperature is above 200°C (Huang et al., 1993; S. Hillier, 1995). Therefore in petroleum geology, studies of the illitization of smectite reaction occurring during digenetic processes have been of interest for several reasons. Firstly, the degree of the illitization of smectite is used as an indicator of geothermometry a geothermal indicater to construct the thermal history of sedimentary basins. A second reason is that authigenic clay minerals may grow to larger sizes and a significant amount of silica produced into solution, and consequently authigenic quartz will be crystallized caused changes in rock properties during the illitization of smectite. For that reason reservoir qualities are reduced by clay minerals coating on detrital grains.

Pollastro et al. (1993) have demonstrated that level of hydrocarbon-generation are linked to the stacking order of IS mineral in terms of the Reichweite index (R), which can be identified by analyzing the XRD patterns of IS mineral. In addition, many researchers have attempted to construct the kinetic equation of the smectite-to-illite reaction and then applied it to estimate paleotemperatures. However, due to geological diversity, there is not an exact kinetic equation that can be applied for every case. The two equations that most frequently appear in the literature are the first order equation (Huang et al., 1993) and the second order equation (S. Hillier, 1995). By choosing a range of activation energies and assigning is probability distribution, Susanne Gier et al, 2006, have successfully modeled the thermal history of Miocene sandstones in the Vienna basin, Austria. According to the research of Sorodon et al, 2002, measurements of K/Ar in fundamental illite particles are successfully used for dating of clay diagenesis. Although there are a numerous investigations of the smectite-to-illite reaction as mentioned above, many aspects of the kinetics and mechanisms of this reaction is still poorly understood (Douglas, 2008). That why the use of the kinetics of illitization of has not been widely used in interpreting the geothermal history in various places, e.g. Cuu Long basin. Other reasons are possible ambiguous interpretations of XRD patterns from clays

containing a mixture of discrete clay minerals and mixed-layer phases.

Located in offshore Southern Vietnam, the Cuu Long basin is a typical rift basin, overlying heavily weathered Mesozoic basement (granites and granodiorites). The sedimentary succession consists of a Palaeogene syn-rift package different from a Neogene post-rift succession by an inversion unconformity of latest Oligocene to early Miocene age (Jørgen A. Bojesen-Koefoed, 2009). The syn-rift succession is made up of lacustrine sediments which are considered as the main source rock in the basin (Lee et al., 1996). One of the giant oil fields is the White Tiger field with estimated reserves of about 1.0 - 1.4 billion barrels of oil. Current daily production is 250,000 barrels, 90 percent of which is come from the fractured basement reservoirs with the remainder produced from Oligocene and Miocene classic reservoirs. However, there are not any papers reporting maturity and properties of the sediments in this basin based on analyses of alteration of clays**.** Nowadays, extensive explorations in this, present a good opportunity to investigate the relationship between the degree of illitization and thermal history of the basin as well as its effect on rock properties. Such a study also might help to appraise the prospectivity during exploration and the economic viability of potential petroleum discoveries.

In this paper, we report a study of smectite-to-illite transformation in a suite of Tertiary sediments from an exploration well in the Block 16-1, Cuu Long basin, Vietnam. The samples used for this study are cuttings collected down to about 3,500m. By choosing a suitable method to accurately estimate the percentage of illite in mixed-layer illite/smectite mineral, the first order kinetic equation of the smectite-to-illite reaction is utilized to evaluate the geothermal history of Tertiary sediments in the Cuu Long basin for the first time. The mechanism of this reaction is also discussed in relation to the presence of micro quartz cementation.

2. Methods

2.1. X-ray Diffraction (XRD)

Thirteen samples from an exploration well in the Western Block 16-1 (Fig. 1), Cuu Long basin, were collected from 2,460m down to 3,490m. All the cutting samples were analyzed by XRD for whole-rock mineralogy and clay mineralogy (< 0.2µm), using a Philip X'Pert X-ray diffractometer (Cu Kα, 40kV and 30mA).

2.1.1. Detrital mineralogy

For semi-quantitative analysis of whole-rock samples, the added internal standard reference intensity (RIR) method, modified from Moore and Reynolds (1997) and S. Hillier 2003, was utilized. Therefore, the finely gridded powders were mixed with 50% purified corundum (Al_2O_3) and then were analyzed by X-ray diffractometer. Semi-quantification is based upon calculation of the peak intensity divided by the measured peak intensity of the main corundum 113 peak and multiplied by weight percentage of added corundum divided by the RIR_{cor} (Table 1).

2.1.2. Clay mineralogy

Sample preparation: For the purpose of analysis of the clay fractions, the cutting samples were crushed into a fine powder, and organic materials removed by hydrogen peroxide, and disaggregated by ultrasonicator. The < 0.2µm fractions were obtained by sedimentation and then centrifugation, the settling time was calculated according to Stoke's law. Clay suspensions were treated by 0.1M calcium solution prior to orientation on glass slides and were analyzed after air-drying and after vapor saturation with ethylene glycol at 60°C for 4 hours. The exchanging cation is necessary because clay minerals absorb anions and cations and hold them in an exchangeable state. Additionally, the d-spacing of smectite or mixed-layer mineral illite/smectite depends on the type of cation held in the exchangeable sites. The technique for exchanging calcium is relatively uncomplicated, our laboratory experiments have demonstrated that cations

Table 1. *Reference intensity ratios (RIRs) used for semi-quantification (modified after S. Hillier, 2003)*

Mineral	Peak position	RIR_{cor}
Quartz	3.34	4.04
Calcite	3.03	2.73
Plagioclase	3.19	2.07
K-Felspar	3.24	1.00
Pyrite	2.72	1.70
Kaolinite	3.52	0.54
Chlorite	3.58	0.53
Corundum(standard)	2.08	1.00

in the interlayer of smectite are regularly exchanged with calcium if clays are twice treated with 0.1M $CaCl_2$ solution and carefully washed by distilled water. After treatments, the first peak of the XRD patterns of exchanged smectite identically shows at 15Å in d-spacing. That condition was repeatedly applied to all samples in this study.

Identification and quantitative analysis: The method to identify clay phases is modified from Moore and Reynolds (1997). In this study, both smectite and random mixed-layer illite/smectite is represented as an expendable mineral. Its quantity was determined by the integrated area of the expanded 17Å peak with ethylene glycol treatment, whereas the type of ordering (R0, R1 or R3) was determined by the location of 001/002 illite/EG-smectite peak. The normalized RIR method (Chung, 1974; Snyder, 1992) was applied for semi-quantitative analysis of clay fractions prepared as oriented mounts. The factors are 1, 4, 2 and 2 for the glycolated smectite 001, the illite 001, and the chlorite 002 and kaolinite 001, respectively. In order to apply the kinetics of the smectite illitization ratio, the percentage of illitic layers in the mixed-layer illite/smectite was determined upon estimating $\Delta 2\theta$ after careful calibration using the NEWMOD program (Moore and Reynolds, 1997).

2.2. Scanning Electron Microscopy (SEM)

The samples were embedded with epoxy resin before cutting, gridding, polishing and then coating with gold in order to obtain the cement textures on the Jeol 5,600 Scanning Electron Microscopy (SEM). To acquire a high quality backscattered scanning electron images (BSEIs), the acceleration voltage is adjusted to 30kV. However, it is adjusted down to 20kV at 20cm in walking distance prior to EDS analysis to identify the elemental composition and qualitative mineral identification.

3. Results and discussion

3.1. Detrital mineralogy

The general mineralogy of the Cuu Long basin within litho-stratigraphic frameworks is discussed in detail in Lee et al (1996) and in Nhuan T.V et al (2009 and 2010). Hence we only reexamined the detrital minerals in the research well by using XRD characterization and SEM prior to discussion of the mechanism of the smectite-to-illite reaction. The information about detrital mineralogy is desired because rock types are controls on occurrence and behavior of the smectite-to-illite transformation during diagenesis (J.M. McKinley, 2003). According to the XRD results, the major minerals of the collected sediment samples are quartz, plagioclase, K- feldspar, and minor calcite. BSEI images show the roundness of detrital grain varies from angular to subangular and also indicate partial dissolution of detrital K-feldspar grains (Fig. 4). The quantity of respective phases is calculated and shown in Table 2.

In the above table, only minerals having relatively high concentration were quantified, the other phases

Table 2. *Detrital mineralogy determined by the RIRs method*

Depth (m)	Quartz (%)	Calcite (%)	Plagioclase (%)	K-Feldspar (%)	Clays (%)	Rock type
2160	58.5	0.0	14.2	14.4	13.0	Fine sandstone
2395	50.5	0.0	26.0	9.5	14.0	
2550	57.6	0.0	27.6	14.4	0.3	
2645	47.5	0.0	19.2	21.3	12.0	
2715	45.9	2.8	11.2	7.6	32.5	Fine sandstone
2805	37.2	0.0	4.9	8.2	49.7	
2850	37.1	0.0	9.7	17.3	35.9	
2865	33.0	0.0	6.0	13.5	47.5	
2900	55.7	2.5	25.0	16.6	0.3	
2915	41.7	3.6	8.4	9.8	36.6	Mudstone
2965	38.8	15.4	6.8	13.3	25.7	
3395	44.5	3.7	15.2	11.6	25.0	
3490	44.8	0.0	7.4	12.8	35.0	

including clay minerals and organic compounds could not be included because of their relatively low concentration. Quantities of major phases (quartz, calcite, albite and K-feldspar) then were normalized after Chung (1974) before illustrating as a function of depth (Fig. 2). Generally, there is not a considerable change in the mineralogy pattern of sediments from 2,160m to 2,900m. A significant change in mineralogical components was observed from depths greater than 2,915m, which is marked by a dramatic increase in calcite content within a peak of 15.2% calcite at 2,965m depth (Table 2). In order to interpret changes in dispositional facies, the mineralogical data of the present research was plotted as a function of depth in comparison to studies of Nhuan T.V et al. (2009). The mineralogical data show similar patterns, a significant increase in the proportion of calcite with increasing depth of burial. These changes are presumed to be a result of changes in sedimentary composition or in depositional facies.

3.2. Clay mineralogy

Authigenic minerals are dominated by combinations of chlorite, kaolinite, illite, smectite, and mixed-layer illite-smectite mineral (IS) with a minor amount of quartz. The quantities of these minerals were determined and then listed in Table 3. Excepting smectite, the proportion (by weight) of other authigenic minerals do not show a clear tendency when moving down the drill hole, which might be controlled by differences in detrital mineralogy and depositional facies. Thus it is not reasonable if using the clay mineralogical pattern as a function of depth to evaluate the diagenesis degree. Meanwhile a number of previous studies have demonstrated that IS mineral is a valuable candidate for diagenesis study. Hence it is mainly discussed in this study; other clay minerals such as kaolinite and chlorite are of less concern, even they also influence rock properties.

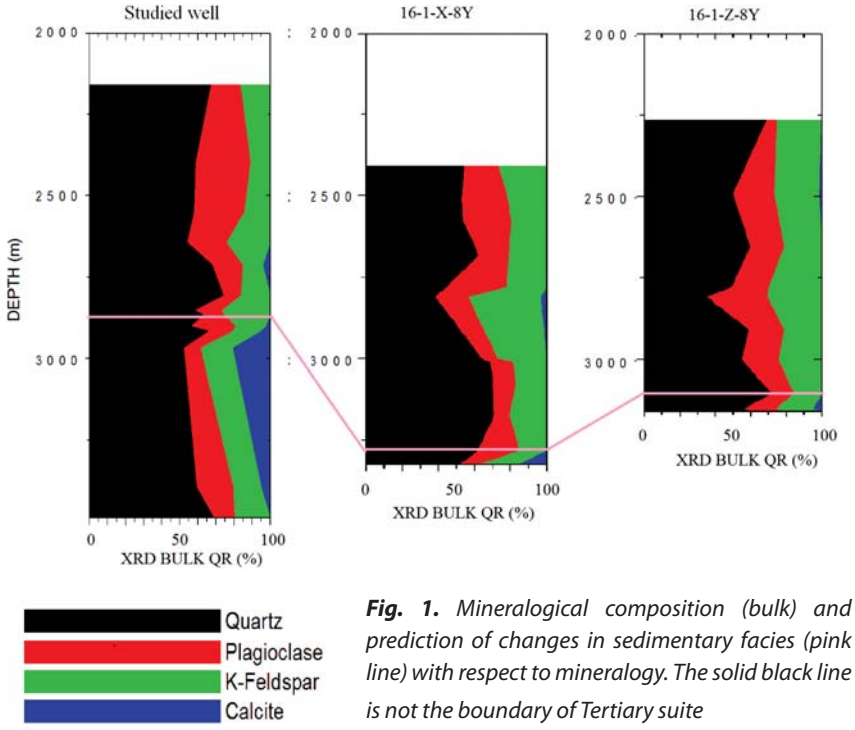

Fig. 1. *Mineralogical composition (bulk) and prediction of changes in sedimentary facies (pink line) with respect to mineralogy. The solid black line is not the boundary of Tertiary suite*

Table 3. *Clay mineralogical data determined by XRD of < 0.2μm factions*

Depth (m)	Chlorite (%)	Kaolinite (%)	Illite (%)	Illite-smectite (%)	Smectite (%)
2160	21.35	24.13	29.12	9.18	10.77
2395	15.30	19.28	35.08	10.05	16.76
2550	18.48	24.16	26.42	11.42	16.50
2645	21.89	23.16	23.90	10.49	18.06
2715	28.52	28.52	16.61	12.89	11.33
2805	28.61	29.83	22.73	8.64	8.23
2850	29.50	31.72	25.60	14.29	2.38
2865	34.12	35.17	18.38	16.61	0.98
2900	24.97	30.61	23.09	7.58	15.79
2915	32.37	35.10	13.77	14.97	1.72
2965	25.52	34.52	30.38	8.14	1.45
3395	31.85	27.74	40.42	0.00	0.00
3490	28.30	28.30	43.40	0.00	0.00

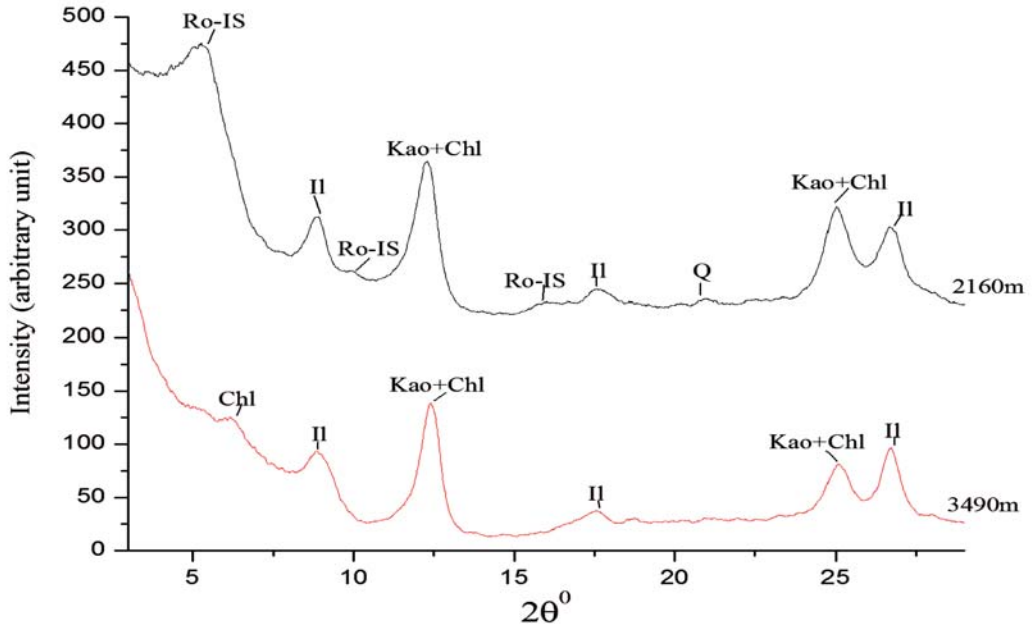

Fig. 2. *XRD patterns of EG-saturated < 0.2μm fraction cuttings from different depths. Ro-IS, random illite/smectite; Kao, kaolinite; Chl, chlorite; Il, illite; Q, quartz*

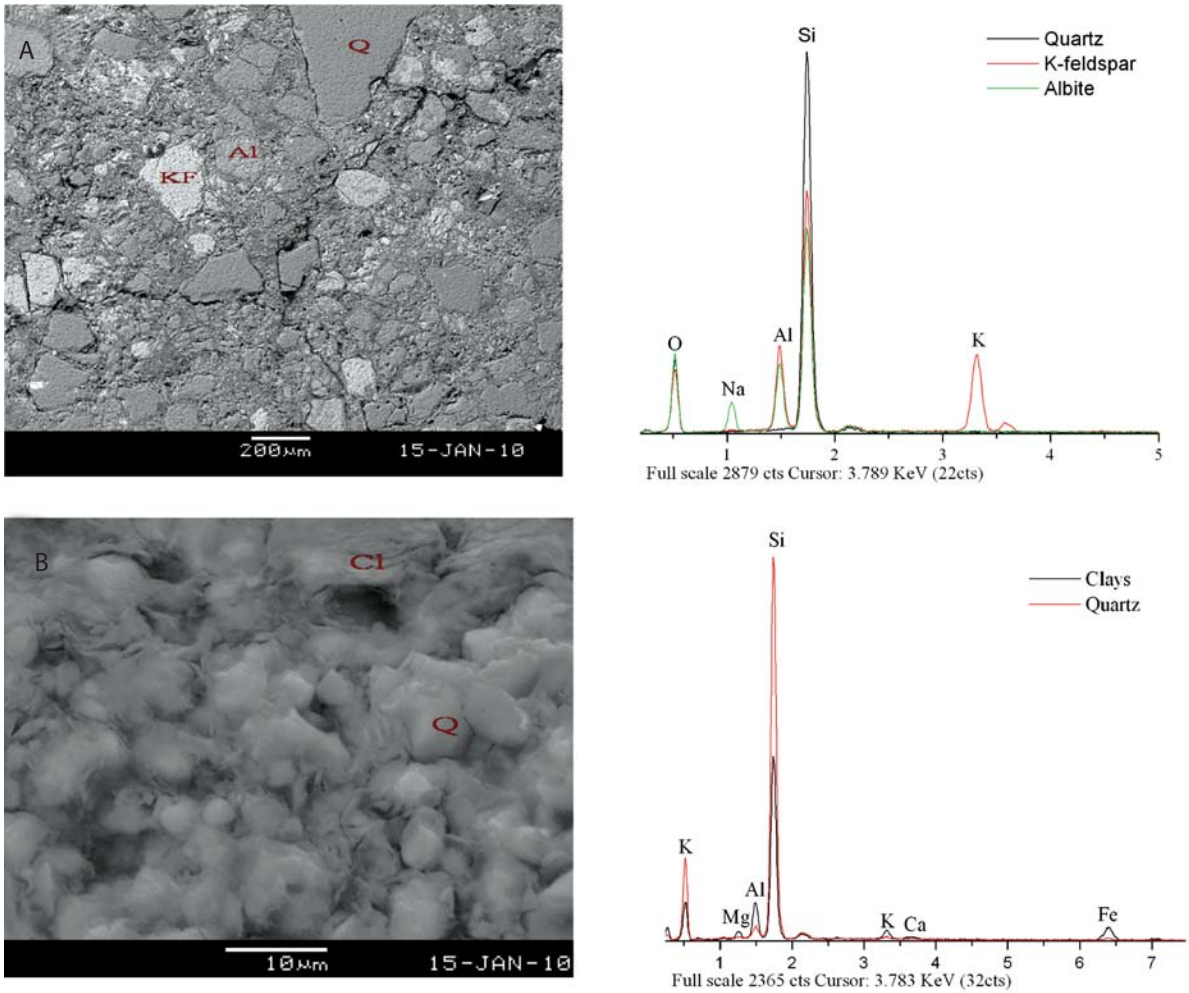

Fig. 3. *Backscatter electron image. (A) Rock texture and dissolution of primary K-feldspar. (B) Individual micro-quartz within fine clay matrix. Q, quartz; Al, albite; KF, K-feldspar; Cl, clays*

An absence of smectite and IS mineral at burial depths below 2,965m is fair evidence of the smectite-to-illite transformation with increasing burial depth. Occurrences of minor microcrystalline quartz incorporated with clays verify that a significant amount of silica is released into solution while smectite is converted to illite (Fig. 3 and Fig. 4). The release of silica during the transformation might result from substitution of Al for Si in the smectite structure (Hower et al., 1976). Therefore during diagenesis processes, the alteration of rich smectite sediments may influence their physical properties. One of the possible reasons may be the partial dissolution of detrital K-feldspars and occurrence of individual authigenic quartz crystal thus increasing pore sizes (Fig. 4). Additionally, the effect of micro-quartz cementation due to the release of Si from the smectite-to-illite alteration is not a single factor influencing the compaction of smectite rich sediments, but also increases in clay particle size and decreases in expendability resulting from S-I transformation may cause increasing rock permeability and reducing overpressure therefore increasing the rate of compaction (Peltonen et al., 2008).

3.3. Thermal history of Miocene-Oligocene sediments

The illite/smectite (IS) data reveal that the proportion of illite in interstratified illite/smectite steadily increases with increasing depths of burial (Fig. 4A). It starts at about 20% of illite at 2,160m, and the percentages of illite in IS are > 90% at depths below 2,800m. This observation demonstrates

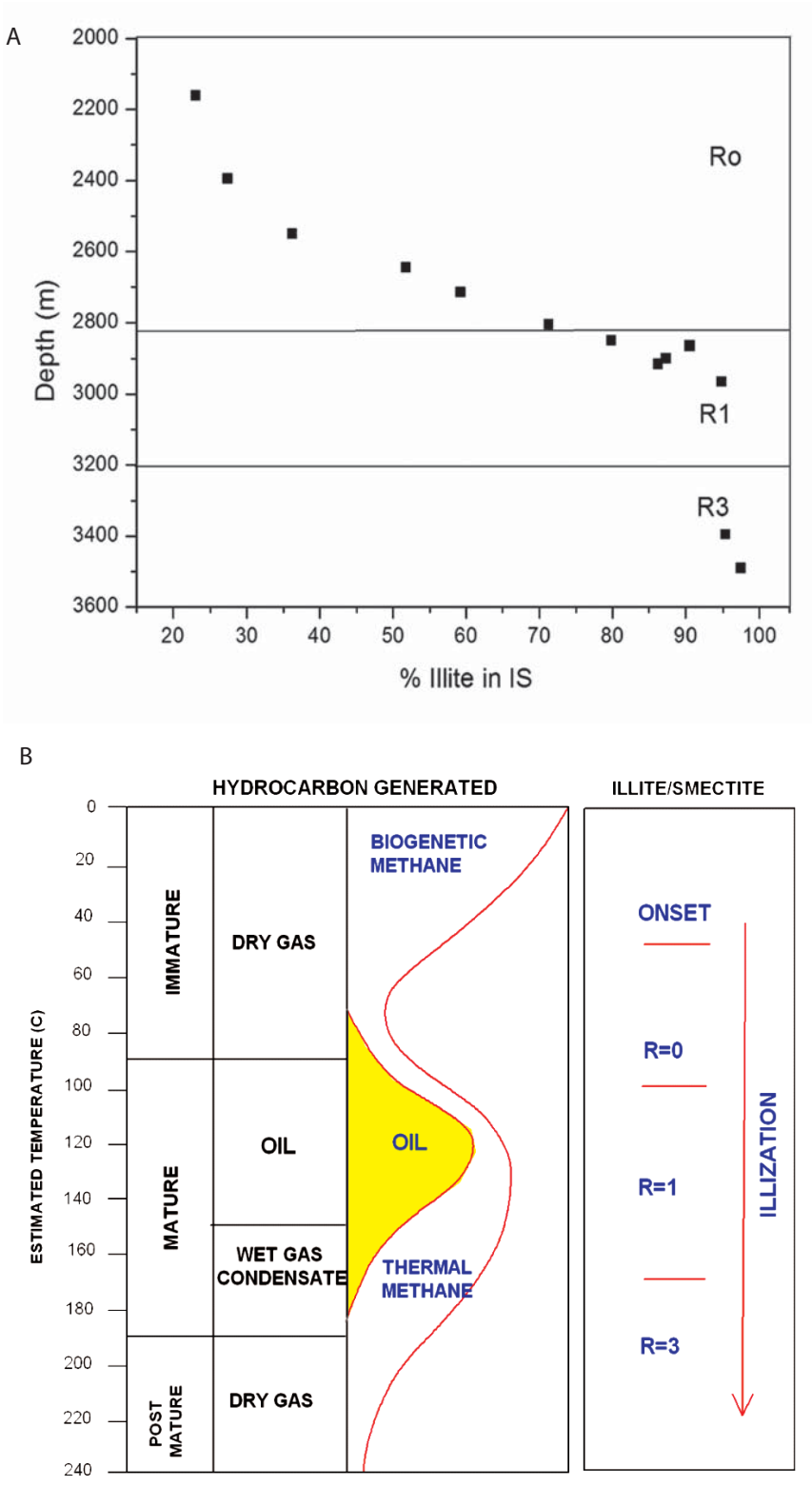

Fig. 4. *(A) The percentage of illite component in the interstratified illite–smectite (I/S) phase, plotted as a function of depths (R0, randomly interstratified I/S; R1and R3, ordered I/S). (B) The relation between smectite-to-illite conversion via mixed-layer I/S mineral and hydrocarbon generation (Richard M.R et al., 1993)*

that mixed-layer IS mineral is a precursor of authigenic illite. As discussed earlier, a major factor that controls the smectite-to-illite reaction is temperature, as confirmed by many observations both from nature and laboratory experiments (Huang et al., 1993; S. Hillier 1995; Reynolds et al., 1984, Hower et al., 1976). Therefore, IS mineral has been used as an indicator to predict the maturity of hydrocarbon source rocks. Based on Reichweite indices of IS mineral, determined by analyses of XRD profiles, the sedimentary succession in the researched well was classified into three different zones: R0, R1, and R3 corresponding to random illite/smectite, R1 ordered illite/smectite, and R3 ordered illite/smectite, respectively. Fig. 5 shows a comparison of the present observation in the Cuu Long basin to the theory of Richard et al., (1993). The sedimentary succession from 2,850 to 3,200m corresponds to the main oil-production phase, however sediments located at the depths greater than 3,200m are over matured thus only wet or dry gas is probably generated (Fig. 5).

Nevertheless, the transformation of smectite to illite is not only controlled by temperature but also by several other factors including burial rate, time, Na/K ratio, activation energy and the initial illite fraction in the IS mineral (Huang et al., 1993; S. Hillier, 1995). These factors reflect geological environments. Herein the kinetic equation of the smectite-to-illite reaction is utilized to predict the thermal history as well as other geological parameters of the Cuu Long basin for the first time. The aluminum (Al) required for the reaction is supplied by the destruction of additional smectite layers, and potassium (K) is produced by partial dissolutions of detrital F-feldspar grains (Eberl and Hower, 1976). It is reasonable because XRD results for bulk samples indicate that all collected samples contain a significant amount of K-feldspar, and SEM observation also shows dissolution and albitization of K-Feldspar. The reaction is simplified in Eq. (1).

$$\text{Smectite} + Al^{3+} + K^{+} \rightarrow \text{Illite} + SiO_2 \qquad (1)$$

The kinetic equation used herein is modified from Huang et al., (1993):

$$-dS/dt = k[K^{+}]S^2$$

Where: S is molar fraction (smectite %) of smectite in the illite-smectite mixed layer;

$[K^{+}]$ is concentration of the dissolved potassium; k is rate constant.

In order to approach the kinetic modeling of the smectite-to-illite reaction for the present researched area, potassium concentration, geothermal gradient and burial rate were adjusted to get the optimum model. Fig. 6 shows the model of smectite to illite conversion in comparison to clay mineral data from Oligocene - Miocene sediments in the Cuu Long basin. The best fit model was constructed by using an initial smectite-illite ratio of 85%, geothermal gradient of 33°C/km, 250m/ma of burial rate, and 250ppm. Based on the kinetic modeling, the maximum temperature of sediments in the studied well is about 110°C, lower than the value estimated by comparing Reichweite indices to Richard M.R's model (1993). However in this research, the burial rate was adjusted arbitrarily to find out the best fit model therefore additional work, possibly K/Ar dating, may help to better estimate the thermal history. In addition, because this research is base on the limited data set, so

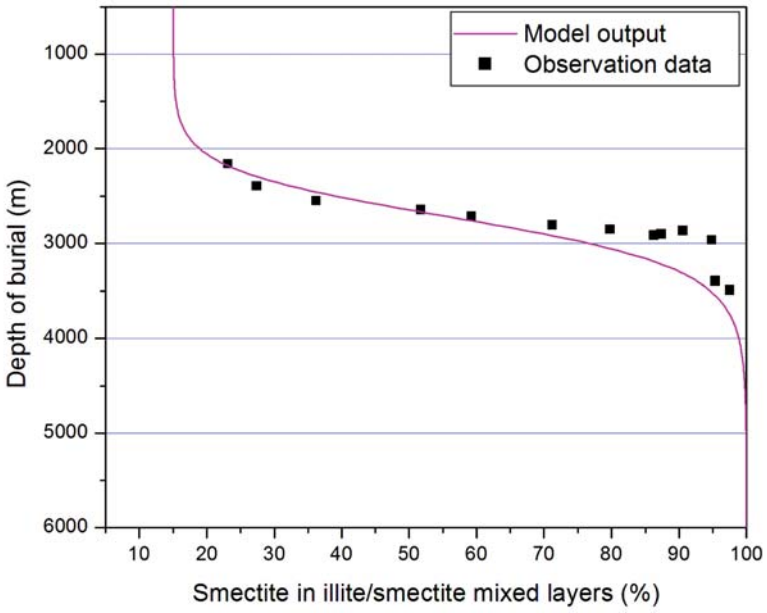

Fig. 5. *Kinetic modeling of smectite-to-illite transformation in comparison to clay mineral data from Oligocene-Miocene sediments in the Cuu Long basin*

larger data sets with better references about geological setting need to be carried out.

4. Conclusion

XRD results for clay fraction (< 0.2μm) in combination with SEM observation show a progressive illitization of smectite with increasing depth, which resulted in the release of significant amounts of silica into solution. Silica locally participated to form authigenic quartz within the clay matrix, thus it might cause changes in rock properties.

The smectite-to-illite conversion not only effects on quartz cementation but also may reflect on thermal history as well as geological environment of the basin. The IS data and the kinetic modeling demonstrate that the sediments at the depths of 2,160 to 3,200m are well matured, however these rocks at depths below 3,200m are probably over matured.

A dramatic increase in proportions of illite in the mixed-layers illite/smectite indicates a rapid dispositional environment. Most smectite in sediments at depths below 2,915m was converted to illite, a significant difference from that in its overlying sediments, which may reflect changes in temperature gradient over time.

Acknowledgements

The authors express thanks to Vietnam Petroleum Institute for providing data and giving permission for publishing the results. Prof. Song Y and Prof. Kim Jinwook are also thanked for helpful advice and suggestions.

References

1. Peltonen C. et al. *Clay mineral diagenesis and quartz cementation in mudstones: The effects of smectite to illite reaction on rock properties*. Marine and Petroleum Geology. 2008: p. 1 - 12.

2. Burst Jr. et al. *Post diagenesis clay mineral-environmental relationships in the Gulf Coast Eocene*. Clay & Clay minerals. 1959; 6: p. 327 - 341.

3. Douglas N.M et al.. Clay & Clay minerals 6,327-341. *Early clay diagenesis in Gulf Coast sediments: New insights from XRD profile modeling*. Clays & Clayminerals. 2008; 56 (3): p. 359 - 379.

4. Fyhn M.B.W. et al. *Geological development of the Central and South Vietnamese margin: Implications for the establishment of the Earst Sea*. Indochinese escape tectonics and Cenozoic volcanism. Tectonophysics. Tecto-12686. 2009.

5. Gwang Lee et al. *Geologic evolution of the Cuu Long and Nam Con Son Basins offshore Southern Vietnam*. AAPG Bulletin1996; 85 (6): p. 1055 - 1082.

6. Hillier S. et al. *Illite/smectite diagenesis and its variable correlation with vitrinite reflection in the Pannonian Basin*. Clays & Clayminerals. 1995; 43 (2): p. 174 - 183.

7. Hillier S. et al. *Accurate quantitative of clay and other minerals in sandstones by XRD: Comparison of a Rietveld and reference intensity ratio (RIR) method, and the importance of sample preparation*. 2000.

8. Hower J. et al. *Mechanism of burial metamorphism of argillaceous sediment: 1. Mineralogical and chemical evidence*. Geological Society of America Bulletin. 1976; 87: p. 725 - 737.

9. Huang et al. *An experimentally derived kinetic model for smectite-to-illite conversation and its use as a geothermometer*. Clays & Clayminerals. 1993; 41 (2): p. 162 - 177.

10. McKinley J.M. Clay mineral cements in sandstones. *Special publication number 34 of the International Association Sedimentologists*. 2003: p. 109 - 128.

11. Moore and Reynolds. *X-ray diffraction and the identification and analysis of clayminerals*. Oxford University Press, New York. 1997.

12. Richard M.P. et al.. *Considerations and applications of the illite/smectite geothermometer in hydrocarbon-bearing rocks of Miocene to Mississippian age*. Clays & Clayminerals. 1993 ; 41(2), p. 119 - 133.

13. Sorodon et al. *Quantitative mineralogy of sedimentary rocks with emphasis on clay and with applications to K-Ar dating*. Mineralogical Magazine2002; 66 (5): p. 677 - 687.

14. Sorodon et al. *Interpretation of K-Ar dates of illitic clays from sedimentary rocks*. 2002.

15. Susanne Gier et al. *Diagenesis and reservoir quality of Miocene sandstone in the Vienna basin*. Austria. Marine and Petroleum Geology. 2008: p. 1 - 15.

Late Pleistocene - Holocene seismic stratigraphy of Nha Trang Shelf, Central Vietnam

Bui Viet Dung
Vietnam Petroleum Institue
Karl Stattegger
Institute of Geosciences, Kiel University
Phung Van Phach, Tran Tuan Dung
Institute for Marine Geology and Geophysics

Abstract

The late Pleistocene - Holocene stratigraphic architecture on the steep and narrow shelf off Nha Trang, Central Vietnam has been explored by high resolution seismic profiles integrated with sediment core data. Sequence stratigraphic results reveal five major seismic units and three bounding surfaces which are composed of two distinctive sequences. Those sequences are bounded by two regional unconformities (SB1, SB2) which have been formed in respond to different sea-level regimes during Marine Isotope Stage (MIS) 5e to the Last Glacial Maximum (LGM) period. The revealed relict beach-ridge deposits at a water depth of about ~ 130m below the present water depth indicate that the LGM sea-level in this area was lower than in neighboring areas and probably resulted from subsidence due to a high sedimentation rate and/or neotectonic movements of the East Vietnam Fault System. The late Pleistocene - Holocene high amplitude of sea-level change during a long fourth-order and superimposed by shorter fifth-order cycle is the principal factor in reorganizing the formation of the Nha Trang continental Shelf sequence. Other local controlling factors such as fluctuations in sediment supply, morphological variations of the LGM surface, subsidence rate and hydrodynamic conditions provided the distinctive features of the Nha Trang Shelf sequence stratigraphic model in comparison to neighboring areas.

1. Introduction

The Nha Trang Shelf is located on a passive continental margin (Fig. 1). Following the Last Glacial Maximum (LGM) about 20ky BP (Before Present), the shelf was submerged rapidly due to its narrow and steep gradient during the post-glacial sea-level rise and therefore many older deposits were protected from erosion during the deglacial transgression. Well preserved relict deposits provide an excellent example for testing sequence stratigraphic concepts which are applied worldwide on continental shelves.

Previous studies on Holocene sedimentation on the Vietnamese Shelf has revealed high sediment accumulation rates off Central Vietnam reaching up to 50 - 100cm/ky [30]. It is also indicated that the surface sediments of the inner shelf in this area were dominated by relict sand [1, 13, 34, 35]. Different sand-barrier generations at Hon Gom Peninsula were dated between BP [12]. Detailed studies on the late Quaternary sequence stratigraphy on the nearby shelf were concentrated on the central Sunda Shelf [18, 19, 20].

Results of sequence stratigraphy on the Central Vietnam Shelf were mainly focused on the offshore Cenozoic basin evolution and hydrocarbon potential [16, 23], but the late Quaternary sequence stratigraphy on the Central Vietnam Shelf was not investigated in detail. In this research, we will apply the concept of sequence stratigraphy to the interpretation of shallow seismic high-resolution profiles on the Nha Trang Shelf (Fig. 1). The general aims of this study are therefore to:

+ Analyze the late Pleistocene - Holocene seismic stratigraphic architecture.

+ Reconstruct the late Pleistocene - Holocene evolution of the shelf and propose a general sequence stratigraphic model.

+ Compare the Nha Trang Shelf to other sequence stratigraphic models to distinguish local controlling factors.

2. Regional setting

The Nha Trang Shelf is bordered by the Vietnamese coastline to the West and the East Sea (SCS) to the East (Fig. 1). The continental shelf is narrow and separated from the deep East Sea by the N-S directed East Vietnam Fault System on the continental slope and rise (Fig. 1). This fault system is generally considered to be the Southward extension of the Red River strike-slip fault zone and runs almost parallel to the shoreline along the 110° - longtitude [11, 16, 23]. The continental shelf of the study area is 40km wide on average, steep in the middle and gentle in the inner-outer shelf (Fig. 1). There are two bays in the study area: Van Phong in the Northern and Nha Trang in the Central part. The climate and hydrodynamic conditions of the study area are driven by the East Asian monsoon system with winds mostly from the NE during winter (October to March) and the SW during summer (April to September) [27]. Most of the sediments are supplied to the shelf by numerous small and short rivers which drain the high relief with maximum elevation of 2,000m (Fig. 1). Estimated total suspended sediment load of all small rivers in the study area ranges from 1.7 - 4 $\times 10^6$ ton/year, of which the Cai and Dinh Rivers account for about 90% [5]. About 70% of supplied sediments are transported to the shelf during short periods of the rainy season (September to December) and 30% in the dry season (January to August). Long-term monitoring data (1985 - 1995) collected in Nha Trang station indicate an average temperature of 27°C and average rainfall of 96.7mm/month. The study area is dominated by a semi-diurnal to diurnal tide regime with amplitude of 0.4m in neap and 2.5m in spring tides [27, 34]. Average wave height in this area ranges from 0.5m and 2.0m during fair-weather and can reach up to 7.5m during storm conditions [38].

3. Methods and available data

About 620km of 2D high resolution seismic profiles have been analyzed on the Nha Trang Shelf (Fig. 1). Those data have been collected at the beginning of the SW monsoon season (April and May) during different cruises in the framework of the Vietnamese - German cooperation project: SO 140 [41], VG5 (2004), VG9 (2005), SO187 [42]. Seismic data were acquired with two different sound-sources: boomer and parasound. Since the objective of the research concentrates on the continental shelf, most of the profiles are located at water depths between 20 and 200m (Fig. 1). The boomer system (EG & G Uniboom) is a single channel system which includes an electrical energy supplier and an electromagnetic transducer that transforms the discharged energy to electro-dynamic acoustic pulses. During the surveys, the transducer of the boomer source was employed in a catamaran that was towed along with a hydrophone-streamer receiver (with 8 hydrophones) astern of the vessel. The average speed of the vessel was 4 knots. The boomer source regularly produced from 2 - 2.67 shots per second at 150 Joules. The main working frequencies of the system range between 0.3 - 11kHz resulting in a typical penetration of 20 - 100m below the seabed

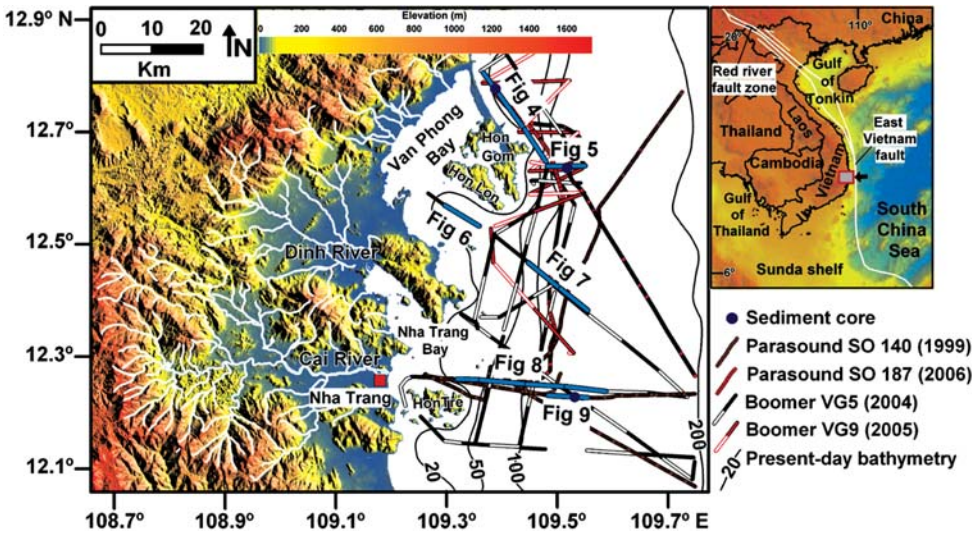

Fig. 1. *Map of Nha Trang Shelf with modern bathymetry and available data (seismic profiles and sediment cores). Locations of geological faults adapted from Fyhn et al (2009) and Clift et al (2008). Elevation data of the land part is extracted from Shuttle Radar Topography Mission (SRTM) digital elevation models (http://srtm.usgs.gov).*

depending on the acoustic impedance (product of velocity and density) of the sediments. The sound waves were reflected when reaching the reflection surfaces which are regarded as acoustic-impedance contrast boundaries. The hydrophone-streamer received the pressure reflection signals and converted them into voltage responses before transmitting them to the computer. Seismic traces were digitally recorded and displayed using NWC software. A GPS (Global positioning system) was used to guarantee the accurate positions of the recorded seismic traces. Parasound is a hull-mounted system which combines a narrow beam echosounder with a sub-bottom profiler. The system is operated with a fix primary frequency of 18kHz and a secondary primary frequency variable from 20.5 - 23.5kHz. Both primary frequencies are transmitted simultaneously in a narrow beam (~5°) and the constructive interference of these frequencies (parametric effect) allows to generate a working frequency (secondary frequency) within the beam of 2.5 - 5.5kHz [17]. In our research, the parasound data was collected with secondary primary frequency of 22kHz resulting in secondary working frequency of 4kHz. The data was digitally recorded and sampled at a frequency of 40kHz. Navigation data were supplied by the ship's GPS.

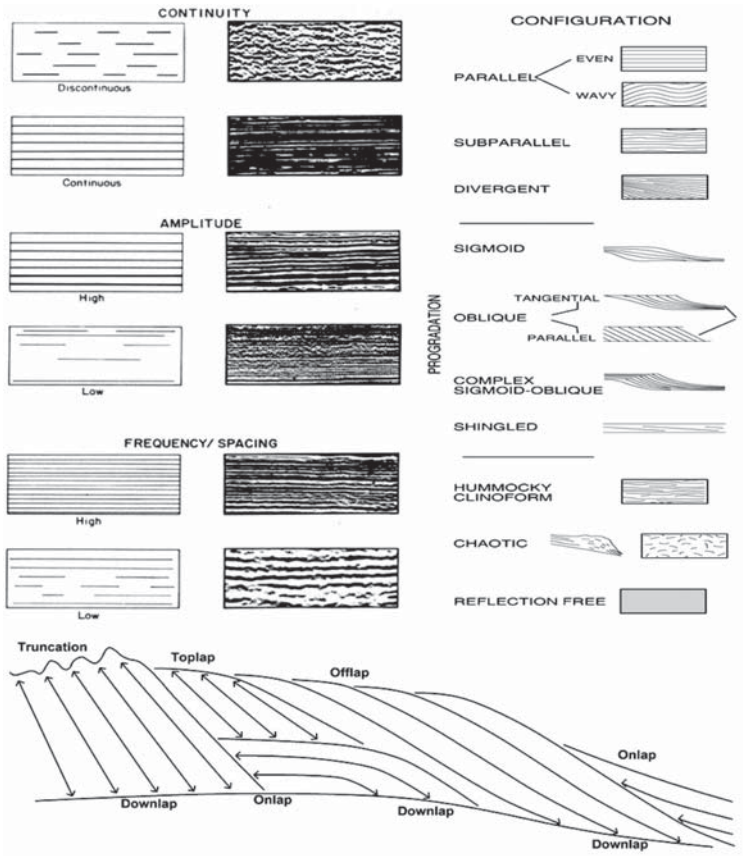

Fig. 2. *Classification of seismic facies and related depositional environments adapted from Badley (1985), Vail (1987), Catuneanu (2002) and Veenken (2007)*

For data processing, the frequency high/low pass filtering has been applied for the recorded data. The frequency band - pass filtering of 2.5 - 6kHz for parasound and 0.5 - 7kHz for boomer data are applied for all seismic profiles on the Nha Trang Shelf. The interpreted seismic surfaces are then picked with the software Kingdom Suite SMT 8.4. Average sound velocity of 1,500m/s in sea water and 1,550m/s in subsurface sediments has been assumed for Two-way travel time (TWT) - depth conversion.The seismic data are interpreted on the basis of the sequence stratigraphic concept which was initiated by Mitchum and Vail [26], Vail [49], and then further refined by numerous authors. The seismic units are distinguished from each other by their reflection continuity, amplitude, frequency and configuration (Fig. 2).

Besides, the termination patterns of the seismic reflectors at the bounding surface as toplap, onlap, offlap, downlap and truncation (Fig. 2) are also important criteria for identifying depositional trend [8]. The interplay between base level changes (combined effect of eustasy, tectonics, sediment compaction, and environmental energy) and sedimentation rate controls the formation of sequence systems tract (Fig. 3). For simplicity (by neglecting the energy of waves and currents), the base level is equated with the sea level [8]. Hence, the concept of base level change is identical with the relative sea-level change. Accommodation is defined as the space available for sediments to accumulate and its variations depend on base level changes. In this research, we apply the four-fold division of systems tract to divide the sedimentary architecture into different stages in relation to sea-level fluctuations [8, 9]:

+ Falling stage systems tract (FSST) is formed entirely during the stage of relative sea-level fall (forced regression) and it occurs independently with ratio between sedimentation rate/accommodation spaces.

+ Lowstand systems tract (LST) is formed during sea-level lowstand and slow sea-level rise when the rate of rise is lower than the sedimentation rate (normal regression).

+ Transgressive systems tract (TST) is formed during the stage of relative sea-level rise when the rate of rise is higher than the sedimentation rate.

+ Highstand systems tract (HST) is formed during the late stage of relative sea-level rise and when the rate of rise is lower than the sedimentation rate.

4. Results

4.1. Sequence stratigraphic analysis

In general, five seismic units and three major bounding surfaces are identified on the seismic profiles. The seismic units and their reflection configurations are summarized in Table 1.

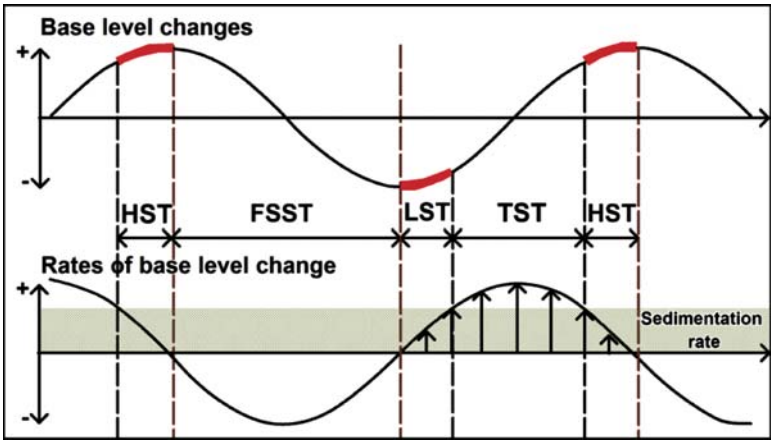

Fig. 3. *Sequence stratigraphic systems tracts as defined by the interplay between base level changes and sedimentation rate (modified from Catuneanu 2002). For simplicity, the sedimentation rate is kept constant during the base level fluctuations*

Table 1. *Summarize of seismic unit, reflection patterns and interpretation systems tracts on the Nha Trang Shelf. Abbreviation: FSST = Falling state systems tract, LST = Lowstand systems tract, TST = Transgressive systems tract, HST = Highstand systems tract*

	Systems tract	Seismic units	Acoustic facies and configuration	Occurence	Thickness (m)	Seismic image
Sequence 1	HST	U4	Low to moderate amplitude, variable frequency, medium continuity, locally transparent, paralell to sigmoid downlap	The entire shelf	0-25	
		RS1				
	TST	U3	Moderate to high amplitude, high frequency, high continuity, backstepping onlap, aggradation	The entire shelf	0-50	
	LST	U2	Moderate to high amplitude, variable frequency, high continuity, oblique tagential downlap, toplap	Outer shelf	20	
		SB1				
Sequence 2	FSST	U1	Moderate to high amplitude, high frequency, high continuity, oblique parallel downlap, toplap truncated	Outer shelf	20	
	HST+TST	U0	Low to moderate amplitude, transparent, paralell	The entire shelf	0-15	
		SB2				

- Major bounding surfaces:

+ SB1 is marked by high continuous and strong amplitude reflectors on seismic profiles (Figs. 4 - 9). This surface can be traced across shelf (20 - 140m deep).

+ The SB2 surface is the lowest reflection surface recorded on seismic profiles. It is presented as high continuous and strong amplitude reflectors (Figs. 4 - 9). Landward, it is mostly merged with the upper SB1 surface. However, this surface can be traced occasionally on the inner shelf where it is crossed by the SB1 surface as channel incision (Fig. 6).

+ RS1 is first surface which appears below the modern seabed (Figs. 4, 5, 7 and 8). It is characterized by medium but continuous reflectors on the mid and outer shelf. On the mid-shelf, the RS1 surface is clearly defined on seismic profiles as the boundary of the lower backstepping onlap and upper seaward downlapping reflectors (Figs. 8). Toward the outer shelf, the RS1 surface is locally identified as a strong amplitude reflection surface resting on the lower concave-up reflection layer (Fig. 5).

- Seismic units:

+ U0 is the lowest unit identified on seismic profiles. It is recorded across the shelf and bounded by the SB1 (upper) and SB2 (lower) surfaces (Figs. 4 - 8). This unit is characterized by horizontal and transparent reflectors on seismic profiles. The thickness of this unit is strongly variable and ranges from 0 - 15m.

+ U1 is characterized by oblique parallel configuration with seaward dipping reflectors. It is truncated toplap by the overlying erosional surface SB1 and contacts tangential downlap with the lower U0 unit (Fig. 5). On some seismic profiles (Figs. 8 and 9), U1 unit forms tangential downlap directly to the SB2 surface where the U0 unit is absent. In the seaward direction, it is overlain by a concave reflection unit (Fig. 5). U1 unit is only recorded on the outer shelf and pinches out landward at water depths of 100 - 120m. The estimated thickness of this unit on seismic profiles is approximately 20m.

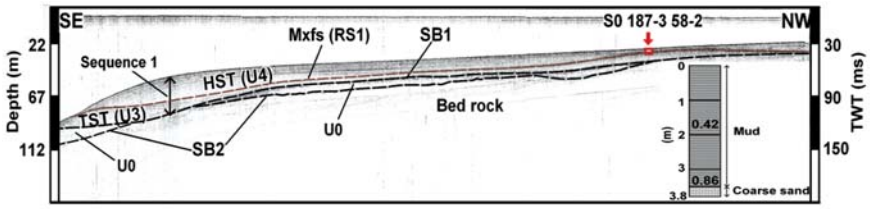

Fig. 4. *Seismic profile of the transition from inner to outer shelf on the Northern part off Hon Gom Peninsula. AMS dating indicates very young highstand deposits (0.42 and 0.86ky BP). Core data adapted from Wiesner et al (2006)*

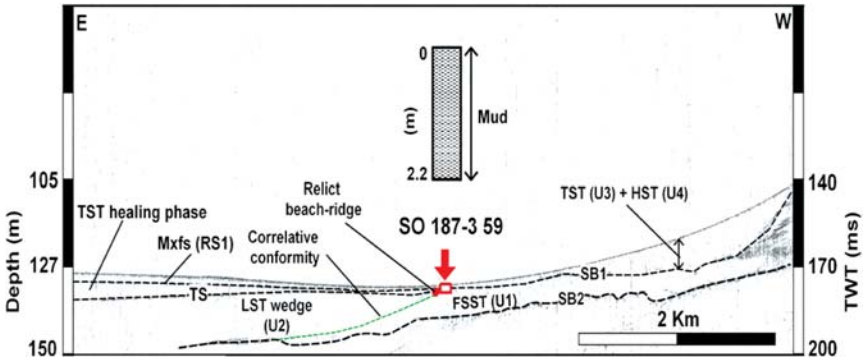

Fig. 5. *Seismic profile on the outer shelf off Hon Gom Peninsula with the complete recorded of systems tracts. Core data adapted from Wiesner et al (2006)*

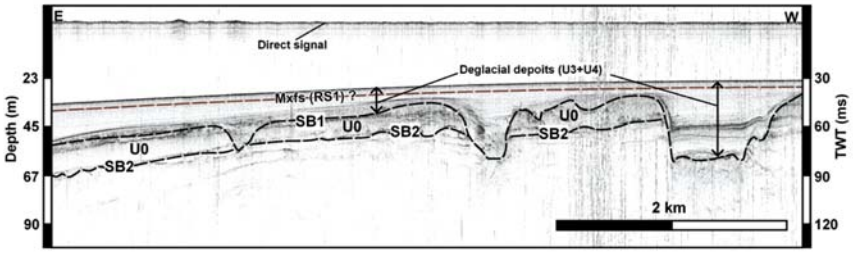

Fig. 6. *Seismic profile on the inner shelf of Van Phong Bay with aggradational stacking patterns of deglacial deposits. Discrimination between HST and TST is hardly resolved*

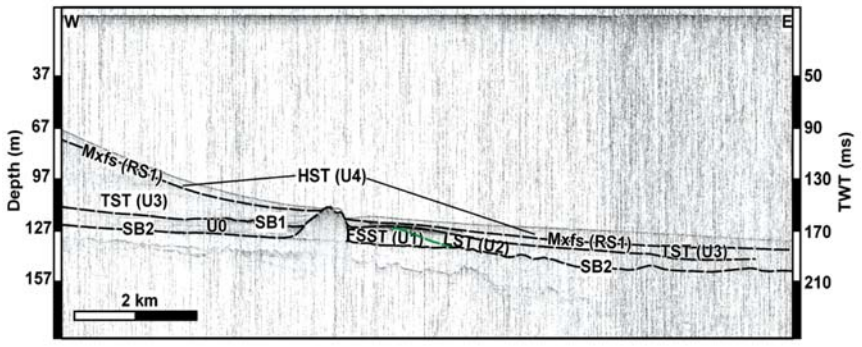

Fig. 7. *Seismic profile on the middle-outer shelf of Van Phong Bay*

+ U2 unit is developed as a seaward continuation of U1 unit and is separated landward from the U1 unit by a concave surface (Fig. 5). This unit is represented by oblique wedge shape with seaward dipping reflectors. On top of this unit, it forms toplap with the overlain smooth surface (Figs. 8 and 9). The angle of dip of seismic reflectors of U2 unit is slightly smaller than those of the U1 unit. The average thickness of this unit is about 20m. The U2 unit is only detected on the Northern shelf off the Hon Gom Peninsula (Fig. 5).

+ U3 unit is recorded across the shelf (Figs. 4 - 9). This unit is bounded by the RS1 surface on top and SB1 surface at the base. It appears as moderate amplitude reflectors with wedge-shaped configuration on the outer shelf (Fig. 5). On the mid shelf, U3 unit is expressed as high amplitude reflectors with backstepping onlap configuration (Figs. 4 - 8). Toward the inner shelf, its seismic configuration becomes aggradational stacking patterns (Fig. 6). The thickness of this unit shows low variability over the shelf with no significant depocenter. Its thickness is occasionally reduced or it is absent on seismic profiles when the basement structures come close to the surface (Fig. 8).

+ U4 is the uppermost unit on seismic profiles (Figs. 4 - 9). It is thin (average of 0 - 5m) on the inner and outer shelf with paralell and transparent seismic reflectors. Thick deposits of this unit are mostly concentrated on the mid shelf where it appears on seismic profiles as thick seaward dipping reflectors (Figs. 4 and 8). The maximum thickness of this unit reaches 20 - 25m on the mid shelf of Van Phong and Nha Trang Bay and it reduces toward the inner and outer shelf (Fig. 8).

4.2. Sedimentary characteristics and age of deposits in other studies

Coring station at a water depth of 29m (core SO187-3 58-2) on the Northern part off Hon Gom Peninsula shows a transition from coarse sand in the lowermost part to homogenous mud in the upper part of the sediment core

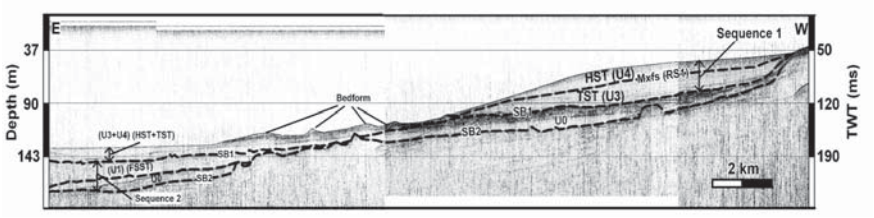

Fig. 8. *Seismic profile of transition from the inner to outer shelf of Nha Trang Bay*

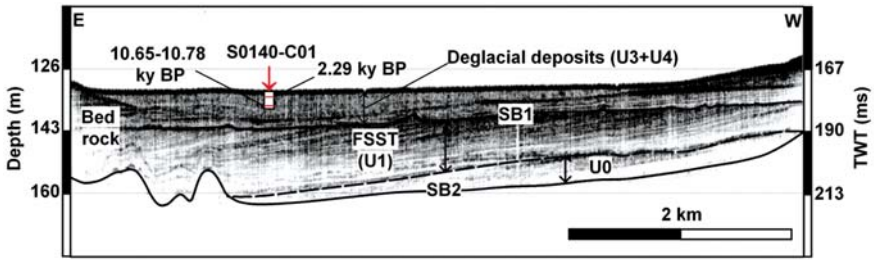

Fig. 9. *Seismic profile offshore Nha Trang Bay. Regressive unit (U1) is toplap truncated by the lowstand surface (SB1) and overlain by deglacial/Holocene deposits (U3 and U4). Core data adapted from Schimanski and Stattegger (2005)*

(Fig. 4). Two radiocarbon datings of this core provide ages of 0.42 and 0.84ky BP (Fig. 4). The 2.2m long sediment core at water depth of 133m off Hon Gom Peninsula shows a homogenous muddy layer (Fig. 5). Radiocarbon dating of sediment core at water depth of 134m on the Nha Trang Shelf (core SO 140-C01, Fig. 9) covers the age interval of 2.29 - 10.78ky BP. The sediments have a muddy composition, low sand content and abundant shell fragments along the core [30]. Earlier study on the outer Sunda Shelf indicated an age of 25 - 30ky BP of the late Pleistocene soil surface [20]. The ages of the seaward dipping clinoforms (regressive unit), at a water depth of 80 - 126m, below the LGM soils surface on the Sunda Shelf were dated as 50 - 30ky BP [19, 20]. Also, a 6.2m long core taken on the top of seaward dipping clinoforms (at water depth of 152m) on the outer Sunda Shelf indicated an age of 39 - 36ky BP for the clinoform deposits and 4.0ky BP for the overlying thin mud layer [31]. On the Southeast Vietnam Shelf, radiocarbon dating of sediment core at a water depth of 156m reaching the upper part of the lowstand wedge shows an age of 24.33ky BP [30].

4.3. Proposed sequence stratigraphic model for the Nha Trang Shelf over the last 120ky

4.3.1. Falling stage (FSST) and Lowstand system tracts (LST)

The FSST and LST are well recorded on the modern outer shelf (Fig. 10). The age of these units are derived by correlation with the regressive deposits on the neighboring shelf areas. Ages of one sediment core taken on the top of the Sunda Shelf regressive wedge at water depth of 152m were identified as 34 - 31ky BP (39 - 36 calibrated) [31]. This can probably provide the upper age limit for the FSST deposits on the Nha Trang Shelf area. On the Sunda Shelf, the outer shelf lens-shaped regressive deposits (at ~110m water depth) were formed around 45ky BP. Therefore, the forced regressive deposits (FSST) in our research recorded at 120m water depth must be formed slightly after 45ky BP. Hence, the FSST on the Nha Trang Shelf was probably formed during final stage of regression around 45 - 30ky BP (Fig. 14b). On the Vietnam Shelf, the upper part of the lowstand wedge at water depth of 156m yielded an age of 24.33ky BP [30]. This result fits well with data on the Sunda Shelf with age of 25 - 30ky BP for the late Pleistocene soil surface [20] that can be correlated with the SB1 surface on the Nha Trang Shelf. Hence, we deduce that LST deposits in our research were probably formed from 30ky BP to the LGM lowstand termination at 19.6ky BP [21]. Regressive deposits on the Nha Trang Shelf were well preserved on the modern outer shelf (at more than 100m water depth) and show seaward thickening with an average thickness of about 20 - 30m (Fig. 10). This is probably due to the fact that the outer part of the shelf was partly or entirely submerged during sea-level lowstand and therefore was protected from the effects of subaerial erosional processes. Further landward, the FSST deposits are absent in all recorded seismic profiles since the inner and mid shelf regressive deposits were subjected to long term erosional processes during the sea-level fall after MIS 5e highstand and were reworked again during the following transgression. The outer shelf lens-shaped regressive deposits documented on the Sunda Shelf [19] and the SE Vietnam Shelf [42] cannot be detected on the high-gradient shelf of Nha Trang area. We therefore consider the absence of the seaward dipping regressive deposits on the inner and mid shelf as a result of a long-term erosional hiatus (Fig. 14). The FSST unit is bounded on the top by the unconformity SB1. The SB1 surface (Fig. 11) in our work is an amalgamated surface which

was probably initiated after the MIS 5e, expanded untill the LGM sea-level lowstand and was further reworked during the subsequent deglacial transgression (Fig. 14). The SB1 surface merges seaward with the TS ravinement surface which overlies the LST wedge (U2) and FSST (U1) (Figs. 5, 8 and 9).

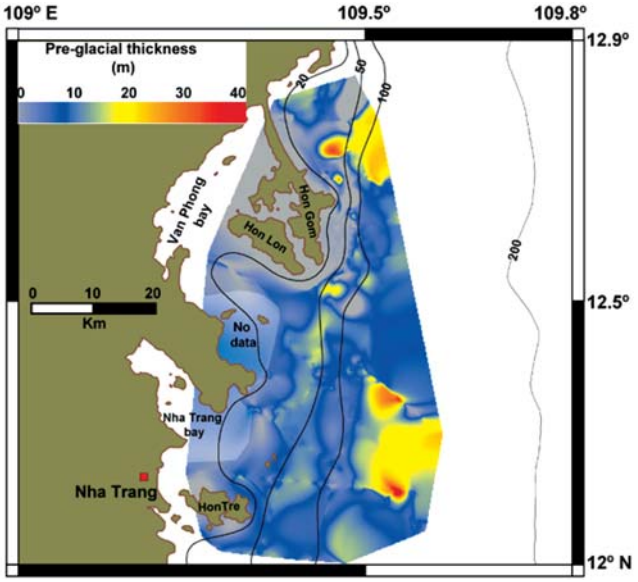

Fig. 10. *Total sediment thickness map of sequence 2 (U0, U1 units) and U2 unit. Thick deposits on the outer shelf resulted from well developed regressive units (U1 and U2) which are pinching out landward at water depth of 100 - 120m*

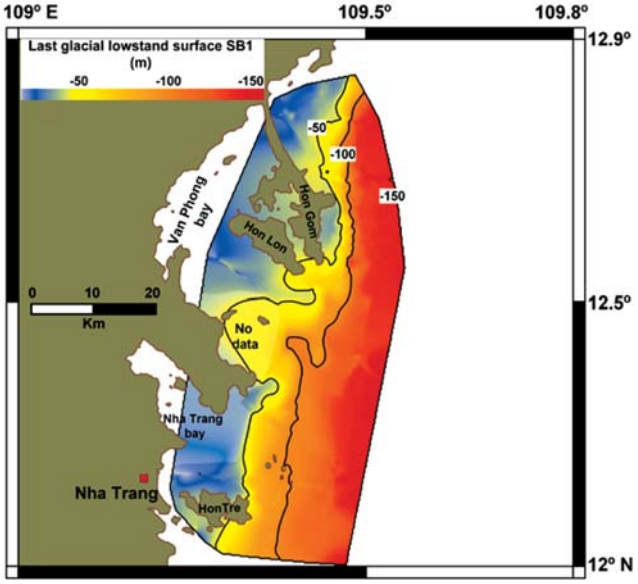

Fig. 11. *Contour map of the LGM surface SB1 with reference to the modern sea-level constructed from seismic profiles. Basically the lowstand surface was blocked at the LGM sea-level around -125 to -130m and its seaward extension was merged with the transgressive surface (TS)*

4.3.2. Transgressive (TST)

The time of maximum flooding on the Nha Trang Shelf remains unclear since the RS1 surface was not dated. However, its formation can be correlated to the initiation of the two nearby Red and Mekong River deltas which around 8.0ky BP [22, 36, 37]. We deduce that the ages of TST on the Nha Trang Shelf can range from 19.6 - 8.0ky BP. Configurations of the TST deposits show a wedge-shape on the outer shelf which represents early TST healing phase deposits. On the mid-inner shelf, its configuration changes from backstepping to aggradation stacking patterns that reflect the interaction between the rate of sea-level rise, sediment flux and the pre-existing LGM lowstand surface gradient.

4.3.3. Highstand (HST)

The HST period on the Nha Trang Shelf began about 8.0ky BP. At the same time, the Mekong and Red river deltas were initiated. The modern highstand mud deposits observed on the Nha Trang Shelf have been formed following the maximum sea-level highstand of 1.5m above the modern level reached between 6 and 5.5ky BP [25]. The HST sediment depocentre appears as a NE-SW elongated sediment body on the mid-shelf and is almost absent in the Northern part of study area where the river influences are less profound (Fig. 13). Location of the HST

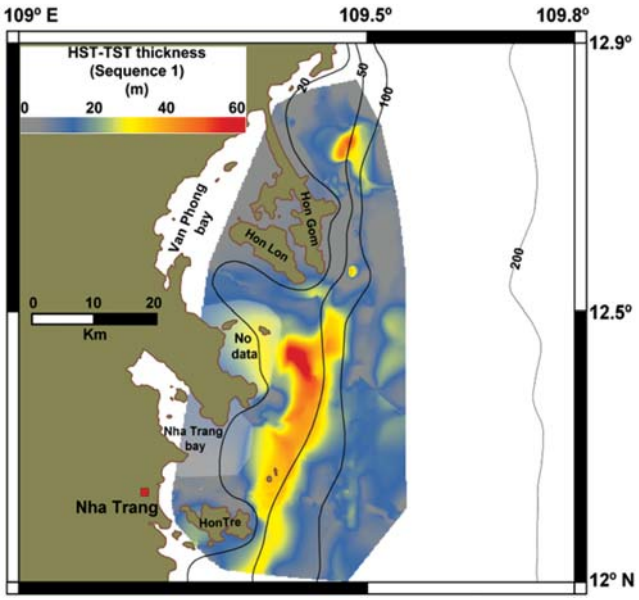

Fig. 12. *Total deglacial/Holocene sediment thickness (sequence 1) including U3 and U4 units. The sediment depocentre is located on the mid shelf*

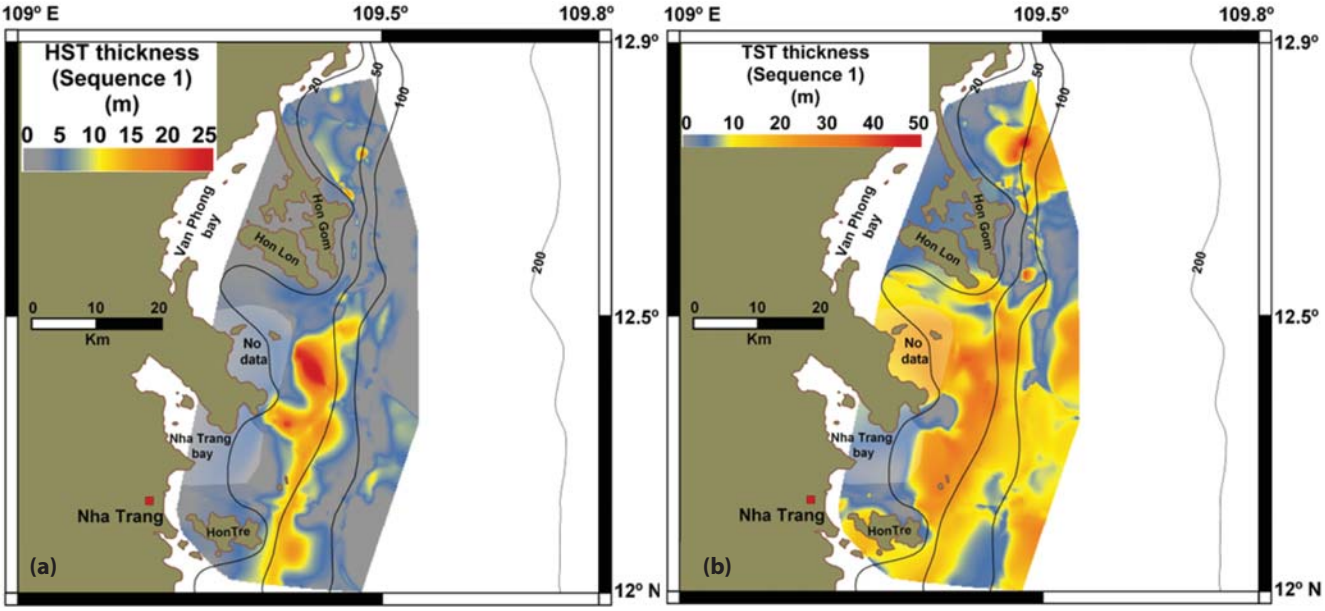

Fig. 13. *Sediment thickness map of HST (a) and TST (b) of sequence 1. HST depocentre is located on the mid shelf in front of Van Phong and Nha Trang Bay. HST deposits are probably transported along-shore Southward. The TST deposits develop over the shelf without significant sediment depocentre*

mud wedge suggests the importance of local rivers as the major sediment sources of the sediment depocentre. Hydrodynamic modelling studies indicate that the surface currents on Nha Trang and Van Phong Bay are mainly oriented offshore during summer and southward along-shore during winter [3]. Therefore, the major sediment supply to the shelf during the rainy season (accounting for 70% of sediment supply) is almost coincident with the beginning of the winter season (September to December). Sediments will be transported along-shore by the dominant NE monsoon effects or they can settle only around the river plume outflow on the inner shelf. Dispersion of fine material directly to the mid and outer shelf by the cross-shore sediment transport during this period is not significant. Since the inner shelf surface sediments are dominated by sands, reasonable sources of the modern fine sediments on the mid and outer shelf are assumed to be redeposited from the inner shelf via advection processes as well as transported along-shore from the Northern shelf [35].

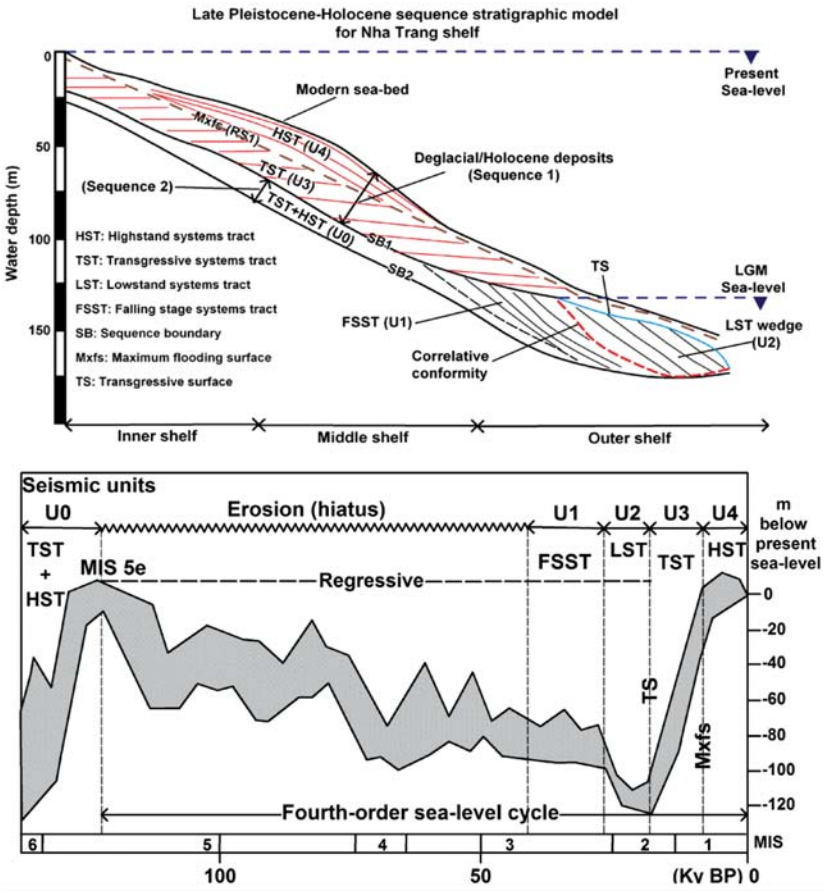

Fig. 14. *Late Pleistocene - Holocene sequence stratigraphic model for the Nha Trang Shelf (a) with regional sea-level curve (b) (Shackleton 1987; Chappell et al., 1996; Fleming et al., 1998; Hanebuth et al., 2004)*

5. Discussion and conclusions

The late Pleistocene high amplitude of sea-level change during a long fourth-order cycle (120ky) superimposed by several shorter fifth-order cycles is the principal factor in the organization of the Nha Trang continental shelf sequence (Fig. 14). The proposed sequence-stratigraphic model for the SE Vietnam Shelf basically follows the main features of the theoretical models of Vail and Zaitlin et al. [39, 43]. However, there still exist differences which are attributed to local controlling factors. On the Nha Trang Shelf, the thick mud highstand wedge is detached from the sediment source and forms the elongated mid-shelf mud belt. The formation of the mud-belt on the Nha Trang Shelf is probably correlated to the advection-dominated clinoform-progradation type according to Cattaneo's classification [7]. The LST deposits above the LGM surface on the inner and mid shelf are not documented on the Nha Trang Shelf since they were often eroded by subaerial and following marine erosional processes or they are not clearly discriminated by seismic resolution. Besides, the absence of the incised-channels due to transgressive erosional processes in this area did not allow the LST fluvial sediments, predicted to deposit at the bottom of the incised-channels, to be preserved [43]. Therefore the TS surface in the Nha Trang Shelf's model was mostly merged with the lowstand sequence boundary landward and TST deposits often rested directly on the LGM lowstand surface in the landward part of the LGM coastline. The variable gradient of the LGM surface influences the formation of sequence system tracts: The relative high-gradient on one hand has reduced the effects of the rapid transgression and on the other has prolonged the time for sediment reworking with a given amount of sea-level rise. As a result, the TST deposits on the Nha Trang Shelf were stacked thicker than their counterparts on the nearby low-gradient Sunda [20] and SE Vietnam [5]. On the other hand, the effect of transgression over longer time has also enhanced the marine erosional process of the lower regressive deposits and therefore reduced their preservation. This together with the high wave energy has resulted in the loss of the regressive deposits over the mid and inner part of Nha Trang Shelf.

The late Pleistocene - Holocene stratigraphic architecture on the shelf off Nha Trang area comprises five major seismic units and three bounding surfaces which can be attributed to four systems tracts: FSST, LST, TST and HST.

+ The lowermost unit U0 formed as transparent and parallel layer overlying the SB2 surface, and it is interpreted as deposits accumulated during MIS 5e transgression and highstand period of the last glacial cycle. The long gap between U0 and the following FSST unit is attributed to the erosional hiatus.

+ The FSST with unit U1 and LST with unit U2 are well preserved on the modern outer shelf but pinch out landward at water depths of 100 - 120m. FSST and LST units were primarily formed during the falling stage of sea-level from MIS 3 to the LGM sea-level lowstand of MIS 2. The LST wedge deposits on the central shelf are only recorded in the steep-gradient shelf off the Hon Gom Peninsula and they are almost absent in the other parts of study area. The relict beach-ridge deposits identified at a water depth of about ~ 130m below present sea-level indicate that the LGM sea-level lowstand in this area was lower than on the Sunda Shelf in the South. The difference probably resulted from subsidence due to high deglacial Holocene sedimentation and/or neotectonic movements of the East Vietnam Fault System.

+ Transgressive deposits (unit U3) were developed across the shelf with significant thicknesses. The TST shows a clear transition from backstepping to aggradational stacking patterns from outer to inner shelf which reflects the interplay between rate of sea-level rise, LGM surface gradient and sediment supply.

+ The thick highstand mud (unit U4) is documented on the mid shelf forming a shore-parallel sediment depocentre and its thickness decreases toward the inner and outer shelf.

+ The late Pleistocene high amplitude of sea-level change during a long fourth-order and superimposed shorter fifth-order cycle is the principal factor in reorganizing the formation of the Nha Trang continental shelf sequence. Local factors like geometry of the narrow shelf and high sediment supply from the mountainous hinterland provided specific features of the Nha Trang Shelf's sequence stratigraphy.

References

1. Allen SB. *Sediments of Nha Trang Bay, South Vietnam*. Am. Asso. Petr. Geol. Bull. 1967; 51: p. 454.

2. Badley ME. *Practical seismic interpretation: International Human Resources Development Corporation*. Boston. 1985: p. 266.

3. Barthel K, Rosland R and Thai NC. *Modelling the circulation on the continental shelf of the province Khanh Hoa in Vietnam*. Journal of Marine Systems 77. 2009: p. 89 - 113.

4. Bui VD, Dalman R, Weltje G, Stattegger K and Tran TD. *Flux and fate of sediments on the Nha Trang Shelf (central Vietnam) since the Last Glacial Maximum (LGM): field measurements and process-based numerical modelling*. To be submitted to Journal of Asian Earth Sciences.

5. Bui VD, Stattegger K, Phung VP and Nguyen TT. *Late Pleistocene-Holocene seismic stratigraphy on the South East Vietnam Shelf*. To be submitted to Global and Planetary Change.

6. Cattaneo A and Steel RJ. *Transgressive deposits: a review of their variability*. Earth-Science Reviews. 2003; 62 (3-4): p. 187 - 228.

7. Cattaneo A, Correggiari A., Langone L and Trincardi F. *The late-Holocene Gargano subaqueous delta, Adriatic shelf: Sediment pathways and supply fluctuations*. Marine Geology. 2003; 193 (1 - 2): p. 61 - 91.

8. Catuneanu O. *Sequence stratigraphy of clastic systems: concepts, merits, and pitfalls*. J. Afr. Earth Sci 35: p. 1 - 43.

9. Catuneanu O et al., 2009. *Towards the standardization of sequence stratigraphy*. Earth-Science Reviews. 2002; 92: p. 1 - 33.

10. Chappell J, Omura A, Esat T, McCulloch M, Pandolfi J, Ota Y and Pillans B. *Reconciliation of late Quaternary sea-levels derived from coral terraces at Huon Peninsula with deep sea oxygen isotope records*. Earth Planetary Science Letters. 1996; 141: p. 227 - 236.

11. Clift P, Lee GH, N Anh Duc, Barckhausen U, H Van Long, and Sun Z. *Seismic reflection evidence for a Dangerous Grounds miniplate: No extrusion origin for the East Sea*. Tectonics 27, TC3008. 2008.

12. Dam QM, Frechen M, Tran N, Harff J. *Timing of Holocene sand accumulation along the coast of central and SE Vietnam*. International Journal of Earth Sciences. 2010; 99 (8): p. 1731 - 1740.

13. Douglas IL and Nordstrom CE. *Sedimentation in Nha Trang Bay, South Vietnam- Am*. Asso. Petr. Geol. Bull. 1973; 57: p. 786.

14. Emch M, Feldacker C, Yunus M, Streatfield PK, Thiem VD, Canh DG and Ali M. *Local environmental drivers of cholera in Bangladesh and Vietnam*. American Journal of Tropical Medicine and Hygiene. 2008; 78: p. 823 - 832.

15. Fleming K, Johnston P, Zwartz D, Yokoyama Y, Lambeck K and Chappell J. *Refining the eustatic sea-level curve since the Last Glacial Maximum using far- and intermediate-field sites*. Earth Planetary Science Letters. 1998; 163: p. 327 - 342.

16. Fyhn MBW, Nielsen LH, Boldreel LO, Thang LD, Bojesen-Koefoed J, Petersen HI, Huyen NT, Duc NA, Dau NT, Mathiesen A, Reid I, Huong DT, Tuan HA, Hien LV, Nytoft HP and Abatzis I. *Geological evolution, regional perspectives and hydrocarbon potential of the Northwest Phu Khanh Basin, offshore Central Vietnam*. Marine and Petroleum Geology. 2009; 26: p. 1 - 24.

17. Grant J A and Schreiber R. *Modern swathe sounding and sub-bottom profiling technology for research applications: The Atlas Hydrosweep and Parasound Systems*. Mar. Geophys. Res. 1990; 12: p. 9 - 19.

18. Hanebuth TJJ, Stattegger K and Saito Y 2. *The stratigraphic architecture of the central Sunda Shelf (SE Asia) recorded by shallow-seismic surveying*. Geo-Marine Letters. 200; 22: p. 86 - 94.

19. Hanebuth TJJ, Stattegger K, Schimanski A, Lüdmann T and Wong HK. *Late Pleistocene forced regressive deposits on the Sunda Shelf (SE Asia)*. Marine Geology. 2003; 199 (1 - 2): p. 139 - 157.

20. Hanebuth TJJ and Stattegger K. *Depositional sequences on a late Pleistocene Holocene tropical siliciclastic shelf (Sunda Shelf, (SE Asia)*. Journal of Asian Earth Sciences. 2004; 23: p. 113 - 126.

21. Hanebuth TJJ, Stattegger K, Bojanowski A. *Termination of the Last Glacial Maximum sea level lowstand: The Sunda-Shelf data revisited*. Global and Planetary Change. 2009; 66: p. 76 - 84.

22. Hori K, Tanabe S, Saito Y, Haruyama S, Nguyen V, and Kitamura A. *Delta initiation and Holocene sea-level change: Example from the Song Hong (Red River) delta, Vietnam, Sediment*. Geol. 2004; 164: p. 237 - 249.

23. Lee GH and Watkins JS. *Seismic stratigraphy and hydrocarbon potential of the Phu Khanh Basin, offshore Central Vietnam, East Sea*. AAPG Bulletin. 1998; 82: p. 1711 - 1735.

24. National Project KC08.12. *Research on the preventative method of flooding processes on the central Vietnam*. Final report, Hanoi. 2004: p. 523.

25. Michelli M. *Sea-level changes, coastal evolution and paleoceanography of coastal waters in SE - Vietnam since the mid - Holocene*. PhD thesis. University of Kiel. 2008: p. 160.

26. Mitchum JR and Vail PR. *Seismic stratigraphy and global changes of sea-level: Part 7. Seismic stratigraphy interpretation procedure*. In: Payton, C.E. (Ed.), Seismic Stratigraphy-Applications to Hydrocarbon Exploration. AAPG Memoirs. 1977; 26: p. 63 - 81.

27. Pham VN (Editor). *Bien Dong Monograph*. Vol. II - Meteorology, Marine Hydrology and Hydrodynamics, Hanoi National University Publisher, Hanoi. 2003: p. 565.

28. Posamentier HW and Allen GP. *Variability of the sequence stratigraphic model: effects of local basin factors*. Sediment. Geol. 1993; 86: p. 91 - 109.

29. Shackleton NJ. *Oxygen isotopes, ice volume and sea-level*. Quaternary Science Reviews. 1987; 6: p. 183 - 190.

30. Schimanski A and Stattegger K. *Deglacial and Holocene Evolution of the Vietnam Shelf: Stratigraphy, Sediments and Sea-level change*. Marine Geology. 2005; 214: p. 365 - 387.

31. Steinke S, Kienast M and Hanebuth TJJ. *On the significance of sea-level variations and shelf paleomorphology in governing sedimentation in the Southern East Sea during the last deglaciation*. Marine Geology. 2003; 201: p. 179 - 206.

32. Shuttle Radar Topography Mission (SRTM) digital elevation models (http://srtm.usgs.gov).

33. Swift DJP. *Continental shelf sedimentation*. In: Stanley, D.J., Swift, D.J.P. (Eds.), Marine Sediment Transport and Environmental Management, New York. 1976: p. 311 - 350.

34. Szczuciński W, Jagodziński R, Nguyen TT, Kubicki A and Stattegger K. *Sediment dynamics and hydrodynamics during a low river discharge conditions in Nha Trang Bay, Vietnam*. Meyniana. 2005; 57: p. 117 - 132.

35. Szczuciński. W, Stattegger K and Schloten J. *Modern sediments and sediment accumulation rates on the narrow shelf off central Vietnam, East Sea*. Geo-Marine Letters. 2009; 29 (1), p. 47 - 59.

36. Tamura T, Saito Y, Sieng S, Ben B, Kong M, Choup S and Tsukawaki S. *Depositional faciess and radiocarbon ages of a drill core from the Mekong River lowland near Phnom Penh, Cambodia: evidence for tidal sedimentation at the time of Holocene maximum flooding*. Journal of Asian Earth Sciences. 2007; 29: p. 585 - 592.

37. Tamura T, Saito Y, Sieng S, Ben B, Kong M, Sim I, Choup S and Akiba F. *Initiation of the Mekong River delta at 8 ka: evidence from the sedimentary succession in the Cambodian lowland*. Quaternary Science Reviews. 2009; 28 (3 - 4): p. 327 - 344.

38. Thanh TD, Saito Y, Huy DV, Nguyen VL, Ta TKO and Tateishi M. *Regimes of human and climate impacts on coastal changes in Vietnam*. Reg Environ Change. 2004; 4: p. 49 - 62.

39. VAIL PR. *Seismic stratigraphy interpretation using sequence stratigraphy, Part 1: seismic stratigraphy interpretation procedure, in* Bally. A.W., ed., Atlas of Seismic Stratigraphy. 1987; Vol. 1: American Association of Petroleum Geologists, Studies in Geology (27): p. 1 - 10.

40. Veenken P C H. *Seismic Stratigraphy*. Basin Aanlysis and Reservoir Characterisation. 2007; 37: p. 509.

41. Wiesner M, Stattegger K, Kuhnt W, et al. *Cruise Report SONNE 140 SÜDMEER III*. Reports Institut für Geowissenschaften. 1999; 7: p. 157.

42. Wiesner M, Stattegger K., Voß M. et al. *Reports Institut für Geowissenschaften.* 2006; *23*: p. 99.

43. Zaitlin BA, Dalrymple RW and Boyd R. *The stratigraphic organization of incised valley systems associated with relative sealevel changes*. In: Dalrymple, R.W., Boyd, R., Zaitlin, B.A. (Eds.), Incised-Valley System: Origin and Sedimentary Sequences, SEPM Special Publications. 1994; 51: p. 45 - 60.

The Vietnam carbon dioxide storage capacity

Tran Chau Giang
Petrovietnam Exploration Production Corporation
Nguyen Anh Duc
Vietnam Oil and Gas Group
Nguyen Hong Minh
Vietnam Petroleum Institute

Our planet is warmed by a natural greenhouse effect and without this natural greenhouse effect the mean annual temperature on the earth would be about -6°C instead of its present level. Most of the natural greenhouse effect is known to be caused by water vapor and carbon dioxide in the atmosphere. However, water vapor is not classed as an anthropogenic greenhouse gas. Carbon dioxide is released into the atmosphere by the burning of solid waste, wood and wood products, and fossil fuels (oil, natural gas, and coal). As a result of human's activities, the concentration of CO_2 in the atmosphere has risen from a relatively stable level around 275 part per million (ppm) in the pre-industrial era to about 355ppm (1994), and currently continues to rise at a rate of about 1.8ppm per year. According to a study by the United Nations, Vietnam is in the top rank amongst countries hardest suffer by climate change catastrophes. In 2006, Vietnam had 10 typhoons of which 3 were particularly destructive, resulting in 500 people being killed and 2,900 injured. Sea dykes were broken, 86,000 houses were destroyed, 74,000 roofs were blown away and 3,300 ships sank or were damaged.

In order to restrict global temperature rise due to rising CO_2 emissions into the atmosphere, one idea of is to capture such CO_2 and store this gas in reservoirs almost completely shut off from the atmosphere in the deeper subsurface. This paper presents an assessment of the theoretical carbon dioxide storage capacity of deep-seated reservoirs in Vietnam's oil and gas fields.

The concept of underground CO_2 disposal

There are two main concepts for CO_2 disposal in aquifers. The first requires a subsurface trap for buoyant fluids with defined lateral boundaries (spill point) and a closed structure, an analogue to oil and gas fields. In the second concept, carbon dioxide is disposed of directly into aquifers without the need for further confinement to traps. In both cases, the storage reservoir requires a cap rock to prevent vertical migration of CO_2 to the surface and sufficient permeability to allow the injection of great quantities of CO_2. From natural CO_2 reservoirs and modeling results it is known that the migration behavior of carbon dioxide is fairly similar to that of natural gas. Thus, CO_2 disposal underground is similar to natural hydrocarbon accumulations, and carbon dioxide would be retained for millions of years underground, far longer than necessary to prevent its release into the atmosphere.

The concept of disposal of CO_2 into a closed structure is applied in onshore Europe, where the sedimentary basins are mainly small. Some of the aquifers in the deeper parts of these basins may be in direct connection with nearby outcrops. These aquifers may have other uses at shallow depth, for example water supply. Thus environmental constraints in the onshore area are likely to prevent the injection of CO_2 into an aquifer unless it is confined in a trap which will prevent it contaminating the useful parts of the aquifers. However, there may be some aquifers onshore which have no uses and are not connected to the surface onshore.

The second concept, which involves disposal into aquifers without the need for a closed structure to confine the CO_2, may be most widely applicable in large sedimentary basins where the aquifers have no current uses. In this case, carbon dioxide could be injected into an aquifer with only a top seal. If it was injected sufficiently far from the basin margins, reactions with the host rock and the surrounding formation water as is moved along a flow path within the aquifer would ensure that it did not emerge at the land surface or sea bed.

The storage capacity of aquifers in based on the available pore volume, and the CO_2 storage efficiency is the proportion of the pore volume that can be filled with carbon dioxide, in a fully water saturated reservoir with a hydrostatic pore pressure.

CO_2 disposal in oil and gas fields

The basic concept of CO_2 disposal in depleted oil and gas reservoirs is that the amount of CO_2 that can be stored in a reservoir is directly related to the amount of hydrocarbons that has been recovered from it. It is assumed that the reservoir volume of ultimately recoverable hydrocarbons can be replaced entirely by CO_2.

The major difference between CO_2 storage in aquifers and storage in hydrocarbon fields is that in the case of CO_2 storage in hydrocarbon fields a substantial volume of fluids or gases has been produced from the reservoir, will be replaced by CO_2 which enhances the storage capacity greatly. Additional benefits are that hydrocarbon traps have a proved capability to retain fluids and gases underground for thousands to millions of year and, based on the history of exploration and production, the reservoir is better understood. Moreover, some of the infrastructure used during hydrocarbon production may be re-used for CO_2 injection.

Vietnamese Cenozoic basins and their CO_2 storage capacity

Eight Tertiary basins have been identified in Vietnam comprising the Song Hong Basin, Phu Khanh Basin, Cuu Long Basin, Nam Con Son Basin, Malay - Tho Chu Basin, Tu Chinh - Vung May Basin and the group of Hoang Sa and Truong Sa Basins. Among these, petroleum potential has been confirmed in the Song Hong, Cuu Long, Nam Con Son and Malay - Tho Chu Basins. The inventory of the CO_2 storage potential of the Vietnamese Cenozoic Basins is based on the petroleum resource data. The pore rock volume of the CO_2 geological storage play is following petroleum play in hydrocarbon potential resources calculation (Table 2).

A play is a perception of how a producible reservoir, petroleum charge system, regional top seal and traps may combine to produce petroleum accumulation at a specific stratigraphic level. The geographical area over which the play is believed to extend is the play fairway. A play may be considered proven if petroleum accumulations are known to have resulted from the operation of the geological factors that define the play. In unproven plays, there is some doubt as to whether the geological factors actually do combine to produce a petroleum accumulation.

Plays are essentially reservoir defined. Hence, fairway at different stratigraphic levels in a basin may be stacked vertically. Within a single play, all leads, prospects and discovered fields share a common geological mechanism for petroleum occurrence. Petroleum accumulations, discovered or undiscovered within a single play fairway can be considered to constitute a naturally occurring population of geological phenomena.

This inventory is further restricted by the burial depth of potential reservoirs. Only deep reservoirs which have the appropriate pressures and temperatures necessary to retain the CO_2 in a dense supercritical state are considered for average gradients of 30°C/km and 10.5Mpa/km. Generally, the cutoff-level of 1,000m below mean sea-level is used. That means only reservoir sediments below a depth of 1,000m are considered. Here the indication is that even if CO_2 escapes from the reservoir, it will take a very long time for it to reach the surface; based on the result of modeling, it would take at least five thousand years before a large bubble of free CO_2 released at a depth of 1,000m would reach the surface. Another constraint is that the reservoir should have an average permeability of at least 100mD. If CO_2 is injected with sufficient pressure into an aquifer which is in open communication with the surface (an "open" aquifer), the CO_2 is able to displace the formation water. Displaced formation water may eventually flow into surface water, which may be an ocean or lake, or into groundwater. The pressure will be hydrostatic again when the conditions in the aquifer have reached equilibrium after CO_2 injection. In a reservoir connected to an aquifer system that does not communicate with the surface (a "closed" system), water displacement by CO_2 must be accommodated by compression of rock and interstitial water. If the reservoir volume is insignificantly small compared to the volume of the connected aquifer system, formation water flowing out of the reservoir into the aquifer system will lead to a negligible increase of reservoir pressure. The pressure will increase significantly if the reservoir itself is "closed".

If CO_2 is intended to be injected into an aquifer, the CO_2 must be able to permeate the aquifer at a reasonable rate with limited pressure losses. Based on modeling of the radial pressure behavior of CO_2 injected into an "open" aquifer at a depth of 800 - 1,800m, Van der Meer at al. (1992) concluded that with permeabilities smaller than 50mD, unacceptable pressure losses occurred. CO_2 injection under these conditions was not workable. Between 50 - 100mD, CO_2 injection is only feasible if wells are used that have a negative skin factor, i.e an improved flow performance at the bottom hole injection point. He therefore suggests a cut-off level of 50 - 100mD.

In the case of a "closed" aquifer, the volume of CO_2 injected must be accommodated by compression of the

reservoir. The most practical parameter for estimating how pressure increases due to injection is pore volume compressibility, which is a function of the porosity and/or net overburden pressure. If the pressure is increased by 10Mpa (100 bar), the pore water and formation is compressed by 0.8% for consolidated sand, leading to an "extra" pore volume that can be occupied by CO_2. For typical North Sea conditions, the pore volume compressibility will be 1.5 x 10^{-4} bar $^{-1}$ on average, and the compressibility of formation water varies between 0.39 x 10^{-4} to 0.45 x 10^{-4} bar $^{-1}$, i.e. the sum of water and the pore compressibility will be 1.9 x 10^{-4} bar $^{-1}$. This implies that if 2% of the reservoir pore volume is filled, the pressure will increase by 10.5Mpa, assuming 100% efficiency of the compression during the injection operation. It is concluded that only an aquifer with an average permeability larger than 100mD can constitute a suitable CO_2 reservoir. In the inventory below the Oligocene Play in the Song Hong Basin is eliminated from this inventory because of improved tight reservoirs (permeability < 1 mD). The CO_2 storage potential of the Vietnamese Cenozoic Basins is based on the petroleum resource data contained in the published document Geology and potential petroleum resource of Vietnam [3] in 2007.

The theoretical storage potential calculation is based on the assumption that 4% of reservoir pore volume can be filled with CO_2 and that 3% of reservoir volume is in a trap. An underground CO_2 density of 700kg/m^3 (i.e. dense supercritical) has been used. The storage capacity of the geological plays in Vietnamese Cenozoic Basins is calculated as follows:

$$Q_{Play} = Vp.\eta_{st}.\rho_{CO2}$$

Where: Vp = Total pore volume of the geological play below 1,000m (km^3).

η_{st} = Storage efficiency, i.e. fraction of the pore volume that can be filled with CO_2 (as shown in the Table 1.

ρ_{CO2} = CO_2 density at initial reservoir conditions (kg/m^3) applied as 700kg/m^3 by assuming a normal hydrostatic pressure (10.5MPa/km) and geothermal gradient (30^{o}C/km).

Q_{play} = Storage capacity of entire play (Mt CO_2).

Table 1 of CO_2 storage efficiency, i.e. the fraction of the reservoir pore volume that can be filled with CO_2, is based on the recommendations of the report: The Underground disposal of CO_2 - Joule II Project NO. CT-92-0031 [1].

Table 1. *Reservoir pore volume storage efficiency [1]*

Reservoir type	Storage efficiency
Closed trap	2%
Open trap	6%
Traps from which it is unclear if they are "open" or " closed"	4%

Table 2. *The theoretical storage capacity of the entire geological plays in Vietnamese sedimentary basins [2]*

Basin	CO_2 geological plays	Total Rock Vol. (km^3)	Total Pore Vol. (km^3)	Storage Capacity (Mt CO_2)
Song Hong	1. Fractured basement	7,928	250	210
	2. Miocene sandstone	12,472	561	471
	3. Miocene carbonate	7,866	1,038	872
	4. Pliocene sandstone	24,296	1,042	876
Phu Khanh	1. Fractured basement	3,505	105	88
	2. Miocene sandstone	15,188	683	574
	3. Miocene carbonate	17,262	2,184	1,834
Cuu Long	1. Fractured basement	41,308	1,446	1,214
	2. Oligocene sandstone	19,527	410	344
	3. Miocene sandstone	4,929	237	199
Nam Con Son	1. Fractured basement	3,505	105	88
	2. Miocene sandstones	18,693	1,346	1,131
	3. Miocene carbonate	5,091	386	325
Malay - Tho Chu	1. Miocene sandstones	10,807	389	327
Tu Chinh - Vung May	1. Fractured basement	7,886	237	199
	2. Oligocene sandstone	46,315	973	817
	3. Miocene sandstones	20,636	854	718
	4. Miocene carbonate/ Lower Pliocene limestone	1,289	105	88
Truong Sa	1. Fractured basement	na	na	na
	2. Paleogene sandstone			
	3. Miocene sandstone			
	4. Cenozoic carbonate			
Hoang Sa	1. Fractured basement	na	na	na
	2. Oligocene sandstone			
	3. Miocene sandstone			
	4. Miocene carbonate			
Total		**268,502**	**12,351**	**10,375**

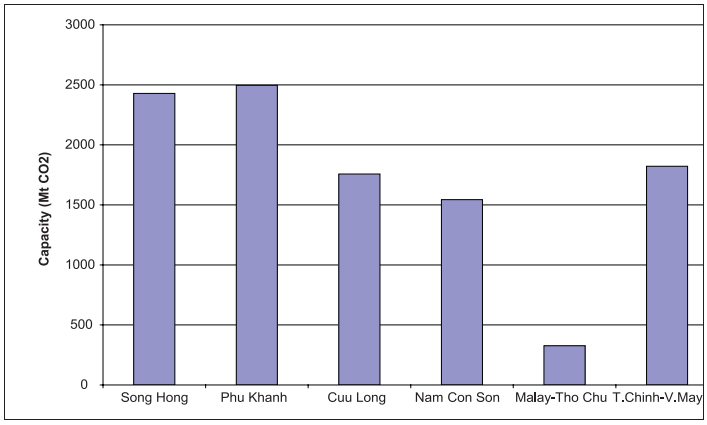

Fig. 1. *CO_2 storage capacity for Vietnam's sedimentary basins*

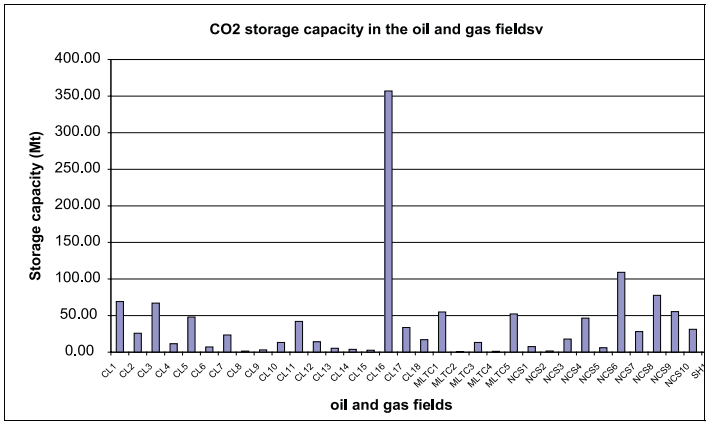

Fig. 2. *Vietnam's oil & gas fields CO_2 storage capacity*

Storage in oil and gas fields

The production in 2009 amounted to 8 billion cubic meters gas and 16.3 million tons oil (~20 million cubic meters oil under standard conditions, assuming an average crude oil density of 830kg/m^3 at standard surface conditions). The cumulative production by 2009 was 250 million tons or 300 million cubic meters of oil and 50 billion cubic meters of gas.

Currently, in offshore Vietnam, over thirty hydrocarbon fields are in production and or will be in the near future. The production data are restricted and information on temperature, pressure and the properties of the oil and gas are scatter. In order to be able to give a broad inventory of the CO_2 storage capacities of most oil and gas fields, this inventory has been based on these accessible figures. Additionally, only storage capacities of fields >10 Mt CO_2 are considered for use.

The theoretical storage potential of oil and gas fields in Vietnam is simply calculated using the following equations that applied in the RETA 7575: Determining the Potential for carbon capture and storage in Southeast Asia Project (Vietnam Ministry of Industry and Trade and Asian Development Bank co-project) [2]:

$$V_{Uoil} = V_{oil(st)} \times B_o / 1{,}000$$

$$V_{Ugas} = V_{gas(st)} \times 1/GEF$$

$$Q_{CO2} = (V_{Uoil} + V_{Ugas}) \times \rho_{CO2}$$

Where: V_u = Underground volume of oil or gas (millions m^3)

$V_{oil(st)}$ = Recoverable volume of oil at standard conditions (millions sm^3)*

$V_{gas(st)}$ = Recoverable volume of gas at standard conditions (millions sm^3)

Bo = Oil formation volume factor

GEF = Gas expansion factor

ρ_{CO2} = CO_2 density at initial reservoir conditions (kg/m^3) applied as 700kg/m^3 by assuming a normal hydrostatic pressure (10.5MPa/km) and geothermal gradients (30^{o}C/km)

Q_{CO2} = Total CO_2 storage capacity (Mt)

The theoretical storage capacity of the current oil and gas fields in Vietnam is estimated to amount to 1.15Gt CO_2, and Fig. 2 shows the largest field exceeds 350Mt CO_2 capacity.

To conclude, Vietnam has the capacity to store megatons of CO_2. The theoretical cumulative storage capacity of Vietnam's sedimentary basins exceeds 10Gt of CO_2 (Table 2), an order of magnitude larger than that calculated for Vietnam's Oil and Gas fields of 1.15Gt. As the geology of Vietnam's basins becomes better defined, this number will become more precise. However, the storage number is large enough to justify further quantification of Vietnam's geological storage potential.

References

1. *The Underground disposal of CO_2* - Joule II Project NO. CT-92-0031. ADB sources.

2. RETA 7575: *Determining the potential for carbon capture and storage in Southeast Asia, Viet Nam Country Report - Summary* (Vietnam Ministry of Industry and Trade and Asian development Bank co-project, 2011).

3. *Địa chất và Tài nguyên Dầu khí Việt Nam*. NXB Khoa học - Kỹ thuật. 2007.

** Standard conditions are at 20^{o}C and 0.1 MPa (1bar).*

The 4D Experience in TOTAL

E. Brechet, S. Maultzsch,
A. Grandi, O. Rahmanov, C. Hubans
Total

Born nearly thirty years ago, time lapse (4D) seismic monitoring technology has been developed in such a way that it has finally proven to monitor fluid movement and to distinguish between drained and undrained portions of a reservoir. Its ultimate aim is to quantitatively improve reservoir models, particularly their predictive capability. Indeed, the benefits of time-lapse seismic for reservoir characterisation depend on the quality of 4D acquisition and processing, but they also greatly depend on the particular 4D inversion and interpretation schemes used; finally, a decisive aspect is certainly also the capability of integrating results from different disciplines in an effective way. In fact, the 4D success comes through close interaction between Geophysicists, Geologists, Rock Physicists, Geomechanicists, Reservoir Engineers and Drillers. Timing is also crucial: results delivered in a few months can have a direct operational impact such as optimising well locations.

For the last ten years, Total has recognised the importance of time lapse seismic and has therefore conducted 4D seismic monitoring in different geological environments. Examples of 4D experiences range from monitoring of water injection and production for reservoir management and field development in the Gulf of Guinea (Angola Block 17, and Nigeria); monitoring of geomechanical effects in HPHT fields (Elgin-Franklin, UK), in compacting reservoirs in Norway (Ekofisk and Valhall) and in the Gulf of Mexico (Matterhorn, US); monitoring of steam chamber in tar sands (Surmont, Canada) and monitoring of compaction and water rise in carbonates (South-East Asia).

To illustrate capabilities of time lapse seismic monitoring two cases are presented. The first case is a deep offshore field in Angola with turbiditic stacked channel reservoirs with a good 4D response. The main 4D effect is given by fluid substitution and in particular by gas both injected and generated by a small depletion, the initial pressure being close to bubble-point; in this case the seismic quality and repeatability are outstanding and in fact the fluid change in the reservoir is very well resolved. The second example pertains to an HPHT field in the UK where the seismic quality is degraded due to the extreme depth of reservoir burial (>5000m) as well as the vicinity of the platform. It shows 4D effects due to a dramatic pressure drop; it is a significant result because it shows that appropriate tools enable achieving reliable results even in critical conditions.

Block 17, Angola, the Dalia Field

Geological & field development context

The deep offshore fields operated in Angola (Block 17) are composed of confined and unconfined unconsolidated turbidite sands aged from Miocene and Oligocene at an average depth ranging from 2,200 to 2,800m subsea with an average water depth of 1,300m. Three fields, named Girassol, Dalia, and Rosa were discovered in the Mid 90's and started producing in 2001 for Girassol, 2006 for Dalia and 2007 for Rosa. These turbidite fields are known for their strong heterogeneities, which imply complex fluid communications and dynamic behaviour which must be fully understood before drilling the significant number of development and infill wells required.

Geophysical context

On Block 17, seismic data are of very good quality with a dominant frequency between 50 - 60Hz and a vertical resolution from 7 to 10m. After one year of production a 4D seismic was shot on these fields in order to monitor development wells (water injection efficiency, depleted areas), understand reservoir communications (vertical communications, fault behaviours), but also prepare the next development and infill wells. Owing to positives results obtained from the first 4D survey, a two year periodicity between monitor surveys was planned.

Due to the field environment (unconsolidated sands and shallow burial), 4D effects are very strong and time shifts due to fluid changes larger than 10ms have been

observed on the Dalia Field. Post-stack processing and interpretation techniques were optimized in order to fully interpret 4D effects and integrate them into the reservoir model.

For all three fields, three production mechanisms are present: water injection, gas injection and depletion. As reservoir pressures of these fields are close to the bubble point, migration of dissolved gas occurred with depletion.

In order to generate a reliable 4D signal, an in-house warping inversion was used to retrieve the relative velocity changes (dV/V) due to production between the two seismic acquisitions (Fig. 2). In areas adjacent to producers, depletion of around -10 to -40 bars associated with the appearance of dissolved gas is observed. This induces a decrease of P-velocity (Gassmann's theory) whereas fluid pressure decrease (increase of effective pressure) induces an increase of P-velocity according to laboratory measurements. In the case of Dalia, the pressure effect is negligible, and the main effect is a P-wave velocity decrease. Around water injectors two effects are observed: when injecting water in the oil pool, one observes an increase of P-velocity, whereas injecting water in the water pool yields a decrease of P-wave velocity due to salinity differences between injected water and aquifer.

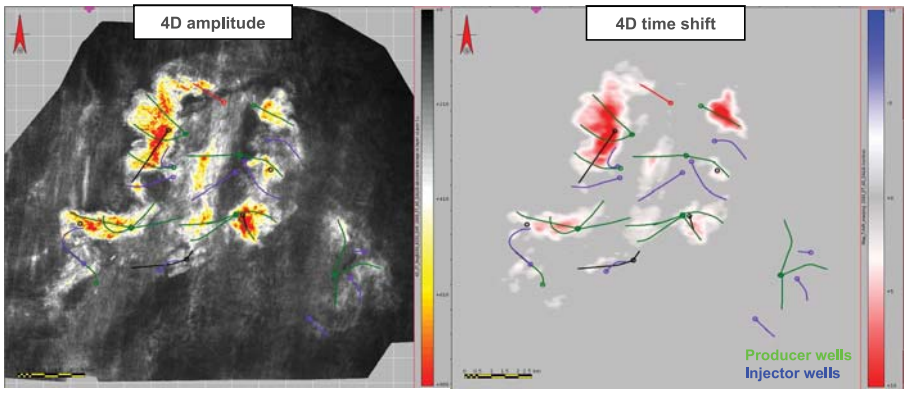

Fig. 1. *Fast track amplitude differences over the reservoir interval of Dalia (left) and associated time shift of the reservoir in ms (right)*

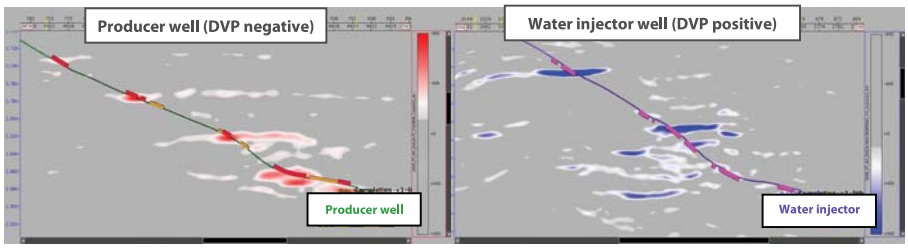

Fig. 2. *Warping results: time re-alignment of monitor seismic data. Illustration of a depleted area around a producer which induces a strong pull down*

4D results

4D results on the Dalia Field improved the understanding of geological heterogeneities, fluid pathways and therefore helped the reservoir management. Here are short-listed the domains where 4D brings useful information:

+ Reservoir management by understanding well injection and production efficiency coming from the interpretation of 4D anomalies. This has an impact on the understanding of water breakthroughs at producers.

+ Identification of depleted areas and impact on the positioning of development wells.

+ Understanding of the vertical dynamic communication through erosion and degraded facies inside turbiditic channels and lateral communication between turbidite deposit systems.

+ Fault behaviour with connecting faults and partially sealing faults.

+ Rise of the oil-water contact within several turbiditic lobes, which were not predicted by reservoir models.

Fig. 3 shows an important contribution given by 4D in understanding water breakthroughs of four producers. Without 4D results it would have been impossible to know the origin of the produced water (aquifer or a specific water injector well), and the role of faults in inhibiting or allowing fluid flow would not have been known.

Fig. 4 shows how 4D attributes helped understanding the vertical communication in stacked channels and inter-system communication. 4D anomalies were confronted with geological and dynamic knowledge of the field: The vertical dynamic communication, seen on MDT pressure measurements, occurs in areas where sand channels erode each other for example.

Another important issue is the role of faults in the dynamic flow. On one of the systems, which is heavily faulted, several

4D anomalies (anomalies of depleted areas) terminate along fault directions and some other anomalies (water injection) seem spread out along fault directions. 4D seismic data correlated to dynamic information and structural knowledge proved a useful resource in understanding the dynamic role of faults. The Dalia Field contains two fault families N45 and N160. The first family of N45 faults show fault relays and very large water injections anomalies around them. These faults behave as non sealing faults and as drains for water injectors. The second fault family (N160) delimits many depleted areas and seems to reduce the fluid transmissibility.

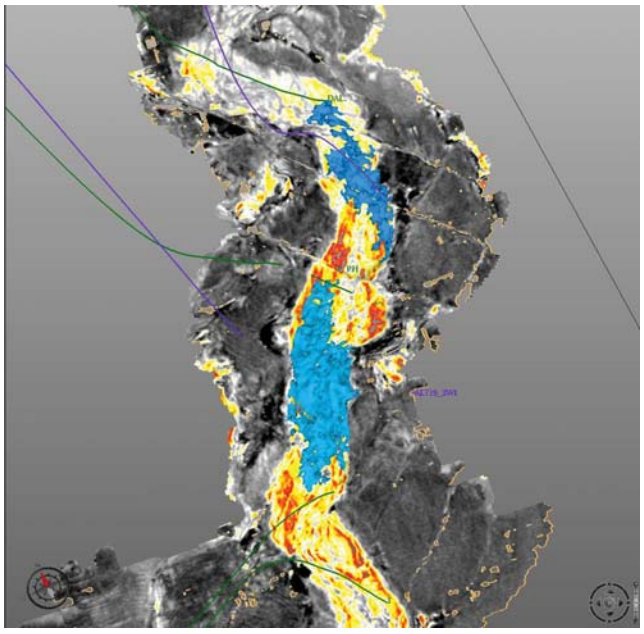

Fig. 3. *Water injection efficiency of two water injectors: Water is reaching producers. Some faults reduce water injection efficiency in the North*

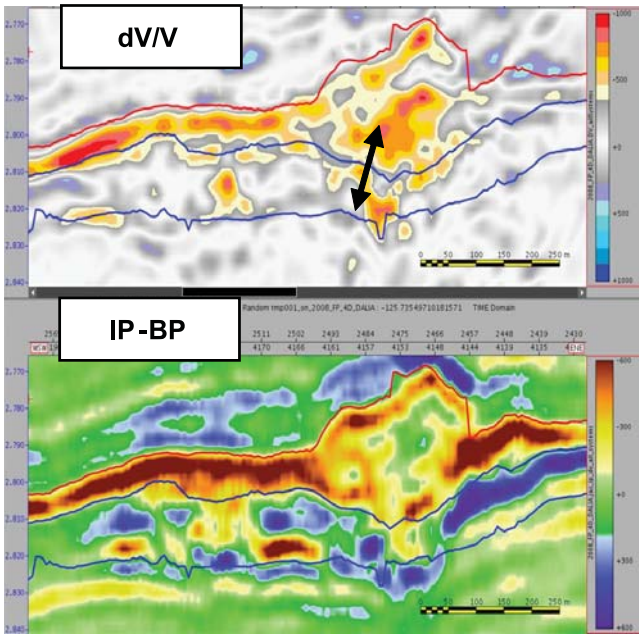

Fig. 4. *Example of vertical communication between lobes*

For unconfined turbidites (lobe types), we observed water front movements on some lobes (Fig. 5), which help to locate future producers up-dip of aquifers. Thus the 4D assists in preventing early water breakthroughs and helps for reservoir model history matching.

North Sea Central Graben, UK, Elgin Field

Geological & field development context

The Elgin Field, located in the UK North Sea Central Graben, is an extreme HPHT field. The initial reservoir pressure is in the region of 1,100 bars and the bottom hole temperature around 200°C. The Jurassic sandstone reservoirs, buried some 5,300m below sea level exhibit permeabilities ranging from a few tens of mDarcy to 1 Darcy. Three main reservoir units are identified, from top to base: Fulmar C sands, of moderate reservoir quality; Fulmar B sands which have the best reservoir properties and are the main contributor to production; and Fulmar A sands, which are generally of poor quality. The overall Fulmar sand pay thickness is about 170m with an average porosity of about 19%. The cap rock is formed by Upper Jurassic shales of the Heather and Kimmeridge formations.

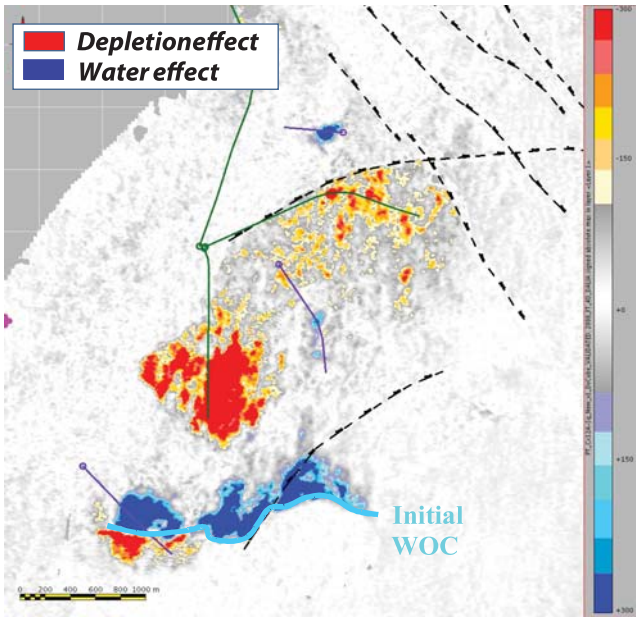

Fig. 5. *dV/V attribute extracted on a lobe showing in the South the water front movement and water injection efficiency of the South injector in oil pool (positive dV/V) and in water pool (negative dV/V)*

The Elgin Field was discovered in 1991 and brought on stream in 2001. Typical of most HPHT fields, reservoir pressure dropped rapidly in the first few years of production. The early rate of pressure depletion on Elgin was about 100 bars every six months. The initial development plan did not consider re-entering highly depleted areas technically feasible and hence all the development wells were drilled before start of production.

Geophysical Context

In order to monitor the pressure drop across the field and investigate the stress redistribution in the overburden induced by reservoir compaction (with a corresponding measurable effect on seismic velocities and travel times), a 4D seismic survey was acquired in 2005. The two expected main benefits of the 4D seismic survey were identification of un-depleted fault compartments, and the calibration of the geomechanical model. Indeed, although not part of the business case, another important aspect is the identification of areas where well integrity was at risk (casing/liner deformation or rupture).

4D results

Time-lapse seismic monitoring has improved the understanding of the Elgin HPHT field. It helped assisting infill drilling by minimising risks of well failure. It improved understanding of compartmentalisation, flow connectivity and reservoir quality away from control wells.

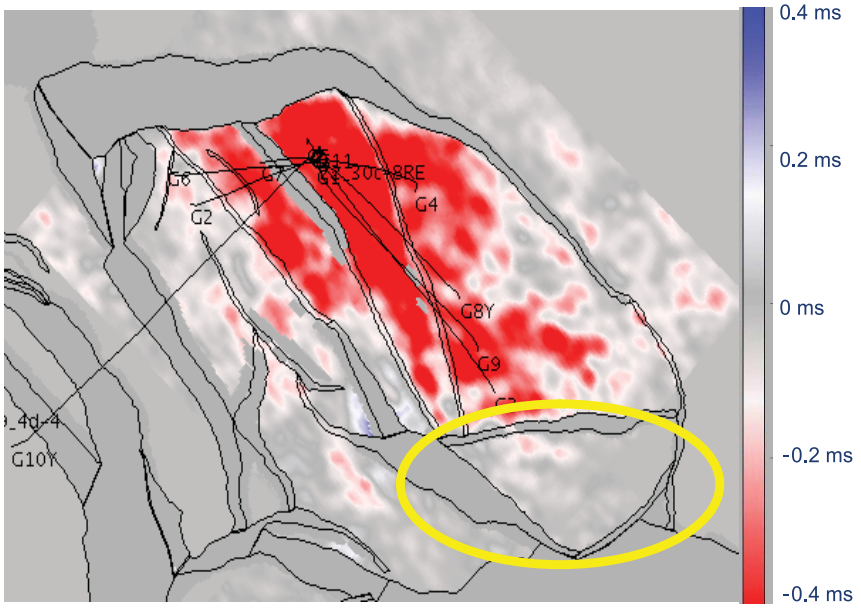

Fig. 6. *Time-Shift cumulated within the B sands layer*

The most important results were:

Identification of un-depleted panels: The 4D inversion, performed in the overburden and within the reservoir, shows the relaxation of the overburden associated to the reservoir compaction and associated relaxation of the overburden. Within this time strain attribute, a delineation of depleted panels versus un-depleted was performed, showing un-depleted panel in the South-East (Fig. 6).

- Calibration of the geomechanical model: 4D attributes show positive time shifts in the overburden, indicating the relaxation of the overburden and negative time shifts in the reservoir associated to compaction. This geomechanical effect is not only seen on Elgin but also on nearby fields such as Franklin and Shearwater. 4D time shifts where used to calibrate the geomechanical model and reservoir simulation models.

- Assistance in infilling well: geomechanical model calibrated by time lapse seismic results in the overburden (Fig. 7) provided accurate mud weight windows during infill drilling operations enabling to re-enter highly depleted reservoirs. Moreover 4D results helped understanding and predicting geo-hazards related to high pressure gas intervals in the overburden.

- Reservoir model update: the reservoir model was updated and reserves were secured.

- Reservoir quality far from control wells: 4D results highlighted possible facies degradation in the eastern panel of Elgin.

Conclusion

Today, a number not too far from one hundred fields are covered by 4D seismic and this number is growing fast. In Total, 4D acquisition has proven to be an excellent enabler for improved reservoir management and hence an important source for value creation in the petroleum industry. 4D has always been positively used with direct impact on the field development (well planning, reservoir management, well integrity). Total's experience in this technology lies mainly in clastic or chalk offshore oil reservoirs as well as in tar sands.

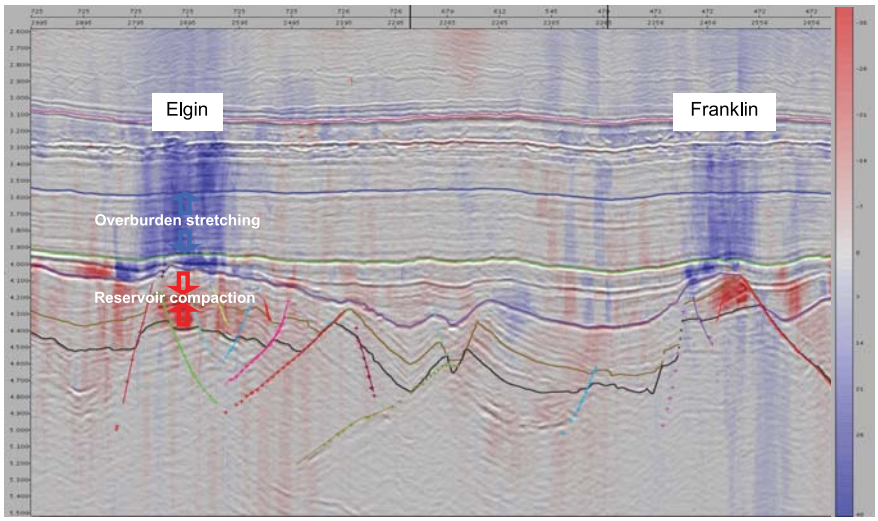

Fig. 7. *Time strain (4D attribute given by the sum of compaction and relative velocity change) on a line across Elgin and Franklin fields*

A Business Case approach prior to sanctioning a 4D project is a good way for evaluating the stakes and issues of the field. It gathers all disciplines in order to put in perspective the different issues and possible actions for the field management/development. In many cases the benefits initially expected were fully confirmed. However, very often there have been additional benefits which were not foreseen or evaluated prior to interpretation. These unanticipated benefits sometimes appear to be the major value of some 4D surveys.

We have learned that 4D projects must be anticipated in the Field Development Plan, since the global 4D process can be long, as acquisition, processing, inversion and interpretation request significant time and have to be successfully timed. 4D feasibility studies have proven to be essential in generating questions and anticipating possible problems. A crucial part of its feasibility is represented by rock physics, which enables to identify 4D seismic effects by studying fluids, pressure, temperature and salinity parameters depending on the production process.

The two examples discussed in this paper show practical applications on improved understanding of the fields and therefore on field development. In Total 4D seismic is considered a fundamental tool for reservoir monitoring and, thanks to in-house inversion techniques and interpretation, its impact on reservoir management, infill and development wells as well as reservoir dynamic communications understanding is dramatic. A number of patents were filed to protect our know-how on 4D inversion and demonstrate that Total has pushed technology to anticipate future trends.

Although an extensive use of time-lapse seismic has been made mainly in a qualitative sense, we expect a usage in a more quantitative way where reservoir flow simulation and 4D seismic are merged in an attempt to provide largely improved forecasts of reservoir behaviour. Such a progress would have a major impact on the future of 4D seismic in the Industry.

The 4D workflow (planning, Business Case study, feasibility, acquisition, processing, interpretation and integration) adopted by TOTAL appears well appropriate. This process is being improved continuously. Amongst all the key factors, the most important aspect in making a time-lapse project successful are:

- Integration of both expertise and data anlalysis/ management between different disciplines: Geology, Geophysics, Geomechanics, Reservoir Engineering, Rock Physics and Drilling,
- Anticipation and effective 4D feasibility study,
- Quick turnaround time,
- Inversion and interpretation techniques adapted to the specific challenges of every given field case.

Acknowledgments

The authors wish to thank TOTAL and co-venturers for permission to publish this work:

- TOTAL Angola and the Block 17 concessionaire Sonangol and its partners Statoil, ExxonMobil and BP
- The Elgin Franklin co-venturers: TOTAL E&P UK Ltd, ENI UK Ltd, BG Group, GDF SUEZ, E.ON, Ruhrgas UK E&P Ltd, Esso E&P UK Ltd, Chevron, Dyas, and Summit Petroleum.

Thanks also to the many assets, specialists and advisors who have helped and advised on the paper.

Numerical simulation of bottomhole flow filed of PDC bit with side nozzles

Hoang Anh Dung, Le Hai An
Hanoi University of Mining and Geology
Li Gensheg
China University of Petroleum

Abstract

To analyze the effects of a steerable nozzle on the flow field at the bottomhole, CAD software in conjunction with Gambit is used to design PDC drill bit models with steerable nozzles. Fluent flow modelling was then used to perform flow simulations at the bottom of the hole. The research results show that the assemblage of steerable nozzles has maximized the hydraulic energy of two jet streams to enhance drill cuttings cleaning and minimize the formation of mud in drill mud PDC to ultimately improve the mechanical drilling rate.

Introduction

For conventional nozzles (single-hole nozzle drill bit), there one stream from the nozzle outlet so it is not possible to maximize the effect of the hydraulic energy of the jet stream in the bottomhole and drill bit surface cleaning. In order to overcome this phenomenon experts have proposed a plan for designing new nozzles, called the steerable nozzles, installed on the drill bit.

This nozzle type appeared as early as in 1962 and was installed to a 3-cone rotary drill bit. In 1998, Winton and Dickey carried out installation of a steerable nozzle on a PDC drill and yielded good results [1]. In recent years steerable nozzles has been extensively used, proving their superiority in terms of cleaning surface and bottomhole drill during drilling [2].

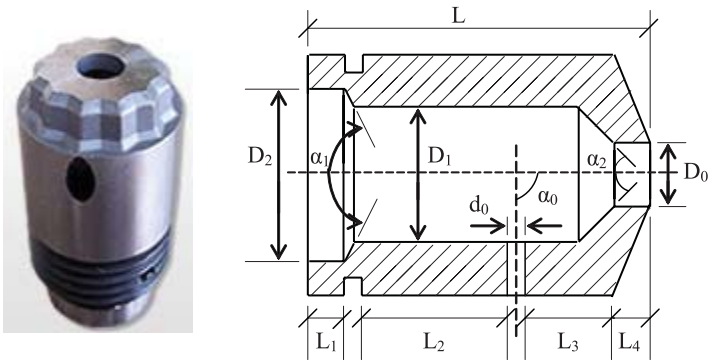

Fig. 1. *The structure of directional nozzle*
L: Length of the nozzle; D_2: Diameter inlet of the nozzle; D_1: Diameter in of the nozzle; D_0: Diameter outlet of the main nozzle; d_0: Diameter outlet of nozzle on the body; α_2: Spray angle outlet of the main nozzle; α_0: Spray angle outlet of nozzle on the body; α_1: Spray angle inlet of the nozzle.

To analyze the effects of steerable nozzle of PDC drill on bottomhole flow field, the author has used the combination of CAD software in conjunction with Gambit to design a steerable nozzle PDC drill simulation and then applied fluent flow modelling to examine simulated characteristics of the flow field of the steerable nozzle in the bottomhole.

1. Steerable nozzle assemblage

The structure of steerable nozzles when compared with conventional nozzle has one or more extra nozzles on the body of spray. called a tilt steerable jet stream (Fig. 1).

The assemblage parameters of nozzle geometry including size and shape of the nozzle flow path... Depending on the size and type of PDC drill, the parameters of the nozzle will be determined [3].

The direction of the jet axis and tilt axis of the spray nozzle forms an angle (α_0) that is controlled in the range from 45 to 90 degrees, the magnitude of α_0 being influenced by the assemblage of the drill. If using small angle smaller than 45 or greater than 90, the flow direction injection nozzle flows will impact directly on the body of the drill bit or the impact

with drilling equipment on the borehole surface that ultimately reduces the efficiency of cleaning surface and bottomhole drill orientation of the nozzles [4].

The diameter outlet of the main nozzles (D_0), the diameter outlet of the nozzles on the body (d_0) and the distance between them (L_0) has a strong influence on the hydraulic characteristics of the jet stream. To ensure the outlet energy of the nozzles outlet is stable, the diameter (d_0) must be relatively smaller than the (D_0) and must meet the conditions $0.2 < d_0/D_0 < 0.4$. In addition, when choosing the nozzle diameter it is necessary to ensure no clogged jets by large particles of drilling mud flowing back into the injector pump when pumping is stopped [5].

2. Modern design and calculation conditions

The calculation parameters were selected as follows: drill diameter is 215.9mm diameter in of the nozzle D_1 = 15mm, flow rate of inlet nozzle Q = 32L/s, speed of the nozzle inlet 45.3m/s, the diameter of the nozzle outlet is designed as D_0 = 9mm and d_0 = 3mm, distance between nozzles L_0 = 10mm), relative angle of the jet flow direction inclined to the main injection was designed as α_0 = 45 and α_0 = 60, rotary drill bit speed is 120rph, working fluid is water.

The azimuthal position of the nozzle is determined according to four directions A, B, C, D along OO relative azimuth and is distinguished by the clamp angle 62, 38, 60, 35, and must ensure that all the bottomhole is covered by the spray from the nozzle. The installation locations of the nozzles are arranged on the circumference of a circle with various radii from the center of the nozzle to the central axis. Moreover, in order to clean the mud at the bottomhole and the mud layer covered drill strings, the jet flow direction of the main spray nozzle (diameter D_0) is tilted at a suitable angle, and the jet flow direction of the tilt nozzle (diameter d_0) must be arranged parallel to the surface of the appropriate blades (Fig.2) [6].

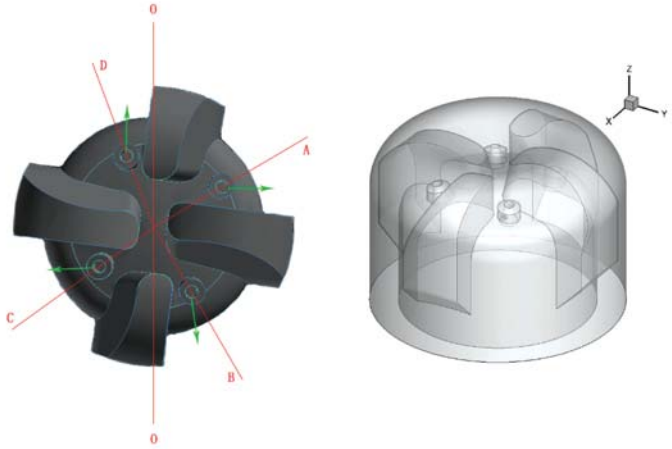

Fig. 2. *Nozzle arrangement diagram*

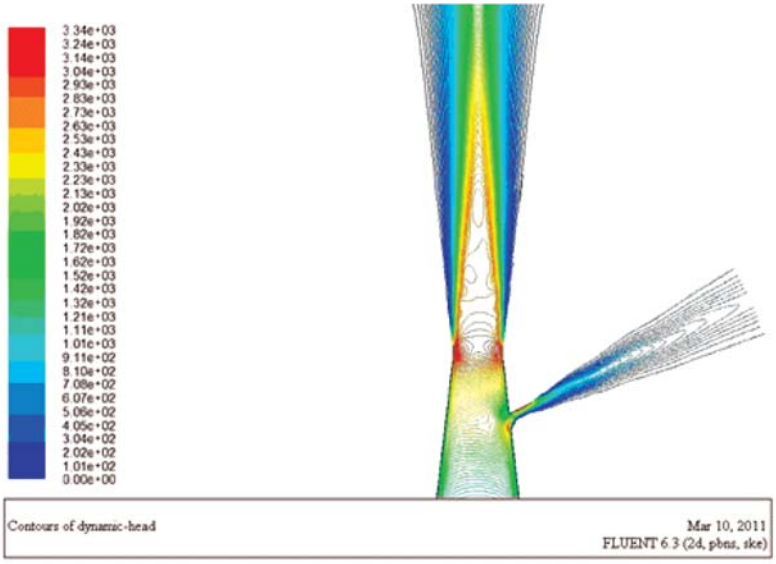

Fig. 3. *The dynamic head isoline of directional nozzle center section (α_0 = 60°)*

When designing the model parameters, the three-dimensional model of PDC drill steerable nozzle and the physical model of the flow field flow at the bottom of the well were designed in CAD software in combination with Gambit in order to optimize the designed models. Fluent flow modelling was then used to perform the simulations of efficiency of steerable nozzle to the flow field characteristics at the bottomhole.

3. Analysis of the effects of steerable nozzle to the low current at bottomhole

3.1. The effect of tilt angle (α_0)

Distribution problems inside the nozzle flow is an important indicator in determining the function of a steerable nozzle. The working efficiency of the injector nozzle is always better than a conventional nozzle because of more support from the tilted jet stream in the process of cleaning the drilling mud covered drill bit. The scope of coverage and speed of the tilted jet stream will determine the efficiency of cleaning the mud. When the angle (α_0) is small, the distribution characteristics of

the flow in the nozzle is relatively good,, creating high spray rate and extent of the coverage of tilted spray that consequently benefits the cleaning and limits the mud formation in the drill bit [7]. Based on the limited angle ($45 \le \alpha_0 \le 90$) and in order to create favourable conditions for the spray manufacturing processes, the values of α_0 = 60 and α_0 = 45 were chosen to conduct simulation.

The result of the simulation process is shown in Fig. 3 and Fig. 4, confirming that with a smaller angle the spray coverage and the speed of the spray would be better. So, when designing steerable nozzles installation on PDC drill, the selected angle α_0 = 45 is the most appropriate one to create good and effective cleaning and limit the formation of mud in the drill bit. It also makes for conveniences in manufacturing steerable nozzles.

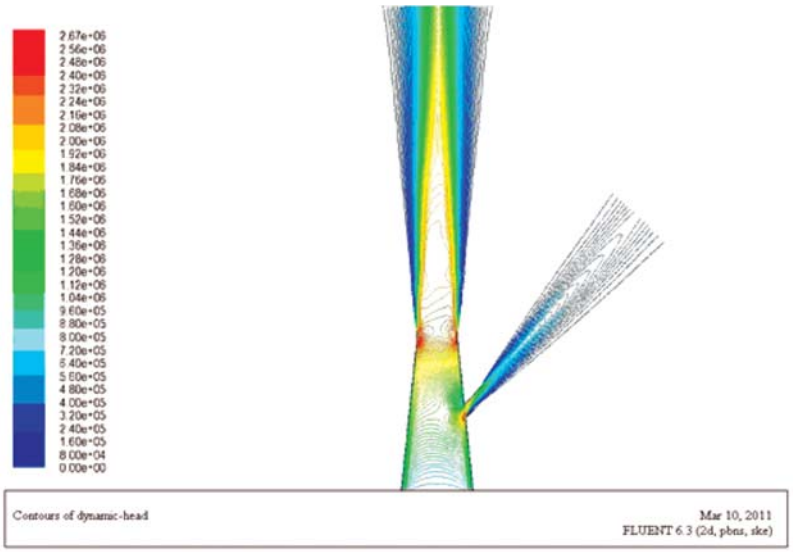

Fig. 4. *The dynamic head isoline of directional nozzle center section (α_0 = 45^0)*

3.2. Effect of steerable nozzle on the flow field at the bottomhole

The influence of a conventional nozzle on the flow field at the bottomhole is categorized into four main areas: the impact area, the flow out area, the counter flow area and the turbulent flow area [8]. The impact area supports the more effective process of destroying rock, the flow out area helps cleaning drill cuttings from the bottomhole, the counter flow area carries drill cuttings to the surface, while the turbulent flow region, due to the flow rate, speed and pressure is relatively low, and prevents the upward push of drill cuttings. Therefore, to limit the influenced region of the turbulent flow area and to support mud cleaning processes, the steerable nozzle is proved to work very well when compared to a conventional nozzles. The result of simulation is displayed in Fig. 5 and 6.

From Figs.5 and 6, it was shown that when compared with a conventional nozzle, the spray assemblage of the steerable nozzle raises some issues with the participation of the tilted jet stream. In the flow out area of the main jet stream, the further support of a tilted stream is recognized, which is very beneficial to the process of cleaning drilling cuttings at the bottomhole. Simultaneously, in the area of turbulent flow of the main jet stream with strong support from the tilted jet stream, there would form a new impact flow area which, though weaker than that of the main jet stream, works very well to reduce the coverage area of the turbulent

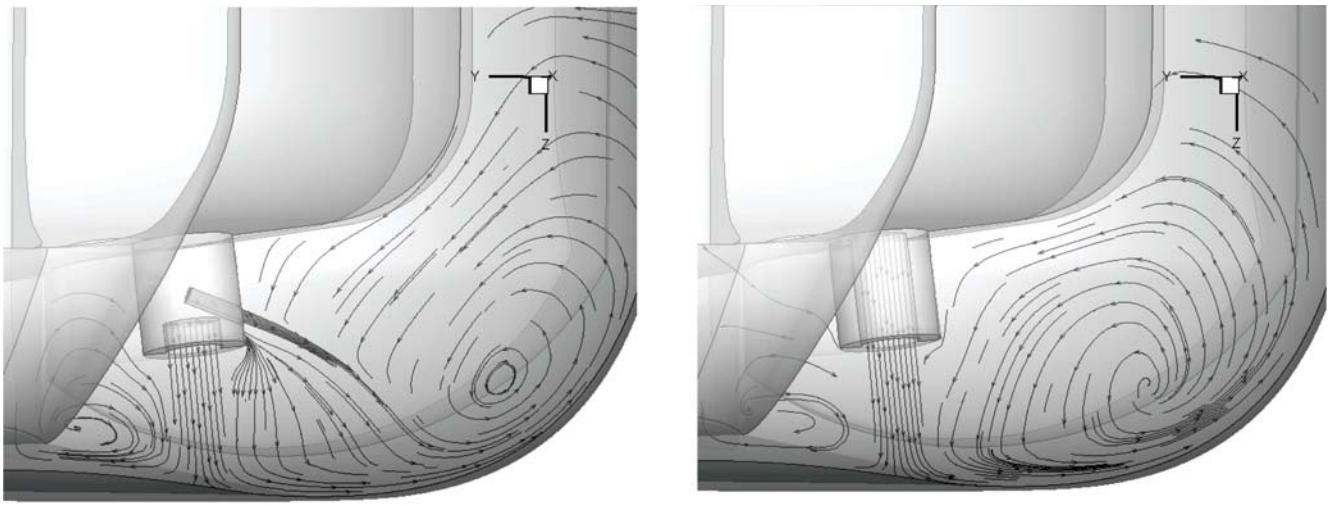

Fig. 5. *The flow graph of bottom - hole section (a - directional nozzle; b - conventional nozzle)*
1 - The impact area; 2 - The flow out area; 3 - The counter flow area; 4 - The turbulent flow area.

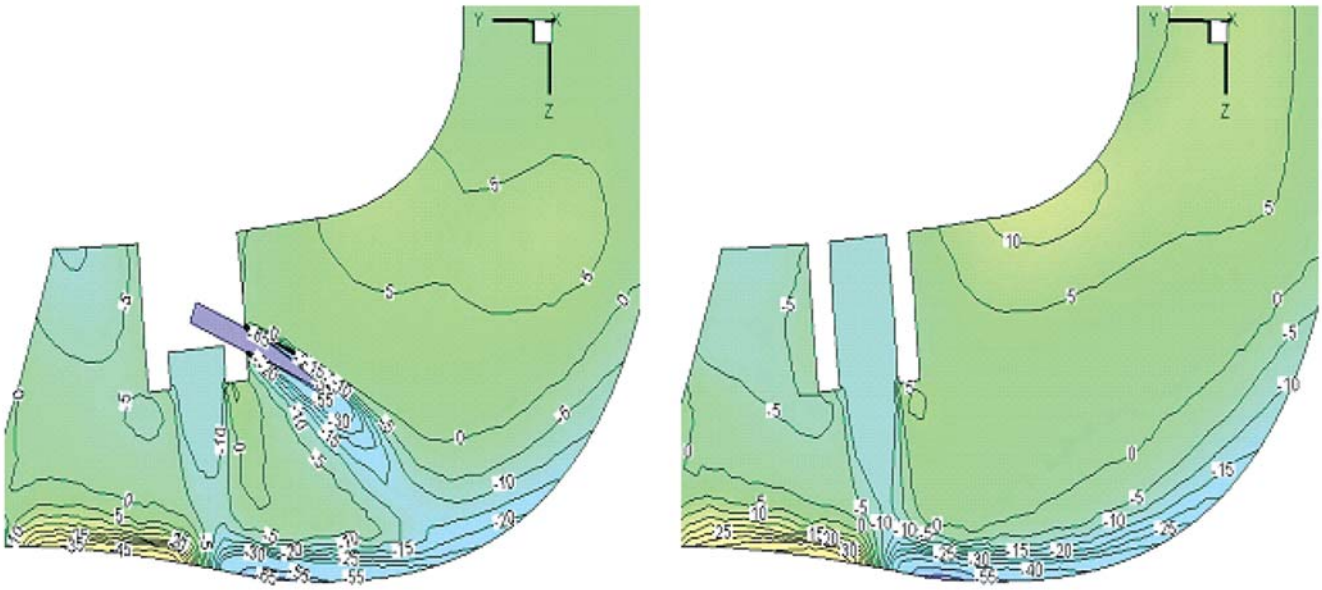

Fig 6. *The isoline of bottom lateral velocity (a - directional nozzle; b - conventional nozzle)*

flow, which is extremely beneficial for pushing the drill cuttings up, to improve the efficiency of the drilling.

4. Conclusion

The following conclusions could be inferred from the results of flow field simulation at the bottomhole to analyze the effects of steerable nozzles:

1) the relative deviation angle of the tilted and the main jet spray α_0 = 45 is the most appropriate angle to support the efficient cleaning of drill cuttings and preventing the formation of mud on PDC drill bit, as well as making favourable conditions for the manufacturing of the steerable nozzles.

2) With the same simulation conditions, when compared with conventional nozzles, the steerable nozzles with support from a tilted jet stream, enhances drill cuttings cleaning at the bottomhole, and reduce the coverage area of the turbulent flow area to accelerate the process of transporting drill cuttings to the surface and ultimately to improve the efficiency of drilling.

References

1. Dickey, Winton B. *Side port nozzle in a PDC bit Europe.* EP0959224A2.11.24. 1999.

2. Li Zhaomin, Shen Zhonghou. *Numerical simulation of turbulent axisymmetric impinging jet flowfields*. Journal of the University of Petroleum China. 1995; 19 (6): p. 42 - 45.

3. Li Zhaomin, Shen Zhonghou. *Numerical simulation of turbulent axisymmetric jet flowfields*. Journal of the University of Petroleum China. 1995; 19 (2): p. 48 - 51.

4. Liu Gang, Chen Tinggen, Guan Zhichuan. *Effect of nozzle inclination angle on cleaning force acting on PDC bit teeth*. Journal of the University of Petroleum China. 1996; 20 (4): p. 30 - 33.

5. Huang Zhiqiang, Zhou Yi, Li Qin, Liu Shaobin, Bu Yan, Yan bo. *Study on the effect of the nozzle of drag bits on bottom - hole Flow Field*. Oil Field Equipment. 2009; 38 (3): p. 17 - 19.

6. Guan Zhichuan, Zhou Guang Chen, Liu Ruiwen, Li Chunshan. *PDC bit inclined jet flow distribution characteristics*. Petroleum Drilling Techniques. 1996; 24 (3): p. 32 - 34.

7. Hou Cheng, Li Gensheng, Huang Zhongwei, Tian Shouceng, Shi Huaizhong. *Research on characteristics of bottomhole flow field of PDC bit with side nozzles*. Oil Drilling & Production Technology. 2010; 32 (2): p. 15 - 18.

8. Yang Li, Chen Kangmin. *Research on the influence of nozzles with different diameters on flow field of PDC bits*. Chinese Journal of Mechanical Engineering. 2005; 9 (41): p. 171 - 174.

Contributions of acid and metal sites to propane aromatisation over fresh Ga, H-ZSM-5 catalyst

Dmitry B. Lukyanov, Stan T. Kolaczkowski
University of Bath, Department of Chemical Engineering
Nguyen Huu Luong
Vietnam Petroleum Institute

Abstract

A kinetic modelling has been developed to describe the aromatisation of propane over fresh H-ZSM-5 and Ga, H-ZSM-5 catalysts at 500°C. It was shown that the introduction of metal into H-ZSM-5 has enhanced both the yield and selectivity of aromatics and that the conversion of propane is mainly due to the dehydrogenation step over metal sites. Over Ga, H-ZSM-5 catalyst, the contribution of hydrogen transfer steps (between the feed alkane and alkenes adsorbed over acid sites) to the conversion of alkane is reduced considerably. On the other hand, the formation of aromatics is mainly from aromatisation steps over metal sites. As a result of the alkane dehydrogenation and alkene aromatisation steps over metal sites, the hydrogen yield is observed to increase in comparison with the hydrogen yield for the transformation over H-ZSM-5.

1. Introduction

The conversion of light alkanes into aromatic hydrocarbons is an important reaction from both the academic and industrial points of view. The medium pore zeolite ZSM-5 appears to be the most effective for this reaction [1]. The introduction of metal species, such as platinum, gallium or zinc, into H-ZSM-5 results in a remarkable enhancement of the catalyst aromatisation activity, but also leads to a pronounced increase in the rate of coke formation and related catalyst deactivation [2]. The enhancement of aromatisation activity on Me, H-ZSM-5 catalyst was attributed to the appearance of active metal sites as Lewis sites after the introduction of metal species into the zeolite [3, 4].

In agreement with the literature data [2, 5], the aromatisation of light alkane over ZSM-5 catalysts can be represented as a two-stage process: (i) transformation of light alkanes into light alkenes, and (ii) aromatisation of light alkenes. Over H-ZSM-5 catalysts, the first stage includes two routes: protolytic cracking route and hydrogen transfer route while the second stage proceeds through a number of acid-catalysed oligomerisation, cracking, cyclisation, and hydrogen transfer (HT) steps [5]. Over Me, H-ZSM-5 catalysts, metal species provide additional dehydrogenation routes for propane transformation into propene, and for alkenes transformation into aromatics [2, 5]. During the reaction, coke is also formed from reactive alkenes, covering active sites of the catalyst, and leading to catalyst deactivation [5, 8]. The entire pathway of the aromatisation reaction of light alkanes over H-ZSM-5 and

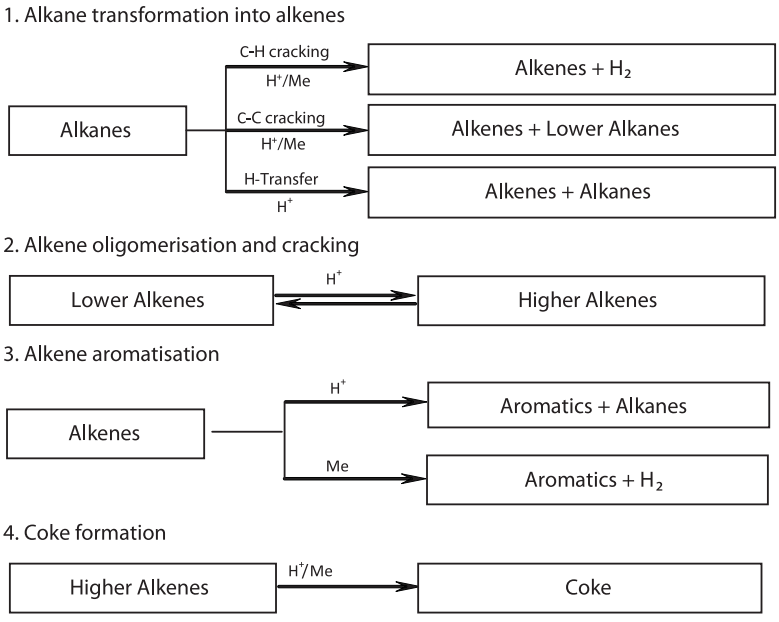

Fig. 1. *Reaction scheme of alkane aromatisation over Me, H-ZSM-5 catalysts*

Me, H-ZSM-5 catalysts is shown in Fig. 1. It is interesting to determine quantitative contributions of acid and metal sites to the reaction. In this work, we consider an approach to the development of a kinetic model that describes major features of the propane aromatisation over fresh H-ZSM-5 and Ga, H-H-ZSM-5 catalysts.

2. Experimental

H-ZSM-5 zeolite (Si/Al = 15) was used as a catalyst in this work. 1% Ga, H-ZSM-5 catalyst was prepared by impregnation of H-ZSM-5 zeolite with gallium nitrate solution using the incipient impregnation technique. Kinetic studies of propane reaction were performed at 500°C. The reactions were carried out under nondeactivating conditions at atmospheric pressure in a continuous flow micro-reactor with a feed of 80wt% of propane (N_2 was used as a gas carrier and diluting agent). Prior to the catalytic experiments, the catalyst samples were activated under N_2 flow (30ml/min) at 500°C for 4h. Reaction products were analysed by on-line GC equipped with two detectors: TCD (analysis of H_2) and FID (analysis of hydrocarbons). Different levels of conversions were obtained by performing experiments at different weight hour space velocities (WHSV) which have been checked for satisfaction of the reaction occurring in a kinetic regime. In our investigated conditions, at a certain space velocity, changes in flow rate and catalyst amount do not have any considerable effect on our experimental results. Hence, mass transfer limitation can be ignored.

3. Results and Discussion

3.1. Formulation of the model for the aromatisation of propane over fresh Ga, H-ZSM-5 catalysts.

The kinetic modelling to describe the reaction over a bifunctional catalyst (e.g. Ga, H-ZSM-5) is performed over two stages: (1) Development of a model for the reaction over H-ZSM-5 and (2) Modification of the model to apply for the reaction over Ga, H-ZSM-5. A model to describe the reaction of propane over H-ZSM-5 was developed and reported in our previous paper [6]. To apply the model for describing the reaction over a bifunctional catalyst, the reaction steps over metal sites and their corresponding rate constants and adsorption constants have been included into the model. According to a study by Turner [7], after introducing gallium species into H-ZSM-5, the number of Brönsted acid sites in a zeolite reduces by 60%. Therefore, over the bifunctional catalyst, the values of rate constants for reaction steps over acid sites, which have been obtained from the estimation over H-ZSM-5 catalyst, are multiplied by a factor of 0.4. Estimation of these values of rate constants is based on the comparison between the modelling results and experimental data on propane aromatisation over Ga, H-ZSM-5 catalyst at 500°C. A detailed procedure of the estimation for rate constants of the reaction steps over fresh H-ZSM-5 has been presented in our previous papers [6]. Hence, in this paper, only modelling results for the reaction steps over metal sites are reported (Table 1).

Table 1. *Relative values of rate constants for some reaction steps over metal sites in propane aromatisation over Ga, H-ZSM-5*

Reaction steps	Rate constants
$C_3 \rightarrow C_3^= + H_2$	1.0
$C_3^= + H_2 \rightarrow C_3$	12.7
$C_3 \rightarrow C_2^= + C_1$	0.21
$C_{6+}^= \rightarrow$ A (aromatics) + $2H_2$	64.0

From Table 1, the modelling results show that over metal sites, propane conversion by dehydrogenation is 4.8 times (1/0.21) higher than by cracking. Moreover, over metal sites, while propane dehydrogenation is reversible, C-C cracking of propane is irreversible. Therefore, it can be concluded that transformation of propane over metal sites is mainly from the route of dehydrogenation. It is shown that the rate of the reverse reaction of propane dehydrogenation (i.e., propene hydrogenation) is 12.7 times higher than that of propane dehydrogenation. Furthermore, it can be seen that over metal sites, the rate of $C_{6+}^=$ aromatisation (and also $C_{6+}^=$ dehydrogenation) is 64 times higher than that of dehydrogenation of propane.

In comparison with the reaction over H-ZSM-5, it can be seen that over Ga, H-ZSM-5, propane is converted 3 times faster than over H-ZSM-5 (Table 2). This result is comparable with the result reported by Lukyanov et al. (3.3 times) [5]. It is worth noting that the ratio between the rates of C-C cracking and C-H cracking decreases from 3 for H-ZSM-5 down to 0.3 for Ga, H-ZSM-5. Obviously, the dehydrogenation (or C-H cracking) becomes more favourable over Ga, H-ZSM-5 due to the contribution of metal sites to the mechanism for propane transformation.

Table 2. *Rate constants (mol g^{-1} atm^{-1} h^{-1}) for propane dehydrogenation and cracking steps over acid and metal sites for propane conversion over H-ZSM-5 and Ga, H-ZSM-5 catalysts at 500°C*

Reaction steps	H-ZSM-5	Ga, H-ZSM-5	
	H^+	H^+	Ga
$C_3 \rightarrow C_3^= + H_2$	0.013	0.0052	0.110
$C_3 \rightarrow C_2^= + C_1$	0.039	0.0156	0.023

3.2. Application of the model to describe the propane aromatisation over H-ZSM-5 and Ga, H-ZSM-5 catalysts at 500°C

The agreement between modelling results and experimental data is shown in Fig. 2 for the conversions of propane over H-ZSM-5 and Ga, H-ZSM-5 at 500°C. It can be seen that the model describes the experimental data properly. As expected, the conversion of propane increases with contact time. Fig. 2 shows that the conversions of propane over H-ZSM-5 and Ga, H-ZSM-5 catalysts are similar. It is worth to note that while the model describes propane transformation over H-ZSM-5 catalyst very well, its description over Ga, H-ZSM-5 shows an excess of alkane formation in comparison with experimental data (Fig. 3). However, main characteristics of the reaction are still reflected and description of main products (i.e., aromatics) is reasonable.

In other words, the introduction of gallium species into H-ZSM-5 has not changed the conversion of propane

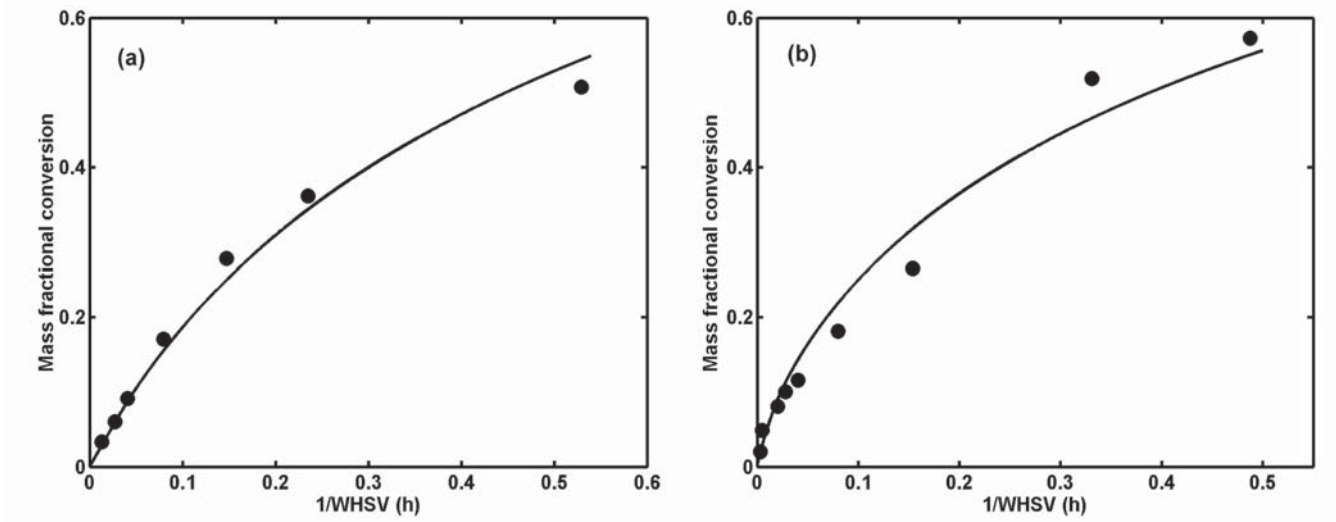

Fig. 2. *Propane aromatisation over fresh (a) H-ZSM-5 and (b) Ga, H-ZSM-5 at 500°C. Experimental data (points) and calculated curves for the conversion as a function of 1/WHSV*

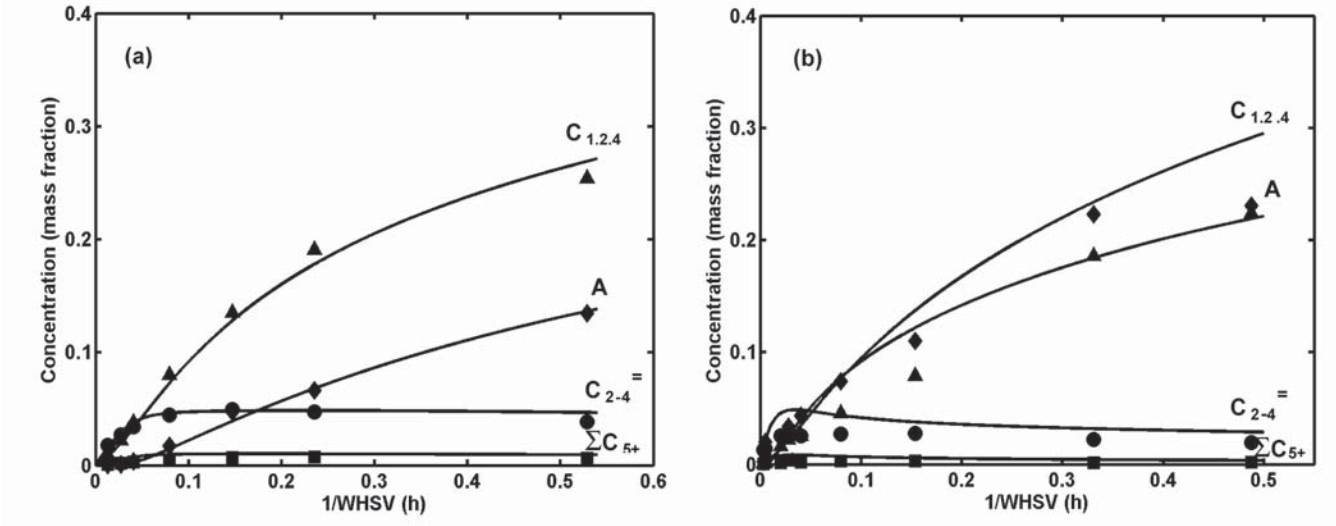

Fig. 3. *Propane aromatisation over fresh (a) H-ZSM-5 and (b) Ga, H-ZSM-5 at 500°C. Experimental data (points) and calculated curves for the concentrations of $C_{1,2,4}$ alkanes, $C_2^=$-$C_4^=$ alkenes, C_{5+} aliphatic hydrocarbons and aromatics as functions of 1/WHSV*

considerably. However, distribution of products in the reaction mixture is different due to the modification of the reaction pathway by the participation of reaction steps over metal sites into the transformation of propane into aromatics. Compared to the reaction over H-ZSM-5, over Ga, H-ZSM-5, a higher concentration of aromatics and lower concentrations of alkenes are observed as a result of a higher consumption of alkenes in aromatisation steps (Fig. 3). Effects of metal introduction on the reaction are discussed in the next section.

3.3. Effects of the introduction of metal species into catalyst on the reaction

3.3.1. The contribution of hydrogen transfer steps to conversion of propane

As discussed in our previous papers [6, 9], as the alkane conversion increases, the contribution of hydrogen transfer (HT) steps to the alkane transformation becomes significant and should be taken into account in the model for the reaction over H-ZSM-5. Modelling results in this work show that when mass fractional conversion of the alkane is around 0.50, this contribution is approximately 20% for propane aromatisation (Fig. 4). This result is in agreement with the result reported by Lukyanov et al. for propane aromatisation over H-ZSM-5 [5].

However, over Ga, H-ZSM-5, the contribution of hydrogen transfer steps between propane and alkenes adsorbed over acid sites is reduced considerably in comparison with over H-ZSM-5 (Fig. 5). Obviously, this reduction results from the addition of alkane conversion over metal sites and also from the decrease in the number of acid sites available for this reaction. In practice, at a propane mass fractional conversion of around 0.50, the contribution of these hydrogen transfer steps to the conversion of propane is only 2.8%. Therefore, it can be concluded that over Ga, H-ZSM-5, the conversion of propane mainly occurs by cracking and dehydrogenation steps over acid and metal sites.

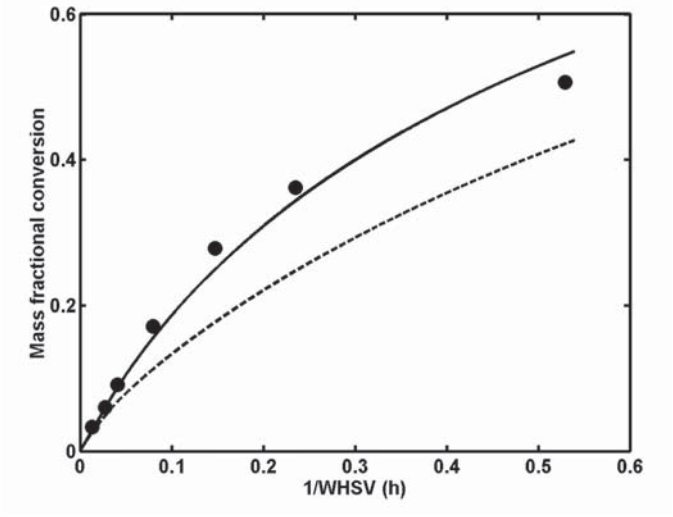

Fig. 4. *Propane aromatisation over fresh H-ZSM-5 at 500°C. Experimental data (points) and calculated curves (solid curve for the reaction over real catalyst with HT activity and dash curve for the reaction over pseudo-catalyst without HT activity) for propane conversion as a function of 1/WHSV*

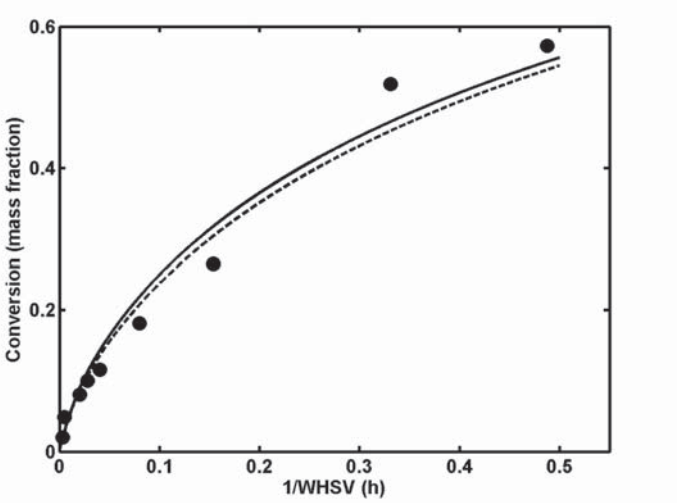

Fig. 5. *Propane aromatisation over fresh Ga, H-ZSM-5 at 500°C. Experimental data (points) and calculated curves (solid curve for the reaction over real catalyst with HT activity and dash curve for the reaction over pseudo-catalyst without HT activity) for propane conversion as a function of 1/WHSV*

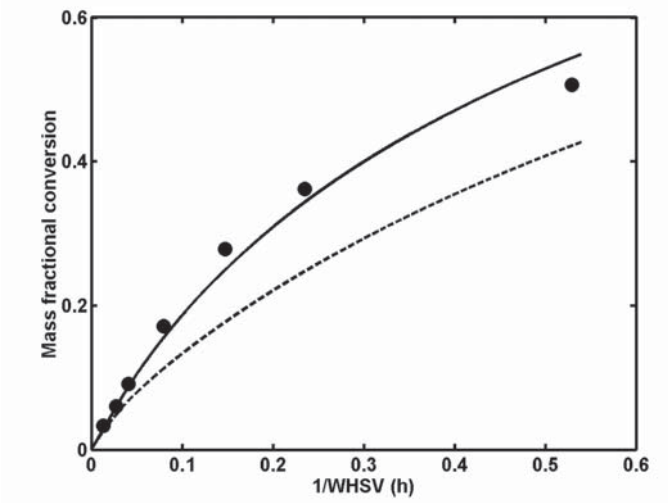

Fig. 6. *Propane aromatisation over fresh Ga, H-ZSM-5 at 500°C. Experimental data (points) and calculated curves (solid curve for the reaction over real catalyst with cracking activity over acid sites and dash curve for the reaction over pseudo catalyst without cracking activity over acid sites) for propane conversion as a function of WHSV-1*

3.3.2. The contribution of cracking steps over acid sites to propane conversion

In order to investigate the contributions of the cracking steps over acid sites of Ga, H-ZSM-5, a model without cracking steps over acid sites was constructed. On the basis of comparison of modeling results between the models over a real catalyst and over a pseudo-catalyst (without cracking activity over acid sites), it was shown that when the mass fractional conversion of propane is about 0.50, cracking steps over acid sites contribute approximately 7% to the conversion of propane over Ga, H-ZSM-5 (Fig. 6). Therefore, it can be concluded that over Ga, H-ZSM-5, propane activation is mainly catalysed by metal sites. This conclusion is also in agreement with the results reported by Lukyanov et al. for propane aromatisation over Ga, H-ZSM-5 [5].

3.3.3. Aromatisation steps over acid and metal sites

In comparison with propane transformation over H-ZSM-5, the introduction of metal into H-ZSM-5 has enhanced both the yield and selectivity of aromatics (Table 3). It can be seen from Table 3 that an enhancement of the aromatics yield is accompanied with a decrease in the alkane yield and an increase in the hydrogen yield. Therefore, it can be concluded that this enhancement arises from the dehydrogenation steps over metal sites, and not from the aromatisation steps over acid sites.

As a result of alkane dehydrogenation and alkene aromatisation steps over metal sites, the hydrogen yield is observed to increase in comparison with that obtained over H-ZSM-5 catalyst (Table 3). In addition, concentrations of alkenes, especially C_{6+} = alkenes, decrease sharply due to their intense consumption in the aromatisation steps (Fig.7).

It is also interesting to know the contribution of aromatisation steps over acid sites and over metal sites to the formation of aromatics over Ga, H-ZSM-5. Accordingly, a model without aromatisation steps over acid sites was constructed. On the basis of the comparison of the results obtained from the models with and without aromatisation activity over acid sites, it has been shown that at an alkane fractional conversion of around 0.50, these steps contribute less than 0.3% to the formation of aromatics over Ga, H-ZSM-5. In fact, this contribution can be neglected (Fig. 8). Hence, it can be concluded that over Ga, H-ZSM-5 catalyst, the formation of aromatics is mainly from the aromatisation steps over metal sites.

Table 3. *Calculated yield and selectivity of aromatics, yields of alkanes, alkenes, and hydrogen for propane conversion over H-ZSM-5 and Ga, H-ZSM-5 catalysts at 500°C and a mass fractional conversion of 0.30*

	H-ZSM-5	Ga,H-ZSM-5
Alkane yield	0.5200	0.4237
Alkene yield	0.1892	0.1437
Hydrogen yield	0.0092	0.0332
Aromatics yield	0.1831	0.3803
Aromatics selectivity	0.2119	0.4412

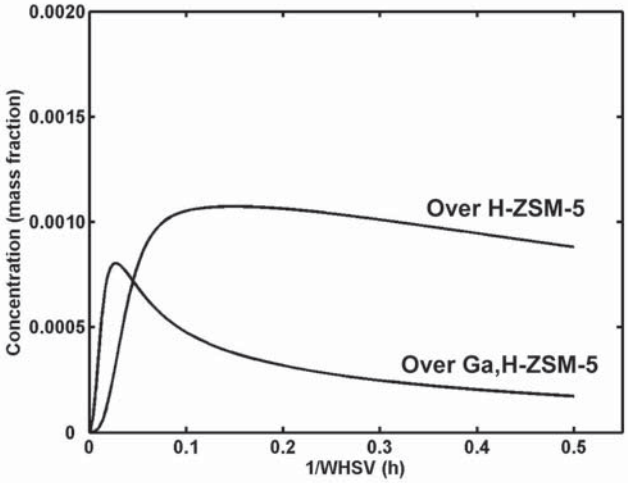

Fig. 7. *Propane aromatisation over fresh H-ZSM-5 and Ga, H-ZSM-5 at 500°C. Calculated curves for C_{6+} = concentration as a function of $WHSV^{-1}$*

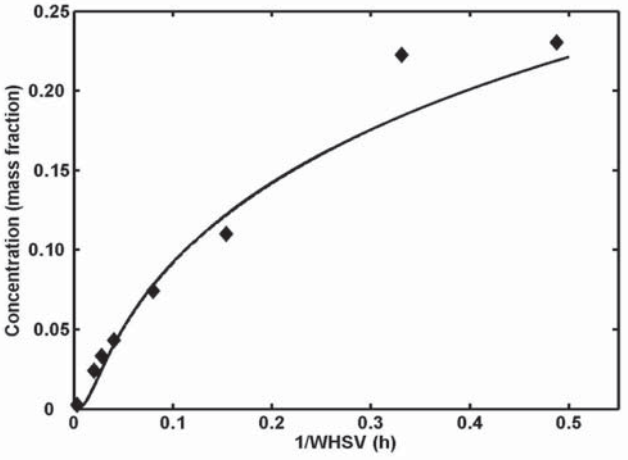

Fig. 8. *Propane aromatisation over fresh Ga, H-ZSM-5 at 500°C. Experimental data (points) and calculated curves (solid curve for the reaction over the real catalyst with aromatisation activity over acid sites and dash curve for the reaction over the pseudo-catalyst without aromatisation activity over acid sites) for the aromatics concentrations as a function of $WHSV^{-1}$*

4. Conclusions

The kinetic model developed in this work describes major features of propane aromatisation over fresh H-ZSM-5 and Ga, H-ZSM-5 catalysts at 500^0C properly. On the basis of the kinetic modelling results, it could be concluded that:

- Over Ga, H-ZSM-5, besides reaction steps over acid sites, additional steps over metal sites also contribute to the conversion of alkane and the formation of aromatics significantly. In comparison with the transformation performed over H-ZSM-5, the introduction of metal into H-ZSM-5 has enhanced both the yield and selectivity of aromatics. In addition, a decrease in the concentrations of alkenes due to their consumption in the aromatisation is also observed, and this decrease is more pronounced for the transformation of propane over Ga, H-ZSM-5 than over H-ZSM-5.

- Under the reaction conditions investigated, the rate of propane dehydrogenation over metal sites is 12.7 times slower than that of propene hydrogenation. On the other hand, the rate of propane cracking over metal sites is lower in comparison with propane dehydrogenation. Therefore, the transformation of propane over metal sites is mainly via the route of dehydrogenation.

- Over Ga, H-ZSM-5, the contribution of hydrogen transfer steps (between the feed alkane and alkenes adsorbed over acid sites) to the conversion of alkane is reduced considerably in comparison with that over H-ZSM-5. In fact, the conversion of propane is mainly due to the dehydrogenation step over metal sites.

- As a result of the alkane dehydrogenation and alkene aromatisation steps over metal sites, the hydrogen yield is observed to increase in comparison with that over H-ZSM-5. Over Ga, H-ZSM-5 catalyst, the formation of aromatics is mainly from the aromatisation steps over metal sites.

References

1. Fricke, R., Kosslick, H., Lischke, G., and Richter, M. *Incorporation of gallium into zeolites: Syntheses, properties and catalytic application*. Chem. Revs. 2000; 100: p. 2303 - 2405.

2. Kwak, B. S., Sachtler, W. M. H. and Hagg, W. O. Catalytic conversion of propane to aromatics: Effects of adding Ga and/or to HZSM-5. J. Catal. 1994; 149: p. 465 - 473.

3. Biscardi, J. A., and Iglesia, E. *Reaction pathways and rate-determining steps in reactions of alkanes on HZSM-5 and Zn/HZSM-5 catalysts*. J. Catal. 1999; 182: p. 117 - 128.

4. El-Malki, El-M., van Santen, R. A. and Sachtler, W. M. H., 1999. *Introduction of Zn, Ga, and Fe into HZSM-5 cavities by sublimation: Identification of acid sites*. J. Phys. Chem. B 103, p. 4611 - 4622.

5. Lukyanov, D. B. *Development of kinetic models for reactions of light hydrocarbons over ZSM-5 catalysts. experimental studies and kinetic modelling of ethene transformation and deactivation of HZSM-5 catalyst, in: Froment, G. F., and Waugh, K. C. (Eds.)*. Reaction kinetics and the development of catalytic process, Stud. Surf. Sci. Catal. 1999; 122: p. 299 - 306.

6. Nguyen, L. H., Vazhnova, T., Kolaczkowski, S. T., and Lukyanov, D. B. *Combined experimental and kinetic modelling studies of the pathways of propane and n-Butane aromatization over H-ZSM-5 catalyst.* Chemical engineering science. 2006; 61: p. 5881 - 5894.

7. Turner, J. *CE30062 Research project report, department of chemical engineering*. University of Bath 2003.

8. Berger, R. J., Stitt, E. H., Marin, G. B., Kapteijn, F., and Moulijn, J. A. *Chemical reaction kinetics in practice.* 2001; cattech 5 (1): p. 30 - 60.

9. Nguyen Huu Luong and Dmitry B. Lukyanov. *Development of a kinetic model for the aromatisation of propane and propene over H-ZSM-5 catalyst under deactivating conditions*. Petrovietnam Journal. 2011; Vol. 6: p. 74 - 78.

Synthesis of some dibenzothiophene-derived sulfur compounds

Bui Thi Le Thuy
Hanoi University of Mining and Geology

Abstract

Some dibenzothiophene deriving sulphur compounds were successful synthesized at laboratory scale by multistep methods. The yield of products decreased after every synthetic step, therefore, the procedures should be strictly followed, especially the refining steps. The products were analysed by GC-MS and the melting points were measured. Results showed that all final products have high purity (98 - 100%).

1. Introduction

Sulfur compounds in petroleum lead to equipment corrosion and SOx emissions that cause air pollution and acid rain. In recent years, regulations on sulfur limits of fuel are increasingly strict [1]. Therefore, extensive research has been carried out during the past decades in industrial and academic research laboratories to deeply desulfurize fuels [2, 3]. In laboratory investigations of desulfurization in petroleum, sulfur compounds are mixed in model oil at specific concentrations and then removed [4, 5].

However, many complex dibenzothiophene-derived sulphur compounds are rarely available to purchase. Therefore, this present work investigates the synthesis of some complex sulfur compounds (Table 1).

2. Experimental procedure and Results

2.1. Synthesis of 8, 9, 10, 11- tetrahydro benzo[b] naphtho[2, 1-d]thiophene

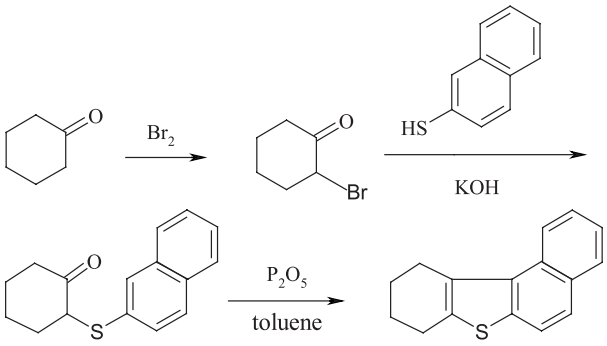

Scheme. 1. *Synthesis of 8, 9, 10, 11- tetrahydro benzo[b] naphtho[2, 1-d]thiophene [6, 7]*

Table 1. *Sulfur compounds synthesized in this work*

N_o	Compound	Molecular formula	Molecular weight	wt % S
1	8, 9, 10, 11- tetrahydro benzo[b]naphtho[2, 1-d]thiophene	$C_{16}H_{10}S$	234	13.67
2	7, 8, 9, 10- tetrahydro benzo[b]naphtho[1, 2-d]thiophene	$C_{16}H_{10}S$	234	13.44
3	4-Keto-1, 2, 3, 4-tetrahydro benzo[b]naphtho[2, 3-d]thiophene	$C_{16}H_9SO$	252	12.69
4	4, 6-dimethylbibenzothiophene (4, 6-DMDBT)	$C_{14}H_{12}S$	212	15.09
5	2, 4, 6, 8-tetramethyldibenzothiophene (2, 4, 6, 8-teMDBT)	$C_{16}H_{16}S$	240	13.33

2.1.1. 2-Bromocyclohexanone

24.5g (250mmol) of cyclohexanone was mixed with 150ml of methanol and cooled to -10°C. 40.g (250mmol), bromine was added quickly to the vigorously stirred solution. There was no noticeable exothermic effect. After 30 minutes, the temperature was raised to 0°C. Stirring was continued for 8 hours during which the reaction mixture went up to room temperature. The solution became colourless. The reaction was quenched with 75ml of water. The mixture was stirred overnight at room temperature. An additional 75ml of water was added and the two-phase mixture was concentrated under reduced pressure to remove methanol. The remaining mixture was extracted with 2 * 100ml portions of 1:1 v/v ethyl acetate: hexane. The combined extracts were washed with 70ml of water, 30ml of 1.2M sodium bicarbonate and 75ml of saturated brine and were then dried over anhydrous sodium sulfate. The dry extract was concentrated under reduced pressure and the residue was distilled under vacuum (52°C at 0,1mm) to yield 22g of a colorless liquid (yield = 49.7%). The product should be stored at -10°C under argon.

2.2.1. 2- (ß-naphthylmercapto) cyclohexanone

10.6g 2-bromocyclohexanone (60mmol) was gradually added to an ice-cooled (20°C) solution of ß-thionaphthol (9.4g or 58.75mmol) in 35% aqueous sodium hydroxide (68ml) during 10 minutes under vigorous stirring. After stirring for 1.5 hours, the mixture was diluted with water and extracted with ether. The extract was washed with alkali, water and dried. Removal of ether gave 8g of a dark colour liquid (yield = 54%).

Note: ether was added gradually until no more solid appeared.

2.2.3. 8, 9, 10, 11-tetrahydro-benzo[b]naphtho[1, 2-d] thiophene

The mixture of 8g (ß-naphthylmercapto) cyclohexanone and 24g phosphrous pentoxide was boiled in 160ml of toluene for 1.5 hours. Removal of toluene gave yellow-coloured oil. Recrystallization from alcohol gave 3.2g lustrous needles with melting point of 81°C, purity of 98%, and yield of 43%.

2.2. Synthesis of 7, 8, 9, 10- tetrahydro benzo[b] naphtho[1, 2-d]thiophene

2.2.1. 2 (ß -naphthylmercapto)cyclohexanone

A mixture of ß-thionaphthol (9.2g or 57.5mmol), sodium (1.4g), absolute alcohol (5ml) and 2-bromocyclohexanone (12g or 67.8mmol) was refluxed for 7 hours. The product was extracted with ether. Removal of ether gave 6.5g brown oil (yield = 44.8%).

2.2.2. 7, 8, 9, 10-tetrahydro-benzo[b]naphtho[1, 2-d]thiophene

The mixture of 5g (ß-naphthylmercapto)cyclohexanone and 15g phosphorous pentoxide was boiled in 100ml of toluene for 2 hours. Removal of benzene gave yellow

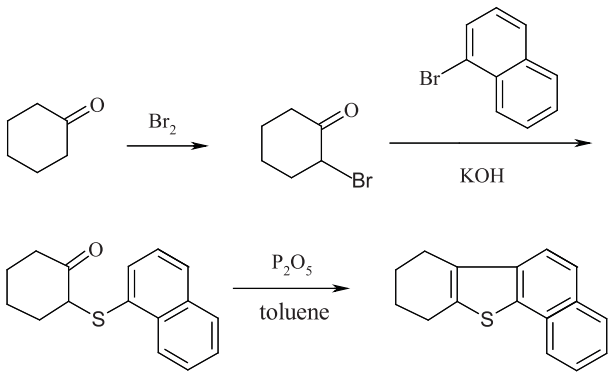

***Scheme. 2**. Synthesis of 7, 8, 9, 10- tetrahydro benzo[b]naphtho[1, 2-d] thiophene [6, 7]*

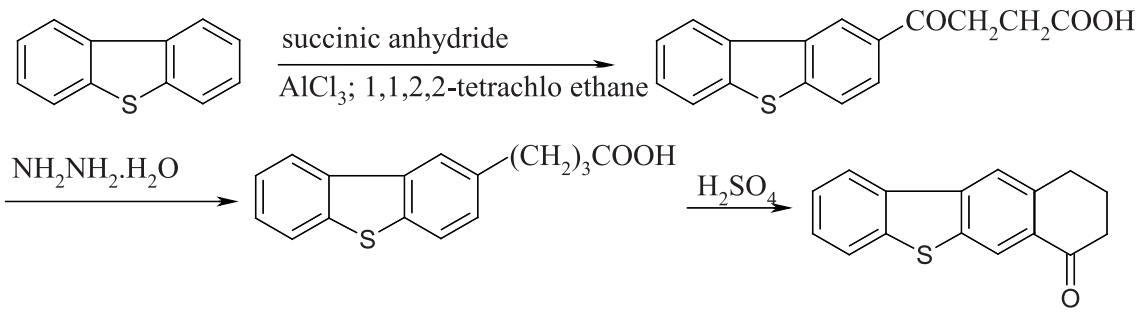

***Scheme. 3**. Synthesis of 4-Keto-1, 2, 3, 4-tetrahydro benzo[b]naphtho[2,3-d]thiophene [8, 9]*

coloured oil. Recrystallization from alcohol gave 1.5g of lustrous needles (melting point 96.5°C, purity = 98.6%, yield = 32%).

2.3. 4-Keto-1, 2, 3, 4-tetrahydro benzo[b]naphtho[2, 3-d]thiophene

2.3.1. ß-2-Dibenzotheonylpropionic acid

46g (250mmol) of dibenzothiophene, 27.5g (275mmol) of succinic anhydride was dissolved in a mixture of 200ml of 1, 1, 2, 2-tetracloroethane and 100ml of nitrobenzene. 77.5g of aluminium chloride was added in 30 minutes at 0 - 5°C. After stirring for 5 hours at 20°C the reaction mixture was poured in a mixture of ice and hydrochloric acid. Recrystallization from ethyl acetate gives 18g of product with melting point of 157°C and yield of 25%.

2.3.2. γ-2-Dibenzothienylbutyric acid

10g (35mmol) of ß-2-dibenzotheonylpropionic acid, 5g of sodium hydroxide, 80ml of 85% hydrazine hydrate were refluxed for 1 hour. Water was then distilled slowly from the reaction mixture until the temperature of the boiling solution reached 195 - 200°C. The mixture was boiled for 3 hours then cooled by the addition of ice. Dilute hydrochloric acid was added slowly with stirring until the solution was acid to litmus. The precipitated product was collected, washed with water, and recrystallized from 80% methanol solution to obtain 4g of product melting at 123°C (yield = 42%).

2.3.3. 4-Keto-1,2,3,4-tetrahydro benzo[b]naphtho[2,3-d] thiophene

4g (148mmol) of ß-2-dibenzotheonylpropionic acid was stirred with 100ml 98% sulfuric acid for 15 minutes at room temperature. The solution became deep red and was poured in ice. The precipitate was filtered, washed with dilute sodium hydroxide, dried and recrystallized from ethanol to give 0.5g of final product (melting point 175°C, yield = 13%, purity = 98%).

2.4. Synthesis of 4,6-Dimetyl dibenzothiophene

200ml of a 1.6M solution of n-butyllithium in hexane (320mmol) were added drop-wise at 0°C to a solution of TMEDA (320mmol or 37.2g) in 100 ml of dry cyclohexane. After being stirred for 30 minutes at 0°C and 30 minutes at room temperature, the mixture was diluted with 200ml of hexane. Then, 19.6g (106.5mmol) of dibenzothiophene were added. After 2 hours being heated at 60°C, the reaction mixture was cooled at -78 °C and 45.5g of methyl iodide (320mmol) was added in 10 minutes. After completion, the mixture was left for 12 hours at room temperature. It was then poured into a flask containing 1 l of ice-water. The product was extracted with methylene chloride (3 * 250ml). The organic phase was acidified with HCl 1N (300ml) and washed with water (3 * 300ml) and dried over magnesium sulphate. Solvent was removed under vacuum. 4.5g 4, 6-DMDBT (melting at 153 - 157°C) were obtained after recrystallizing from tetrahydrofurane (yield = 22%). Analysis by GC-MS showed that the purity was 99.6%.

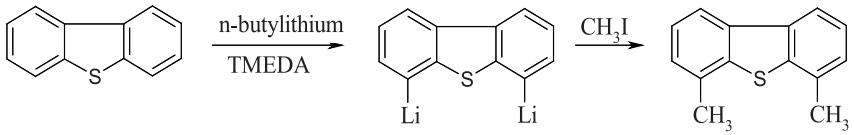

***Scheme. 4**. Synthesis of 4, 6-Dimetyl dibenzothiophene [10]*

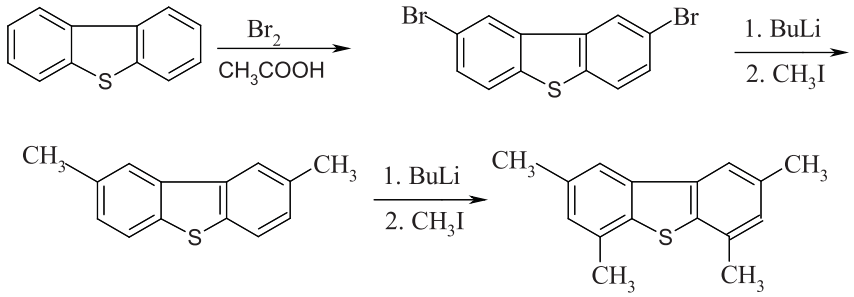

***Scheme. 5.** Synthesis of 2, 4, 6, 8 - tetramethyldibenzothiophene (2, 4, 6, 8-TMDBT) [10-12]*

2.5. Synthesis 2, 4, 6, 8-tetramethyldibenzothiophene (2, 4, 6, 8-TMDBT)

2.5.1. Synthesis 2, 8-dibromodibenzothiophene

35.2g (220mmol) of bromine in 100ml of glacial acetic acid were added to a suspension of 10g (54mmol) of dibenzothiophene in 400ml of acetic acid over a period of 30 min. After that, the mixture was stirred for two hours. It was then refluxed over night and cooled. The mixture obtained was yellow. The product was filtered, washed with water and dried.

Recrystallization from acetic anhydride yielded about 10g of material melting at 228 - 230°C (yield = 44.8%).

2.5.2. Synthesis 2, 8-dimethyldibenzothiophene (2, 8-DMDBT)

A solution of n-butyllithium (38.5mmol) in 24ml of hexane was added within 20 min to a stirred suspension of 2, 8-dibromodibenzothiophene (6.6g (19mmol) in 64ml of hexane) at 0°C. The mixture was further stirred for 30 min at 5°C then a yellow solution was obtained. Further stirring for 30 minutes at 18°C was accompanied by the formation of a colourless precipitate. The suspension was cooled at 0°C in an ice bath and methyl iodide (38.7mmol) was added drop-wise. Then the reaction mixture was stirred for 12 hours at room temperature. It was poured into a flask containing 0.32l of ice water. The product was extracted with methylene chloride (3 * 88ml) and solvent was removed under reduced pressure. The final product had a melting point of 119°C and weighed 1g, equivalent to a yield of 25%.

2.5.3. Synthesis of 2, 4, 6, 8-tetramethyldibenzothiophene

20ml of a 1.6M solution of n-butyl lithium in hexane were added drop-wise at 0°C to a solution of TMEDA (3.7g or 0.032mmol in 10ml of dry hexane) under an argon atmosphere. After stirring for 30 minutes at room temperature, the mixture was diluted with 20ml of hexane. Then 2.25g (10.6mmol) of 2, 8-DMDBT were added through a solid addition funnel. After 2 hours heating at 60°C, the reaction mixture was cooled at -78°C and 4.55g of methyl iodide were added gradually. The reaction must be controlled by vigorous agitation and cooling. After completion, the mixture was left for 12 hours at room temperature. It was then poured in to a flask containing 0.1l of ice water. The product was extracted with methylene chloride (3 * 25ml). The organic phase was acidified with HCl 1N (30ml) and washed with water (3 * 30ml), then dried over magnesium sulfate. Solvent was removed under reduced pressure. The product obtained was in colloidal form (1g). Analysis by GC-MS showed that the product contained DBT, 2-MDBT, 2, 8-DMDBT, 2, 6, 8-TMDBT and 2, 4, 6, 8-TMDBT.

3. Conclusion

In this work, all the sulphur compounds were synthesized by complex methods. Therefore, only moderate yields were obtained. However, the observed purity of all final products was from 98 - 100%. Most of these complex sulfur compounds are not available to purchase. After synthesising the compounds were mixed with model diesel and jet fuels for deep desulfurization research [13, 14].

References

1. J. Stell. *2001 worldwide refining survey*. Oil and Gas J. 2001; 99: p. 74.

2. P.Jeevanandam, K.J. Klabunde, and S.H.Tetzler. *Microprous and mesoporous materials.* 2005; 79: p. 101 - 110.

3. Toru Takatsuka, Shin -ichi Inoue, and Yukitaka Wada. *Catalysis today.* 1997; 39: p. 69 - 75.

4. Yi Nie, Chunxi, Hong Meng, and Zihao Wang. *Fuel processing technology.* 2008; 89, p. 978 - 983.

5. Luisa Alonso, Alberto Arce, Maria Francisco and Ana Soto. J. Chem. Thermodynamics. 2008; 40: p. 966 - 972.

6. John A. Easter and Wayne T. Stolle, J. Labelled compound radiopharmceuticals. 2001; 44: p. 797.

7. K. Rabindran and B.D. Tilak, Proc. Indian Acad. Sci. 1953; 37A: p. 564.

8. Henry Gilman and Arthur L. Jacoby, J. Org. Chem. 1938; 3 108.

9. E. Campaigne and S.W. Osborn, Heterocycles, 655-661 (1968).

10. Catherine Kuehm - Caubere, Sandrine Adach - Becker, Yves Fort and Caubere, Tetrahedron. 1996; 52(27): p. 9087 - 9092.

11. C.R. Neumoyer and E.D. Amstutz; J. Am. Chem. Soc. 1947; 69: p. 1920.

12. Gerdil and E.A.C. Lucken, J.Am. Chem. Soc. 1965; 87: p. 213.

13. Wieland Wache, Leonid Datsevich, Andreas Jess, Gerhard Neumann, Fuel. 2006; 85: p. 1483.

14. Jochen Esser. *Tiefentschwefelung von mineralölfraktionen durch extraktion mit ionischen Flüssigkeiten.* University of Bayreuth, dissertation. 2006.

In situ XANES studies of Titanium sites and their reactivities in nanoporous Titanosilicate frameworks

Nguyen Khanh Dieu Hong
Hanoi University of Science and Technology
Vo Duc Anh, Nguyen Thi Ha
Ho Chi Minh University of Industry
Richard A. Catlow
Department of Chemistry - University College London

Abstract

This study focused on the study of titanium sites, their local structure and reactivities in nanoporous titanosilicates frameworks by using in situ X-ray absorption spectroscopy. XANES provide the information on the oxidation state of the titanium species as well as their change in coordination geometry during de- and re-hydration. Results from in situ XANES studies shows that TS-1 is much more hydrophobic than TiAl or TiFe systems. Pre-edge features of Ti K-edge XANES spectra of these materials also suggested that Ti^{IV} is the dominant Ti coordination in dehydrated system whilst Ti^{VI} is the dominant in the re-hydrated one.

1. Introduction

Titanium-containing nanoporous materials attract much interest because of their remarkable catalytic properties in various oxidation reactions. Titanosilicate materials are shown to catalyze oxidation reactions in the presence of hydrogen peroxide H_2O_2 (as an oxidant) where only water is given off as the by-product. Therefore such materials act as catalysts in 'green' reaction systems. Some of the applications of these catalyst are for the epoxidation of cyclohexene to form epoxides [1, 2, 3]; the catalytic oxidation of propylene to propylene oxide [4].

TS-1, a member of the titanosilicate, family represented by the MFI structure-type has been investigated intensively because of its particularly high catalytic activity which likely derives from its high surface hydrophobicity. This feature means that the adsorption of the organic substrates are more favoured over more polar species such as water since the organic molecules are kept in the pores near Ti^{IV} sites.

During the 1980s, it was proposed that titanium in the TS-1 catalyst was present as titanyl groups or as the corresponding hydrated system [5]. Later, in 1993, this model was corrected using EXAFS measurements to interpret the nature of the titanium species [6]. It was reported that titanium sites are Ti^{IV} in the calcined framework. XANES/EXAFS spectroscopy has been used ever since in view of the fact that it gives direct proof of the coordination of titanium sites in a system [7].

Further studies on the Ti-containing catalyst using X-ray absorption, UV-VIS, IR spectroscopy and computational work [8, 9] yield evidence that Ti^{IV} resides in tetrahedral coordination in the calcined TS-1. Although this structural model for the active site is accepted, there are several issues constantly reported in the literature. For example, Sankar, Catlow and Thomas [10] reported that the titanium in tetrahedral coordination in TS-1, Ti-zeolite b and Ti-MCM-41 but the pre-edge intensity is not the same in all these catalysts. A possible explanation given for this difference may be related to the nature of distortion in the tetrahedral geometry which may affect the pre-edge intensities.

In 1996, F. Farges et al [11] suggested that pre-edge position and height of Ti K-edge XAFS spectra can be used to derive accurate information on the local coordination environment of Ti sites. Using these features, it is possible to distinguish between one coordination environment vs. a mixture of several others. In their work, Ti K-edge spectra were collected for several model compounds in which Ti is located in 4-, 5- or 6-coordinated sites: Ti^{IV}(as Y_2TiMo_8); Ti^{V}(as $K_2Ti_2O_5$) and Ti^{VI} (as $CaTiSiO_5$). Their study indicated that the use of both position and height of the pre-edge

is required to extract reliable Ti coordination numbers from pre-edge features in Ti-XANES spectra of examined materials.

This work presents the study of titanium sites and their reactivity in some nanoporous frameworks with MFI structure. In particular, *in situ* X-ray absorption spectroscopy, XAS, was employed to investigate the local structure around the active titanium sites during de- and re-hydration process. The intensity (height) and position of the pre-edge peak, which is related to the coordination geometry of titanium sites is extensively used in this study. Furthermore we highlight and compare local environments and reactivities of titanium sites in titanium-cogel precursors (used to prepare TS-1 catalysts), titanosilicate (TS-1) and multi-metallosilicate (MTS-1, where M=Fe or Al) hosts.

2. Experimental

2.1. Model compounds for XANES studies

In this work three model compounds for XAS measurement were used: ETS-10, Fresnoite ($Sr_2TiSi_2O_8$) and $Ti(OSiPh_3)_4$. The reason being, all these materials have identical first and second neighbour atoms similar to the one that is present in titanosilicates.

The structure of three model compounds and suggested models of coexisting titanium sites in the materials examined in this studies are co-plotted in Fig. 1 (a, b, c, d, e). The suggested models of titanium sites in examined titanosilicates will be confirmed in the results and dicussion. XANES spectra of three model compounds are also presented in Fig. 17.

ETS-10 is a large pore nanoporous zeotype material, consists of corner-sharing TiO_6 and SiO_4 linked together through bridging oxygen atoms (Fig. 1a) [8, 9]. The crystal structure of Fresnoite, $Sr_2TiSi_2O_8$ possesses an interesting peculiarity as it is one of the few instances of five-fold co-ordinated titanium located inside a square pyramid [12]. $Ti(OSiPh_3)_4$ is a four-coordinate, tetrahedral and monomeric compound in which Ti^{IV} sites are shrouded by the bulky triphenyl groups [13] (Fig. 1c).

XANES examinations reported in this paper were all recorded at station BM26, ESRF, Grenoble, France.

2.2. *In situ* XANES set up

Fig. 2 shows schematic representation of the calcination cell used to obtain XANES spectra of the de/re-hydrated materials examined.

In an typical experiment, a 100mg of the catalyst disc of 20mm diameter was mounted into the quartz sample holder. Materials were then heated to 400°C at 5°C/min in dry air. Following this, samples were then cooled to room temperature. During measuring the Ti K-edge XAS,

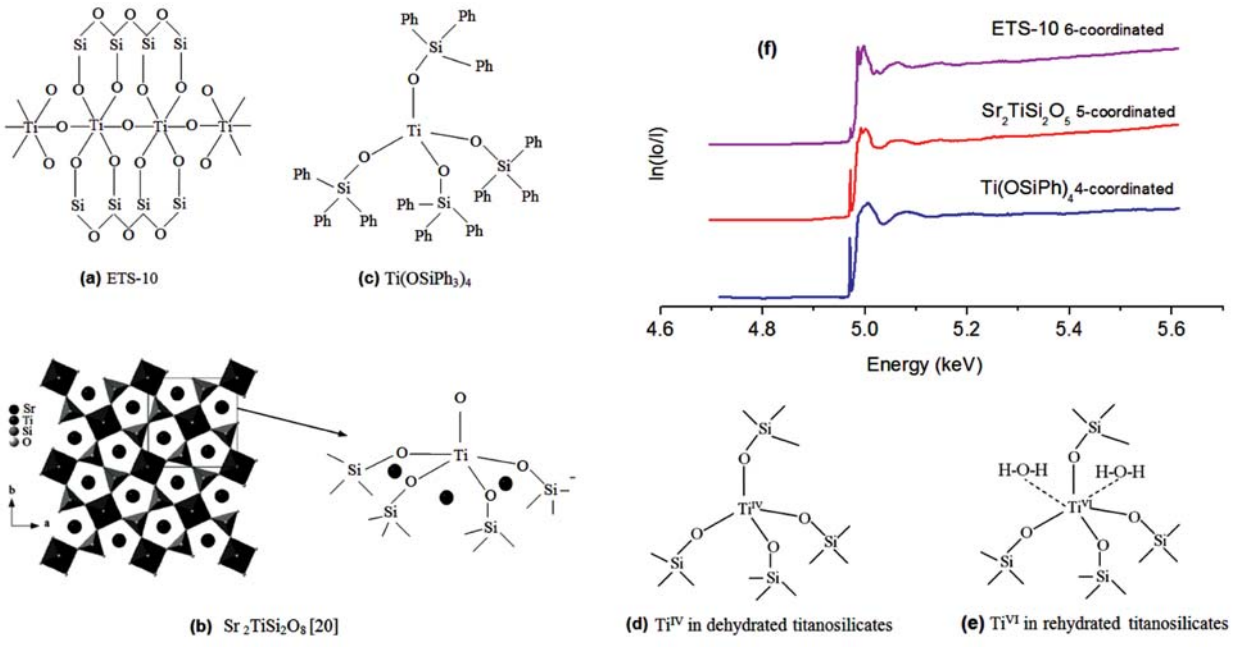

Fig. 1. *Structure of three model compounds containing Ti^{IV}, Ti^{V}, Ti^{VI} coordination and suggested models of titanium sites co-exist in the materials examined are co-plotted with XANES spectra*

water vapour was prior introduced into the cell through a bubbler for re-hydration studies, which will represent the reactivity during catalysis, since hydrogen perioxide typically used contains about 70 percent water.

X-ray diffraction measurements were collected on a Siemens D500 diffractometer at University College London.

2.3. Nanoporous titano silicate materials preparation

All titanosilicate and metallosilicate samples in this work were synthesized from the cogel precursors by Amber Welch and was reported in ref [2].

First, the cogel precursor was prepared. Tetraethylorthosilicate (TEOS) (98%, 49.8g, 0.2mol) was slowly added to a stirred solution of distilled water (20.0g, 1.1mol) and dilute hydrochloric acid (0.1M, 20.0g, 0.5mol) and the resultant solution stirred for 45 minutes. A separate solution of the heteroatom source* in isopropyl alcohol (110.0g, 1.8mol), was vigorously stirred for ~ 4 hours. The two solutions were then mixed and further agitated* whilst an aqueous solution of ammonium salt* was added drop wise until gelation occurred. The transparent white gel was then dried overnight ~ 80°C, calcined (if required) (3°C min^{-1} to 535°C, 4 hours maintained) crushed and the resultant white powder (~ 40.0g) stored under ambient conditions.

The SiO_2-TiO_2 cogels were prepared using the sol-gel process which gives control over both the properties and chemical composition of the raw material. In the TS-1 cogel, the titanium and silicon atoms are bound through oxygen bridges, stabilising the titanium atoms and preventing TiO_2 precipitation during the synthesis procedure [10, 11]. The prepared cogel precursor was converted into Ti-S1 by reacting with tetrapropylammonium hydroxide, under hydrothermal conditions.

Similarly, the multi-heteroatom cogels for the synthesis of multi-metallosilicate were prepared from two separate sources of heteroatoms. S1 was used as the suffix for framework materials additionally specific nomenclature was adopted that would make the nature of the heteroatoms easily explicable. MFI materials with incorporated titanium and aluminium/iron centres were named TiAl-S1 and TiFe-S1. For each system, we have also examined their cogel precursors.

3. Results and discussion

XRD pattern of all calcined cogels (cogels were calcined at the rate 3°C min^{-1} to 535°C, 4 hours maintained) and as-synthesized materials were shown in Fig. 3. As is clearly visible, the cogel appears amorphous with no long-range order. Conversely, the as-prepared Titanosilicate materials show a crystalline nature and adopt the framework type of MFI.

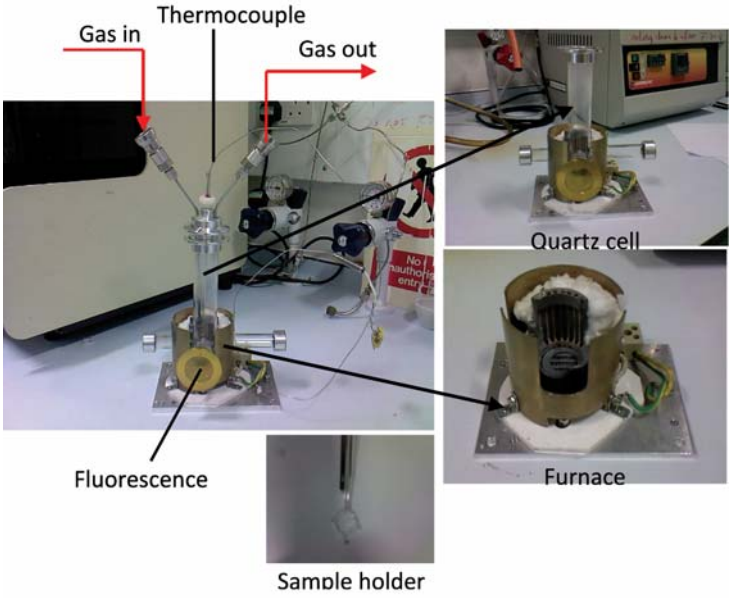

Fig. 2. *Schematic representation of the calcination cell used to obtain XANES spectra of the de/re-hydrated materials*

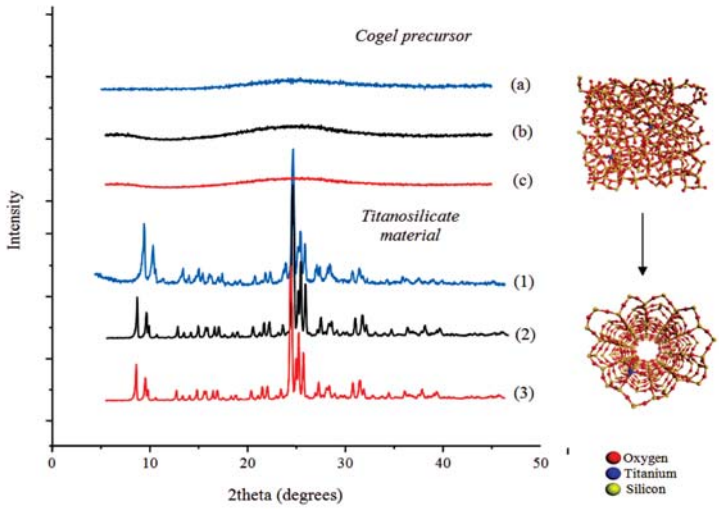

Fig. 3. *XRD pattern of all calcined cogels and as-synthesized Titanosilicate materials (1, a): TS-1 and TS-1 cogel; (2, b): TiAl-S1 and TiAl cogel; (3, c): TiFe-S1 and TiFe cogel*

3.1. XANES studies of model compounds

XANES features of model compounds are shown in Table 1.

The XANES spectrum of ETS-10, in which titanium is in octahedral coordination, has a pre-edge intensity of 0.19926 and position at 4.97208keV (4972.08eV). The XANES spectrum of $Sr_2TiSi_2O_8$ material, a model compound for Ti sites in pentahedral coordination, has a pre-edge at 4.7128keV with intensity of 0.56776. The $Ti(OSiPh_3)_4$ material, which is a model compound for Ti sites in tetrahedral coordination, has a pre-edge intensity of 0.87399. Its pre-edge position is at the lower energy of 4.97068keV (4970.68keV).

Direct correlation between the pre-edge position of a sample and its intensity can be established from Table 1: tetrahedrally coordinated systems have a higher pre-edge intensity, which appears at a lower energy than that of an octahedrally coordinated titanium site as we have confirmed in Fig. 1. Pentahedrally coordinated systems have a pre-edge intensity and location in between tetrahedrally and octahedrally coordinated systems.

3.2. Study of Ti sites in TS-1 system

3.2.1. XANES study of titanium-cogel

Pre-edge of Ti K-edge XANES of the Ti-cogel and TS-1 recorded during an *in situ* study are plotted in Fig. 4, in which: (A): up on the calcination up to 400°C, (B): upon the re-hydration, (C): complete plot of Pre-edge of Ti K edge XANES and (D): pre-edge intensity vs energy positions compared with the model compounds.

As seen in Fig. 4 (left), the intensity of pre-edge in XANES of Ti cogel increased upon increasing the temperature of de-hydration to 400°C (a) and decreased upon the re-hydration (b), suggesting a change in the local environment of the Ti sites in the system during these processes. As-prepared cogel has a pre-edge intensity of 0.3245 and its position appeared at 4.97094keV. After de-hydration to 400°C, the pre-edge shifted towards lower energy values, specifically, 4.97071keV, and its intensity reached 0.79145.

In the following step, the sample was then cooled down and water was introduced into the system. After re-hydration, the pre-edge intensity decreased to 0.26375 and the position of pre-edge peaks shifted back to a higher energy of 4.97154keV.

It is clear from Fig. 4D (left), all as-prepared/de-hydrated/re-hydrated samples have a lower pre-edge intensity compared with the model compound $Ti(OSiPh_3)_4$ and a higher pre-edge intensity compared with that of ETS-10. Pre-edge position of all samples are between $Ti(OSiPh_3)_4$ and ETS-10. From comparison with pre-edge feature of $Sr_2TiSi_2O_8$, it is inferred that the titanium centres of prepared cogel contains a mixture of tetrahedral and octahedral coordination rather than a pentahedral one. The pre-edge position is more similar to that for a tetrahedral system (with dehydrated material) and for octahedral system (with hydrated material) than for a pentahedral one. The pre-edge intensities of the re-hydrated Ti-cogel are much lower than that of the de-hydrated one. This suggests that water interacts with Ti^{IV} sites upon exposure to atmosphere. However the re-hydrated Ti-cogel does not generate the type of octahedral coordination seen for ETS-10.

3.2.2. XANES study of TS-1

As noted in the XANES study of the Ti-cogel, TS-1 shows a lower pre-edge intensity compared with the de-hydrated material, and the model compound, $Ti(OSiPh_3)_4$ (Fig. 5D right). This suggests that water interacts with Ti^{IV} centres upon exposure to the atmosphere. As-prepared TS-1 has a pre-edge intensity of 0.3481 and its position at 4.97094keV. After de-hydration to 400°C, the pre-edge shifted towards lower energy to the value of 4.97068keV, and its intensity reached 0.52323.

After cooling and re-hydration the pre-edge intensity decreased to 0.2342 and the position of the pre-edge peaks shifted back to a higher energy of 4.97134keV. This reactivity of pre-edge in XANES of TS-1 is found to be very similar to the reactivity of the pre-edge of the Ti-cogel precursor.

Although the pre-edge in XANES of the as-prepared TS-1 appeared at the same energy as the cogel precursor, their pre-edge intensity is different. The pre-edge intensity in XANES of the as-synthesized TS-1 (0.3481) is higher than that in the prepared co-gel (0.3245).

Table 1. *Ti K-edge XANES features of three model compounds*

Model compound	Pre-edge intensity	Pre-edge position, keV
Ti^{VI}-ETS-10	0.19926	4.97208
Ti^{V}-$Sr_2TiSi_2O_8$	0.56776	4.97128
Ti^{IV}-$Ti(OSiPh_3)_4$	0.87399	4.97068

Pre-edge features of TS-1 and Ti-cogel, compared with three model compounds, shows that both cogel precursor and as-synthesized materials contain a mixture of Ti^{IV} and Ti^{VI}. However, octahedral coordination generated by the interaction of water molecules with titanium centres does not generate the same octahedral coordination seen the in ETS-10 model compound.

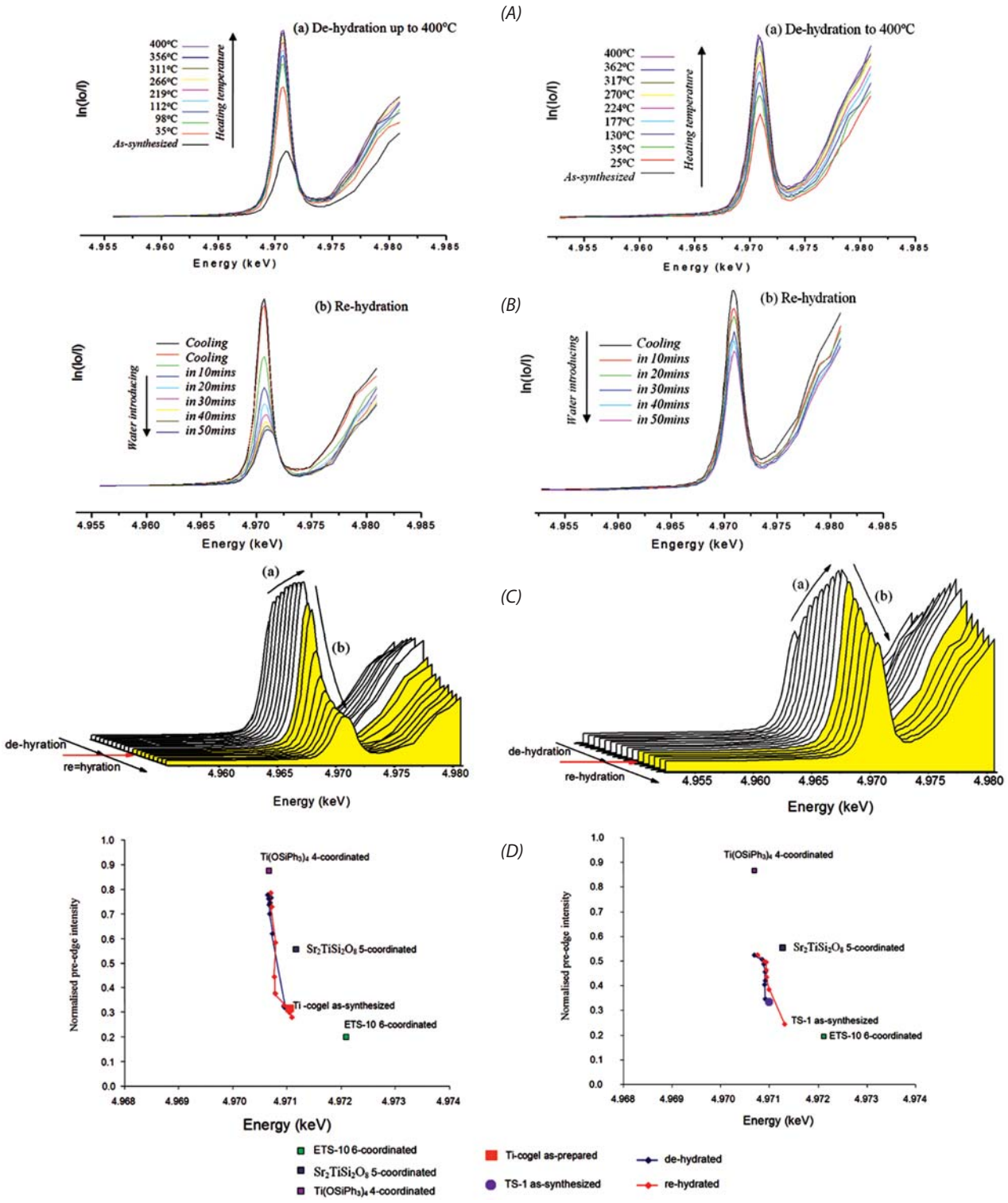

Fig. 4. *Pre-edge studies of Ti K-edge XANES of the Ti-cogel (left) and TS-1 (right) recorded during an in situ study upon the calcination and re-hydration*

Table 2. *Ti K-edge XANES features of TiAl-cogel and TiAl-S1*

Pre-edge features	TiAl-cogel sample			TiAl-S1 sample		
	Before dehydration (As-prepared)	At 400°C	After rehydration	Before dehydration (As-prepared)	At 400°C	After rehydration
Pre-edge intensity	0.23746	0.68765	0.21223	0.36777	0.65081	0.42178
Pre-edge position, keV	4.97134	4.97054	4.97134	4.97114	4.97054	4.97074

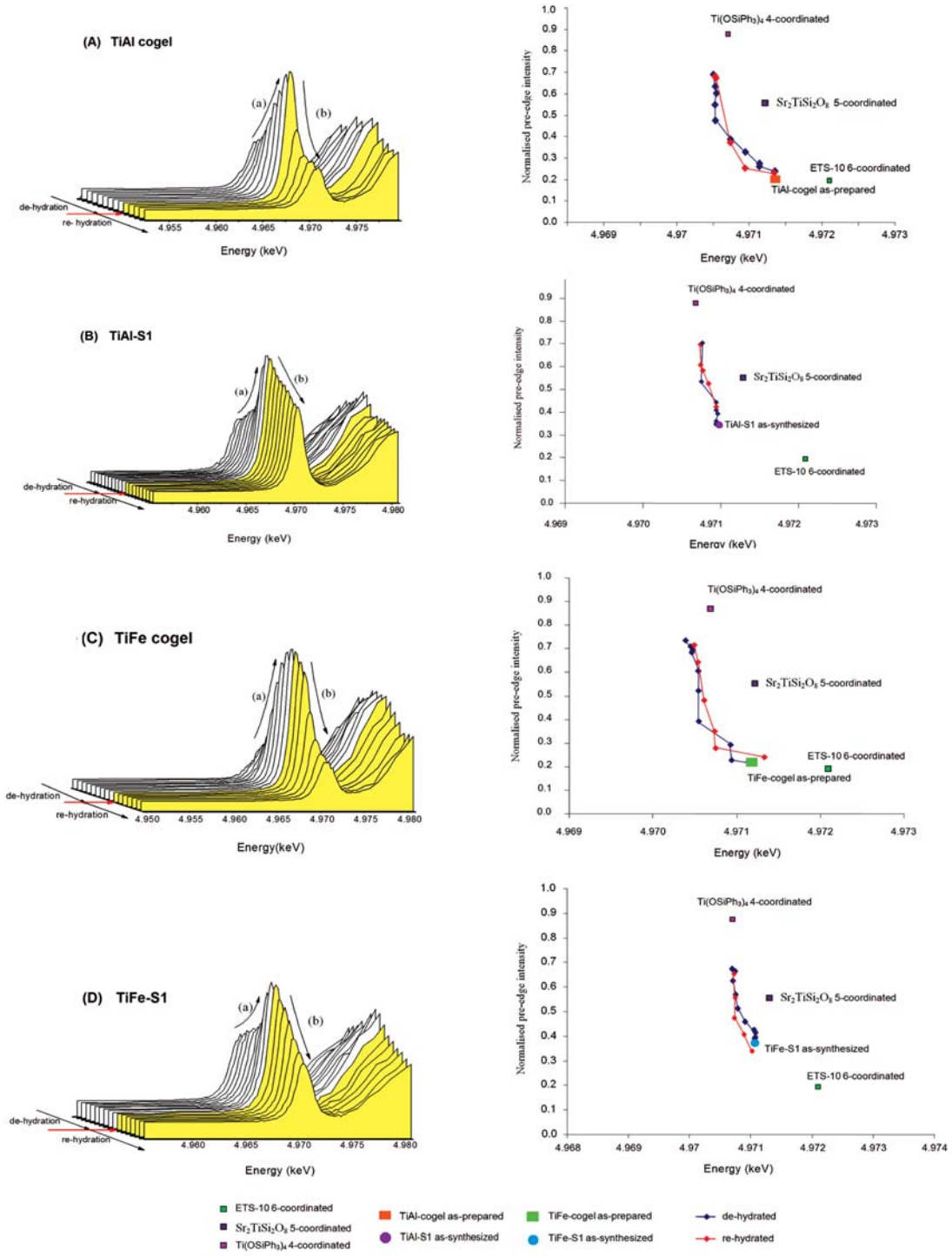

Fig. 5. *Pre-edge studies of Ti K-edge XANES of (A): TiAl cogel, (B): TiAl-S1, (C): TiFe-cogel; (D) TiFe-S1 recorded during an in situ study upon the calcination and re-hydration*

3.3. Study of Ti sites in TiAl-S1 system

3.3. 1. XANES study of TiAl-cogel

Pre-edge of Ti K edge XANES of the TiAl-cogel, TiAl-S1 and TiFe-cogel, TiFe-S1 (will be discussed in 3.3) are co-plotted in Fig. 5, in which on the left is the complete plot of Pre-edge of Ti K edge XANES and on the right is the pre-edge intensity vs energy positions compared with the model compounds.

As seen in Fig. 5A and Table 2, the intensity of the XANES pre-edge of the TiAl-cogel, similarly to Ti-cogel, increased upon the de-hydration to 400°C (a) and decreased upon re-hydration (b) with the pre-edge intensity shifted back to a higher energy, showing the changing local environment of Ti sites in the system.

Pre-edge intensities of the re-hydrated TiAl-cogel are much lower than that of the de-hydrated one. Compared with model compound $Ti(OSiPh_3)_4$, all as-prepared/re-hydrated sample have a lower pre-edge intensity. However the position of the pre-edge of the de-hydrated sample is identical to that of $Ti(OSiPh_3)_4$ and is at much lower energy compared with ETS-10. Upon exposure to atmosphere, the decrease in pre-edge intensity of the XANES clearly indicates that water molecules interact with the titanium centre yielding a distorted octahedral coordination. However, this distorted octahedral coordination is not like the octahedral coordination generated in ETS-10 system.

The reactivity of pre-edge peak in TiAl-cogel XANES spectrum showed that prior to crystallisation, the cogel contained a mixture of Ti^{IV} and Ti^{VI} geometry

3.3.2. XANES study of TiAl-S1

As-prepared TiAl-S1 K-edge has a very similar behavior with TS-1, showing that de-hydrated TiAl-S1 contain Ti^{IV}. After the calcinations, tetrahedral titanium centres are produced in the system. Upon exposure to the atmosphere, the decrease in pre-edge intensity of the XANES clearly indicates that water molecules interact with the titanium centre yielding a distorted octahedral coordination. However, this distorted octahedral coordination is not like the octahedral coordination generated in ETS-10 system.

Compared with pre-edge feature of $Ba_2TiSi_2O_8$, this suggests that the titanium centres of TiAl-S1 are in a mixture of tetrahedral and octahedral coordination rather than a pentahedral one. The pre-edge position in XANES spectra of TiAl-S1 is more similar to that for a tetrahedral system (with dehydrated material) and for octahedral system (with hydrated material) than for a pentahedral one.

3.4. Study of Ti sites in TiFe-S1 system

3.4.1. XANES study of TiFe-cogel

As shown in Fig. 5C and Table 3 the intensity of pre-edge in XANES of the TiFe-cogel increased upon the increasing temperature of de-hydration to 400°C and decreased upon the re-hydration.

Compared with three model compounds, it can be confirmed that prior to crystallisation, the TiFe-cogel has contained a mixture of titanium sites of Ti^{IV} and Ti^{VI} coordination geometry.

3.4.2. XANES study of TiFe-S1 system

From Table 3 and Fig. 5D, this reactivity shows that the Ti^{IV} sites in the de-hydrated system changed to distorted octahedral after the re-hydration.

It can be seen clearly that the pre-edge intensities of the as-prepared/re-hydrated TiFe-S1 are much lower than that of the de-hydrated one showing two different type of coordination. There is a significant difference between the pre-edge intensity of as-prepared/re-hydrated materials with model compound $Ti(OSiPh_3)_4$. The re-hydrated samples have a much lower pre-edge intensity than $Ti(OSiPh_3)_4$ but the intensities are close to pre-edge intensity of ETS-10, suggesting that this material generated a distorted octahedral coordination of titanium sites. However, it does not generate the type of octahedral coordination seen for ETS-10 as its pre-edge energy is lower.

Table 3. *Ti K-edge XANES features of TiFe-cogel and TiFe-S1*

Pre-edge features	TiFe-cogel sample			TiFe-S1 sample		
	Before dehydration (As-prepared)	At 400°C	After rehydration	Before dehydration (As-prepared)	At 400°C	After rehydration
Pre-edge intensity	0.22444	0.72053	0.23855	0.37993	0.66227	0.34324
Pre-edge position, keV	4.97114	4.97054	4.97134	4.97114	4.97074	4.97094

4. Conclusion

XANES study of all cogel precursors and as-synthesized/de-hydrated MFI materials can be rationalized by considering that titanium in all these materials exist in a mixture of two types of coordination geometry. One type of site is tetrahedral and inaccessible to water molecules (hydrophobic). The other type of site is distorted octahedral containing four oxygens of the framework and two oxygens from water molecules (hydrophilic sites). This octahedral environment is different from that of Ti sites generated in ETS-10 model compound (Fig. 1). Pre-edge features of Ti K-edge XANES spectra of these materials suggest that Ti^{IV} is the dominant Ti coordination in dehydrated system whilst Ti^{VI} is dominant in the re-hydrated one.

The reactivity of pre-edge features (positions and heights) upon de/re-hydration can be explained by numbers of tetrahedrally/octahedrally coordinated titanium sites in the mixture. Upon dehydration, two loosely bound water molecules are desorbed from octahedrally coordinated titanium leading to a lower number of hydrophilic sites. As a result, the pre-edge intensity is higher and more similar to that for a tetrahedral system. In re-hydrated samples, when we have a higher number of hydrophilic sites, the pre-edge intensity is lower and more similar to that for an octahedral system.

One of the main conclusions that may be derived based on this study is that, TS-1 is much more hydrophobic than TiAl or TiFe systems. In particular uptake of water appears to indicate that titanium ions are more hydrophilic in these systems. This may have relevance in designing catalytic reactions. Welch [2] showed in her work that TS-1 has more selectivity towards epoxide formation compared to either co-gel or TiAl or TiFe systems. This implies that more the hydrophilic character are present in the other systems and hence further break down of epoxide to diol and other by-products which are catalysed by weak acid sites. Further work, in particular during "actual catalytic reactions" is needed to further confirm these results.

More importantly, this study, once again, re-confirms the sensitivity of pre-edge in XANES with the changing of local environment of metal sites in nanoporous materials.

Acknowledgement

Hanoi University of Science and Technology, Royal Institution of Great Britain, University College London are acknowledged for encouragement and financial support.

References

1. C. Zenonos. *Synthesis and Characterization of metal substituted microporous materials*. Doctoral thesis. Royal Institution of GB. 2003.

2. A. Welch. *Doctoral thesis*. Royal Institution of GB. 2007.

3. R. A. Sheldon, I. W. C. E. Arends, and H. E. B. Lempers. *Collection of Czechoslovak Chemical Communications*. 1998; 68: P. 1724.

4. J. M. Thomas and G. Sankar. *Journal of Synchrotron Radiation*. 2001; 8: p. 55.

5. R. A. Sheldon. *Journal of Molecular Catalysis*. 1983; 20 (1): p. 1.

6. L. Bonneviot, D. T. On, and A. Lopez. *Journal of the Chemical Society - Chemical Communication*. 1993; 8: p. 685.

7. F. Farges, G. E. Brown JR., A. Navrotsky, H. Gan and John J. R. *Geochimica et Cosmochimica Acta*. 1996; Vol. 60 (16): p. 3039.

8. A. Eldewik, Russell F. Howe. *Microporous and Mesoporous Materials*. 2001; 48: p. 65.

9. Y. K. Krisnandi, P. D. Southon, A. A. Adesina and Russell F. Howe. *International Journal of Photoenergy*. 2003; Vol. 5: p. 131.

10. C.M. Barker, D. Gleeson, N. Kaltsoyannis, C.R.A. Catlow, G.Sankar and J.M. Thomas. *Physical Chemistry Chemical Physics*. 2002; 4 (7): p. 1228.

11. F. Farges, G. E. Brown JR. and John J. R. *Geochimica et Cosmochimica Acta*. 1996; Vol. 60 (16): p. 3023.

12. G. Perego, G. Bellusi, C. Corno, M. Tarramaso, F. Buonomo, and E. Esposito. *Studies in Surface Science and Catalysis*. 1986; 29: p. 129.

13. B. F. G. Johnson, M. C. Klunduka, C. M. Martina, G. Sankar, S. J. Teatec and J. M. Thomas. *Journal of Organometallic Chemistry*. 2000; 596 (1 - 2): p. 221.

A two-phase model for the development of positive surface discharge in air

Tran Nam Trung
Vietnam Electricity
Igor O Golosnoy, Paul L Lewin
School of Electronics and Computer Science, University of Southampton
Tran Khanh Viet Dung
Vietnam Oil and Gas Group

Abstract

This paper is concerned with the simulation of positive surface discharge - a frequently encountered phenomenon in high voltage electrical equipment. The development of a filamentary positive surface discharge in air is simulated using the hydrodynamic drift-diffusion approximation. The model consists of a set of continuity equations accounting for the movement, generation and loss of charge carriers (electrons, positive and negative ions). The continuity equations are coupled with Poisson's equation to take into account the effect of space charge on the electric field. The discharge is separated into two phases: the axial propagation of a streamer in the gas gap between a needle electrode and an insulator in phase I and the radial development of the streamer along the dielectric surface in phase II. The first phase is simulated in 2D axial symmetry using the finite element method. In phase II, the streamer is assumed to occupy a cylindrical channel of fixed radius and is solved in 1D using the accurate finite-volume flux-corrected transport algorithm. It is found that the streamer dynamics are strongly governed by the electric field created by the dielectric barrier. Comparisons between simulation results and experimental measurements are also made.

1. Introduction

The generation of non-thermal plasmas has been a topic of interest in recent years due to the broad range of applications it may offer. Most applications utilise the dielectric barrier discharge (DBD) arrangement to effectively control the current and charge distribution [1, 2]. At atmospheric pressure, DBDs have found their applications in large-scale ozone production, plasma display panels, thin film deposition, actuators for flow control, CO_2 lasers and excimer ultra-violet light sources [1, 3]. Surface discharges at triple-junctions in gas-insulated switchgear (GIS) have also attracted a large amount of research due to their critical influence on insulation system coordination.

It has been well established that the discharge pattern depends on the applied voltage polarity. A negative discharge produces a diffuse/circular form of surface charge [4, 5] whilst a positive discharge generates a filamentary streamer structure [6 - 8]. The surface charge distribution can be measured using dust Figures, Lichtenberg Figures, electrostatic probes or the Pockels technique [9, 10]. Out of these methods, the Pockels technique is the only method that provides quantitative analysis of the discharge dynamics.

The simulation of surface discharge phenomena provides better understanding of charge accumulation processes, facilitates effective control over the discharge parameters and is a useful tool for insulation system dimensioning. The modelling of a negative surface discharge has been reported in 2D axial symmetry space dimension [11]. In this paper, the development of a positive surface streamer is simulated and compared with experimental Pockels results. The hydrodynamic drift-diffusion approach is utilised which consists of coupled continuity equations for the charge transport and Poisson's equation for the electric field distribution [1]. The simulation consists of two phases: the axial propagation of streamer in the gas gap between a needle electrode and an insulator and the radial development along the dielectric surface. The second phase of the model helps

to capture the streamer dynamics under different electric fields using reasonable simplifications.

2. Experiment

Fig. 1 shows the schematic diagram of the Pockels experiment to measure surface discharge dynamics. A 17mW HeNe laser source is utilised to generate a coherent polarised light of 632.8nm wavelength. The light is expanded to a diameter of 30mm using a Galilean beam expander prior to arriving at the polarising beam splitter (PBS). The PBS serves as both a polariser and analyser. Having passed through the PBS, the input light is horizontally polarised. It is then modulated by an optical phase modulator (OPM), which is stressed with a square pulse waveform generated from an amplifier. The OPM is made of a 1mm thick Bismuth Silicon Oxide (BSO) crystal with the principal axes positioned 45° with respect to the horizontal. The sensing Pockels crystal is wedge polished to approximate dimensions of 20 × 20 × 0.16mm^3 and glued to a 0.8mm thick BK7 glass with one side grounded via a transparent electrode (Indium Tin Oxide). A needle electrode of 25μm radius of curvature is placed 500μm distant away from the other side of the crystal in order to avoid any undesired mechanical birefringence. The applied voltage waveform is programmed by a function generator and amplified using a high voltage amplifier. The discharge crystal is housed in a vacuum chamber connected to a vacuum pump or an air compressor and a pressure gauge. Light reflected from the back-face of the crystal passes through the PBS again and only the vertical component of the light is transmitted to the CCD camera. The lens and pinhole are placed in between the PBS and camera in order to block unnecessary reflections. The OPM operation, discharge triggering process and camera capturing are all synchronised by the synchronisation control circuit (SCC) programmed in a peripheral interface controller (PIC). Images obtained from the camera are transferred to a personal computer for further image processing after each experiment.

The principle of the electro-optic experiment is based on the Pockels characteristic of some materials such as BSO. Under the electric field induced by surface charge, the refractive indexes of the BSO crystal along two perpendicular principal axes (so-called fast and slow axes) are altered. The change in the refractive indexes leads to a linear phase retardation of the incident light. The change in phase is linearly proportional to the internal electric field. By measuring intensity of the reflected light, the phase retardation can be determined and hence the surface charge density. Further details of the experiment can be found in Y L Sam et al [9]. Similar experimental arrangement and results have also been reported in D Tanaka et al [6].

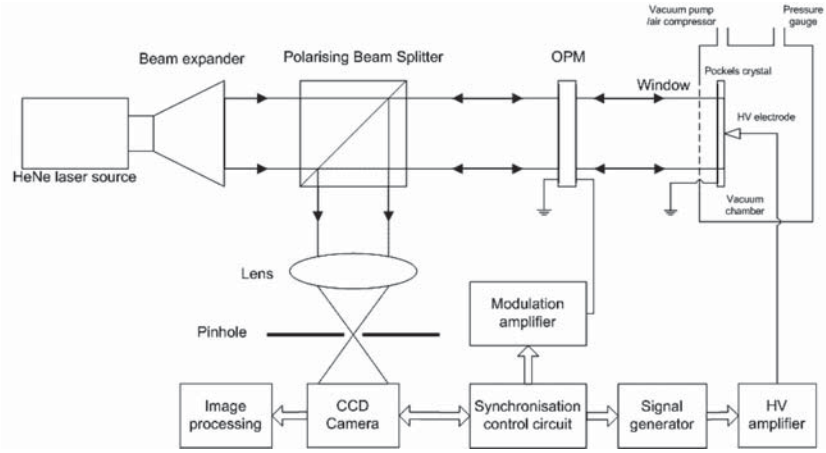

Fig. 1. *Schematic diagram of the Pockels experiment*

3. Model description

3.1. Governing equations

Based on the well-known hydrodynamic drift-diffusion model [1, 12], the set of continuity equations (to account for the movement, generation and loss of electrons, positive and negative ions and for the development of space charge) coupled with Poisson's equation (to include the effect of space charge on the electric field) is given as:

$$\frac{\partial N_e}{\partial t} = S + N_e\alpha\left|\overrightarrow{W_e}\right| - N_e\eta\left|\overrightarrow{W_e}\right| - N_eN_p\beta_{ep} - \nabla.\left(N_e\overrightarrow{W_e} - D_e\nabla N_e\right) \quad (1)$$

$$\frac{\partial N_p}{\partial t} = S + N_e\alpha\left|\overrightarrow{W_e}\right| - N_nN_p\beta_{np} - N_eN_p\beta_{ep} - \nabla.\left(N_p\overrightarrow{W_p} - D_p\nabla N_p\right) \quad (2)$$

$$\frac{\partial N_n}{\partial t} = N_e\eta\left|\overrightarrow{W_e}\right| - N_nN_p\beta_{np} - \nabla.\left(N_n\overrightarrow{W_n} - D_n\nabla N_n\right) \quad (3)$$

$$\nabla.\left(\varepsilon_r\nabla V\right) + \frac{e}{\varepsilon_0}\left(N_p - N_e - N_n\right) = 0 \quad (4)$$

Where t is time, e the electronic charge, ε_0 the vacuum permittivity and ε_r the relative permittivity of the medium, V the electric potential; N_e, N_p and N_n the electron, positive and negative ion concentrations respectively; $\overrightarrow{W_e}$, $\overrightarrow{W_p}$ and $\overrightarrow{W_n}$ the electron, positive and negative ion drift velocities; α, η, β, D_e, D_p and D_n the ionisation, attachment, recombination and diffusion coefficients for electrons and positive and negative ions respectively. The source term S represents the photoionisation process. The swarm parameters, which are functions of the local electric field, $\vec{E} = -\nabla V$, are extracted from the approximations published in [13] and modifications detailed in [14].

3.2. Computational domain

The simulation geometry utilised in this work is shown in Fig. 2. A hyperboloid needle electrode of 25µm radius of curvature was modelled. A system of two dielectric layers was utilised to resemble the Pockels cell. A 160µm thick BSO layer (ε_r = 56) was set on top of an 800 µm thick glass (ε_r = 3). Both layers share the same radius of 10mm. The BSO surface was set 500µm away from the needle electrode. The ground electrode was set at the bottom of the glass. The simulation domain dimensions are 10mm by 10mm. Unless otherwise stated the model assumes atmospheric pressure and room temperature.

3.3. Numerical algorithm and boundary conditions

Equations 1 - 4 should ideally be solved in 3D due to the asymmetry of the streamer pattern. However, this approach was found ineffective as it would have cost a vast amount of computational time and resources. In this paper, the simulation of a positive surface discharge is separated into two phases. In the first phase, due to the strong axial electric field at the needle tip a streamer forms and travels towards the insulator. This phase was fully simulated in 2D axial symmetry space dimension (effectively 3D). When the streamer arrives at the dielectric surface, the dielectric acts as an impermeable barrier causing the discharge to develop along the surface. All barrier discharge models to date continue simulating the discharge in the same 2D space dimension [15 - 17]. This results in a ring form of the streamer. Nonetheless from experimental results, the streamer does not expand radially but rather forms filamentary branches. The branching phenomena have been attributed to instabilities and asymmetric distribution of electrons where the gas streamer interacts with the dielectric surface [18]. For this reason, the second phase of the model proposed in this paper describes the development of one particular streamer along the surface. This phase was simulated in 1D by assuming the streamer propagates along the insulator surface in the form of a cylindrical channel of fixed radius. The radial field calculated at the end of the first phase is used as the driving force for the streamer development in the second phase.

The first phase was solved using the conventional finite element method with an addition of streamline artificial anisotropic diffusion [9]. This approach has proved effective in solving discharge problems in gas and liquid [20, 21] although other advanced techniques for transport problems can be used [22].

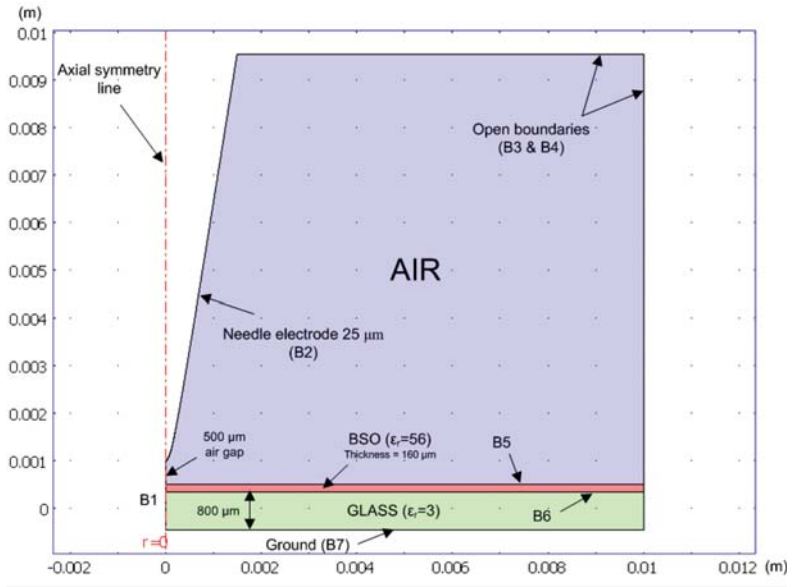

Fig. 2. *Positive surface discharge model geometry*

With regard to the meshing of the geometry, a mesh size of 2.5µm in the region near the symmetry axis and the needle electrode was found sufficient to simulate the development of a streamer in phase I. The total number of mesh elements created was approximately 150,000 giving rise to just above 1 million degrees of freedom to solve. In the first phase, the time steps vary in the range of 10^{-13} - 10^{-11}s. The total runtime was under 6 hours using a single core 3 GB RAM personal computer.

Boundary conditions for the first phase are summarised in Table 1. The boundary conditions of interest are those at the gas-insulator interface (B5). There are generally two types of boundary condition for this

Table 1. *Boundary conditions for the second phase of the positive surface discharge model with reference to Fig. 2*

	Boundary conditions for N_e	Boundary conditions for N_p	Boundary conditions for N_n	Boundary conditions for V
Boundary 1	$\frac{\partial N_e}{\partial r}=0$	$\frac{\partial N_p}{\partial r}=0$	$\frac{\partial N_n}{\partial r}=0$	$\frac{\partial V}{\partial r}=0$
Boundary 2	$\vec{n}\cdot(-D_e\nabla N_e)=0$	$\vec{n}\cdot(\overrightarrow{W_p}N_p - D_p\nabla N_p)=0$	$\vec{n}\cdot(-D_n\nabla N_n)=0$	V = 4000 (V)
Boundaries 3 & 4	$\vec{n}\cdot(-D_e\nabla N_e)=0$	$\vec{n}\cdot(-D_p\nabla N_p)=0$	$\vec{n}\cdot(-D_n\nabla N_n)=0$	$\vec{n}\cdot(\varepsilon_0\varepsilon_r\vec{E})=0$
Boundary 5	$\vec{n}\cdot(\overrightarrow{W_e}N_e - D_e\nabla N_e)=0$	$\vec{n}\cdot(\overrightarrow{W_p}N_p - D_p\nabla N_p)=0$	$\vec{n}\cdot(\overrightarrow{W_n}N_n - D_n\nabla N_n)=0$	$\vec{n}\cdot(\overrightarrow{D_1}-\overrightarrow{D_2})=0$
Boundary 6	-	-	-	$\vec{n}\cdot(\overrightarrow{D_1}-\overrightarrow{D_2})=0$
Boundary 7	-	-	-	V = 0

dielectric interface to simulate the charge accumulation process. The first type sets the fluxes of charged particles to zero; the dielectric acts as an impermeable media. The plasma is hence contained completely in the gas [15, 17]. The second type allows charged particles to go through and the integration of charged particle fluxes yields the surface charge density [3, 11]. The charges accumulate at the surface in this case and are separated from the plasma in the gas. The former approach works best with dynamic structure whereas the latter is suitable for less dynamic cases. For this reason, the former boundary condition was used for the proposed model.

Table 2. *Boundary conditions for the second phase (1D) of the positive surface discharge model*

Charge species	Left boundary	Right boundary
Electrons	$-D_e\frac{\partial N_e}{\partial x}=0$	$W_eN_e - D_e\frac{\partial N_e}{\partial x}=0$
Positive ions	$W_pN_p - D_p\frac{\partial N_p}{\partial x}=0$	$-D_p\frac{\partial N_p}{\partial x}=0$
Negative ions	$-D_n\frac{\partial N_n}{\partial x}=0$	$W_nN_n - D_n\frac{\partial N_n}{\partial x}=0$

The second phase of the model is simplified to 1D as the streamer is assumed to occupy a cylindrical channel of fixed radius. Charge densities vary along the channel axis but remain uniform at each cross-section. The continuity equations 1 - 3 were rewritten in 1D and solved using the accurate finite-volume flux-corrected transport (FV-FCT) algorithm [23]. The Boris-Book limiter has been utilised due to ease of implementation as compared to the equivalently good Zalesak limiter. A time step of 10^{-13} s and a uniform mesh of 1μm size were chosen. These parameters were selected to ensure the Courant-Friedrichs-Lewy (CFL) number much less than 0.5 for stability purposes. Boundary conditions in phase II are summarised in Table 2.

Poisson's equation 4 in phase II was solved by a revised disc method. In this method, the streamer channel is divided into minute discs and the total space charge field is calculated as an integration of the field generated from each disc [19, 24]. The channel radius chosen in this simulation was 50μm as this value has been measured experimentally and commonly used in gas discharge simulations [10, 25, 26]. The influence of this parameter on the discharge development is also studied in this paper. A thickness of 4 μm was chosen for each minute disc as it has been shown to produce good field results with acceptable computational run time [19]. The revised disc method used in this work assumes that image charges on the metal electrode and dielectrics play a minor role in the field calculation. In order to justify this assumption, a comparison between the field calculated using the disc method and that calculated by the finite element analysis in 3D has been made using the same space charge distribution [19]. It has been concluded that the revised disc method is acceptably accurate to be used in surface

discharge modelling. The difference between the field magnitudes obtained from both methods is under 10%.

4. Simulation results

4.1. Phase I

A Gaussian distribution of neutral plasma (seed electrons and positive ions) with the peak value of 10^{14} m^{-3} and width of 25μm was set at the needle tip to commence the discharge [14, 19]. The initial plasma distribution has been confirmed to only speed up the streamer formation process and not affect the streamer characteristics [26]. The source term *S* in equations 1 - 2 indicates the rate of electron-ion pairs generated from the photoionisation process and was simulated as $10^{26}m^{-3}s^{-1}$ in this model [14, 18]. This is a simple approximation to realise processes caused by radiated photons in the gas and has been utilised by some authors [27, 28]. In order to have a similar voltage waveform to that used in the experiment, a step voltage of 4kV was used in the simulation.

Simulation results obtained in the first phase are presented in Fig.s 3 - 7. The first observation is that the streamer travels in the gas gap as an ionising wave. This structure is characterised by a moving streamer head which has a strong electric field and a quasi-neutral density stem behind it. Fig. 3 shows the 2D electric field distribution at various times up until the instant the streamer reaches the dielectric surface. When the streamer has fully developed in the gas (0.4ns) its radial field expansion reaches around 200μm. The streamer head width falls in the range from 50 - 100μm. The axial field plot along the symmetry axis, Fig. 5(d), clearly shows the changes in the magnitude of the streamer head field. The streamer forms after about 0.1ns and the streamer head field decreases while traversing across the gap. After 0.5ns the maximum field strength reduces from 7.2×10^7V/m to 2×10^7V/m. When the streamer reaches the vicinity of the dielectric with high permittivity the streamer head field is enhanced greatly (0.575ns curve). At this interface region, the electric field changes its magnitude and shape.

Fig. 4 shows the 2D positive ion and electron density distributions at various times at which the respective field distributions in Fig. 3 are plotted. As shown in Fig. 5(c) the negative ion density is of one order lower than the others; its contribution to Poisson's equation is negligible

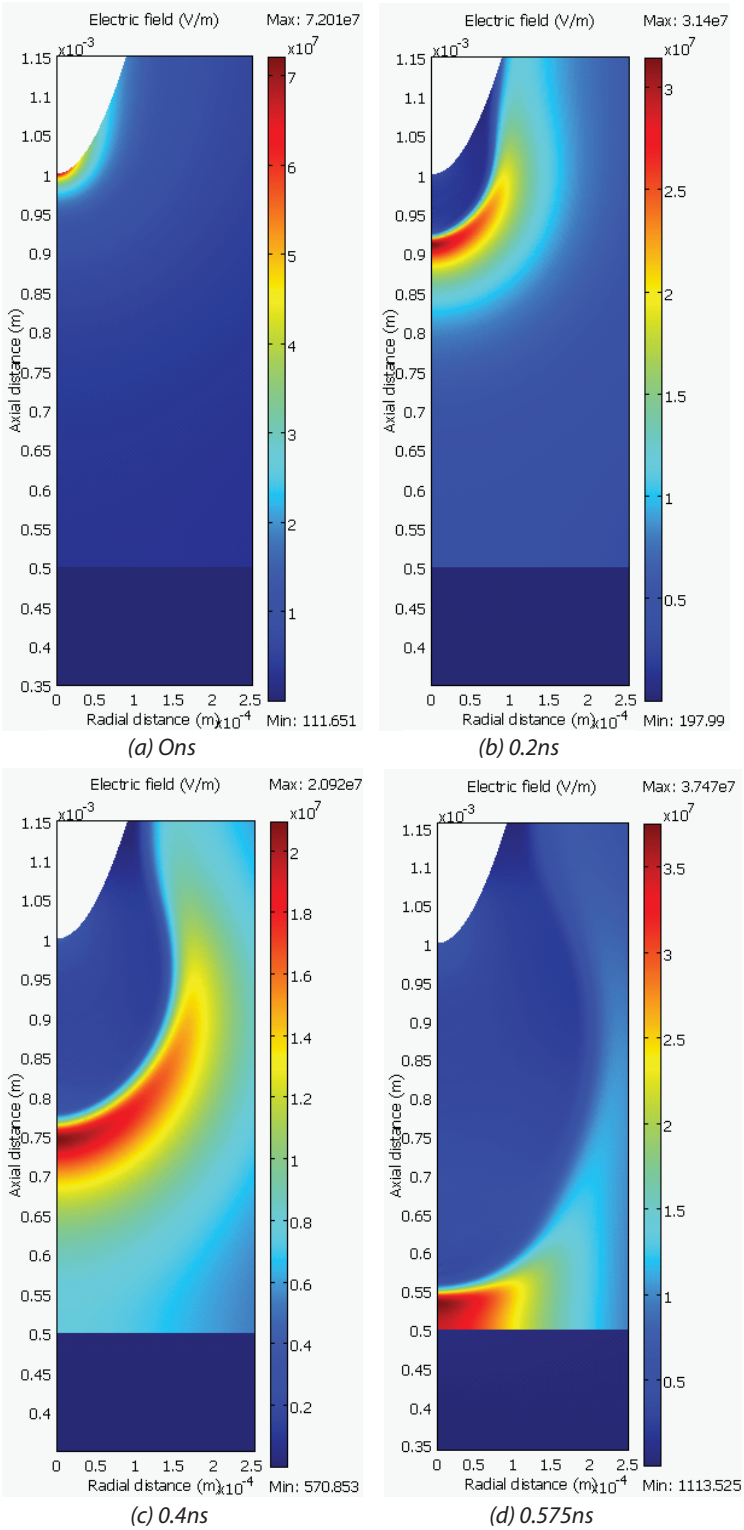

Fig. 3. *2D electric field distribution at various times in phase I*

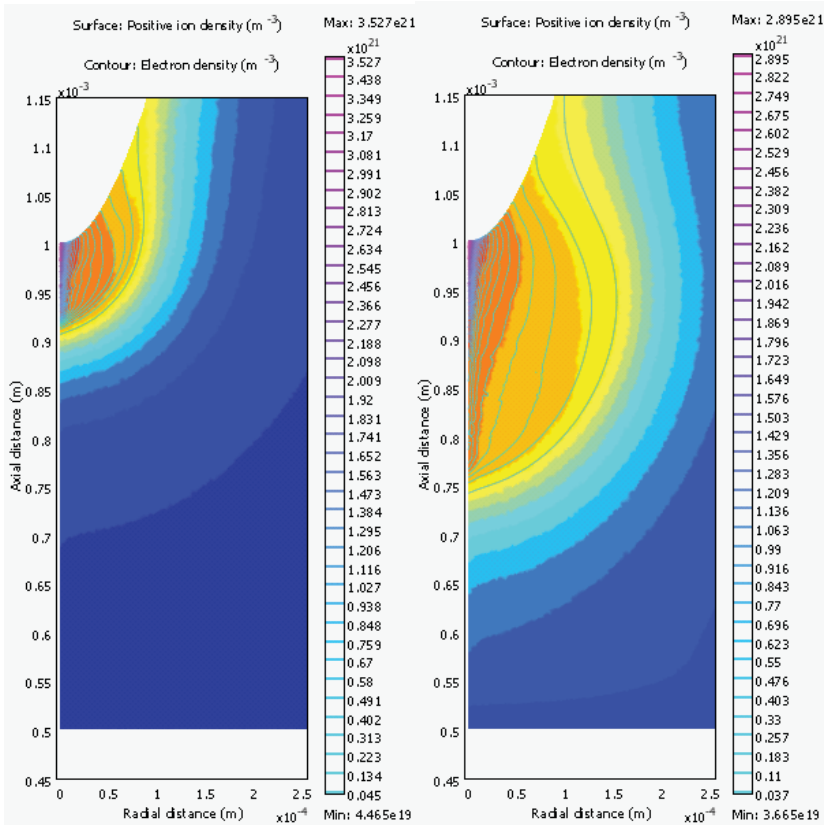

(a) 0.2ns *(b) 0.4ns*

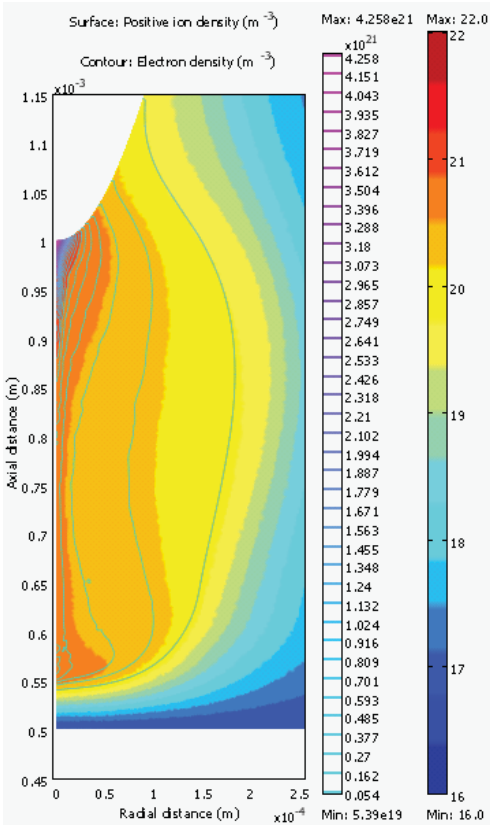

(c) 0.575ns

Fig. 4. *2D positive ion and electron density distributions at various times in phase I*

and is hence not shown in the 2D plots. Both positive ions and electrons are highly concentrated in a narrow volume along the symmetry axis (approximately $2 \times 10^{21} m^{-3}$) then quickly drop radially. The radial expansion of these species can be approximated to about 200 μm from the 2D plots. The electron density distribution follows that of positive ions to a good extent. The electron density is slightly lower than the positive ion density and displaced by a tiny distance towards the needle electrode, Fig. 5. This can be attributed for by the difference in mobility of electrons and positive ions and the fact that electrons are constantly sucked into the stem of the streamer and ultimately the anode. The positive ions, on the other hand, remain almost stationary where they are created. Electron attachment process also plays a role causing to the difference in the charge density magnitude. The displacement creates a positive net charge at the head and a quasi-neutral plasma in the stem. This explains the formation of the streamer head field. As the streamer advances and before reaching the dielectric, both charge densities drop to approximately $3.5 \times 10^{20} m^{-3}$. The densities start increasing as the streamer interacts with the dielectric surface.

In order to calculate the velocity of the streamer in phase I, the peak of the electric field is recorded as a function of time and distance. Fig. 6 shows the streamer velocity during its propagation in the gas gap. It is clear that the velocity increases as the streamer advances. The peak velocity obtained is just under $1.5 \times 10^{6} m/s$ at the position where the streamer is about to interact with the dielectric surface. After the peak, the streamer slows down to commence its radial development.

In order to determine the instant just before the streamer starts spreading

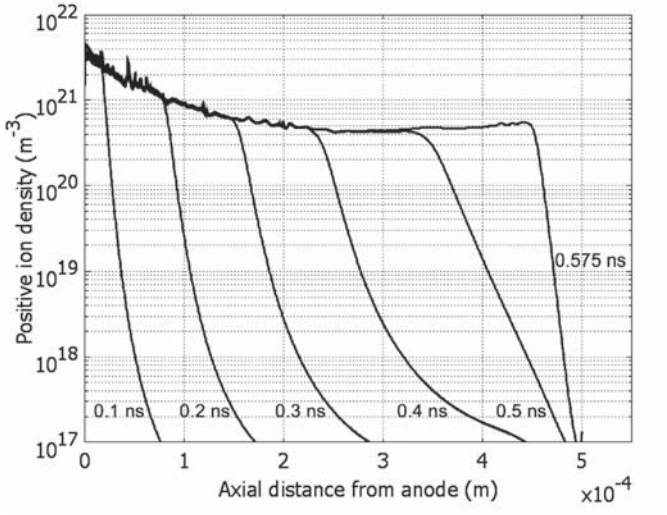

(a) Positive ion density distributions along the symmetry axis

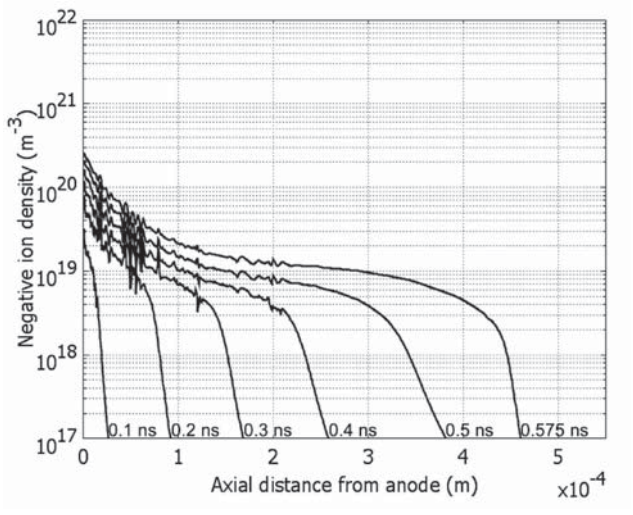

(c) Negative ion density distributions along the symmetry axis

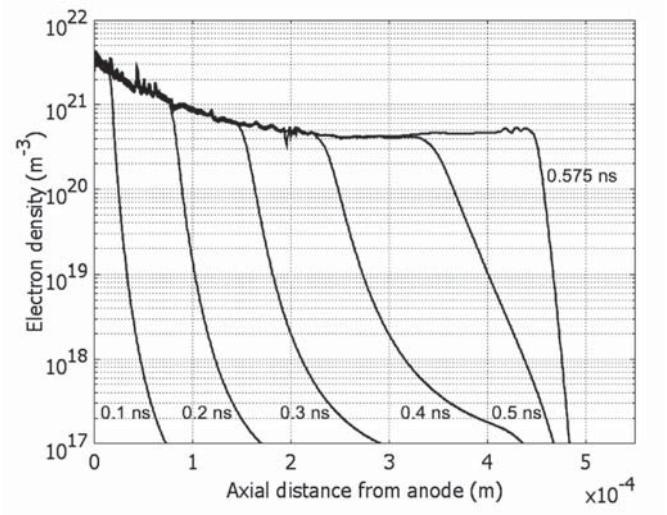

(b) Electron density distributions along the symmetry axis

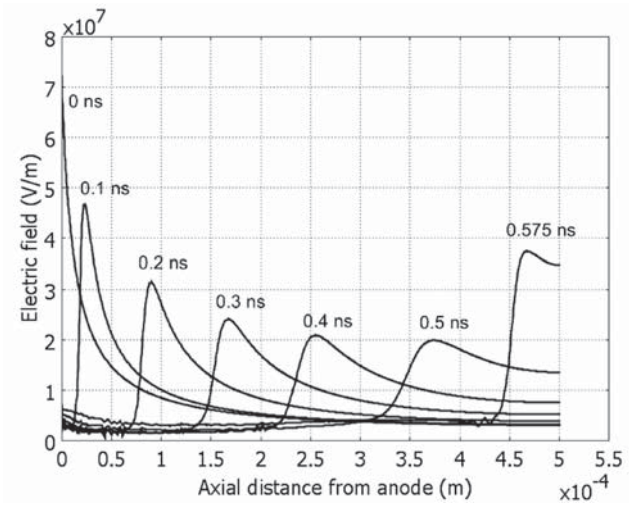

(d) Electric field distributions along the symmetry axis

Fig. 5. *Charged particle density and electric field distributions along the symmetry axis at various times in phase I*

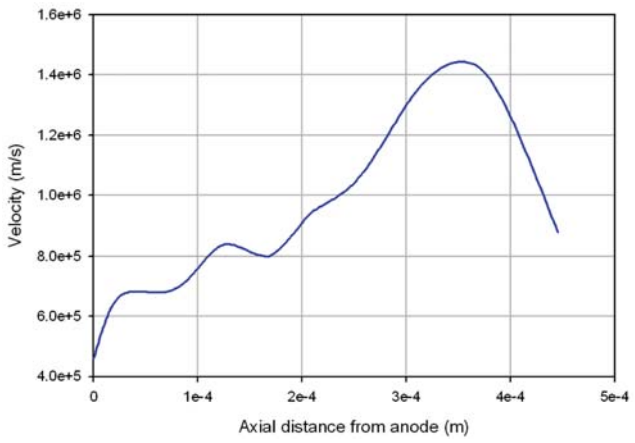

Fig. 6. *Streamer velocity versus distance in phase I*

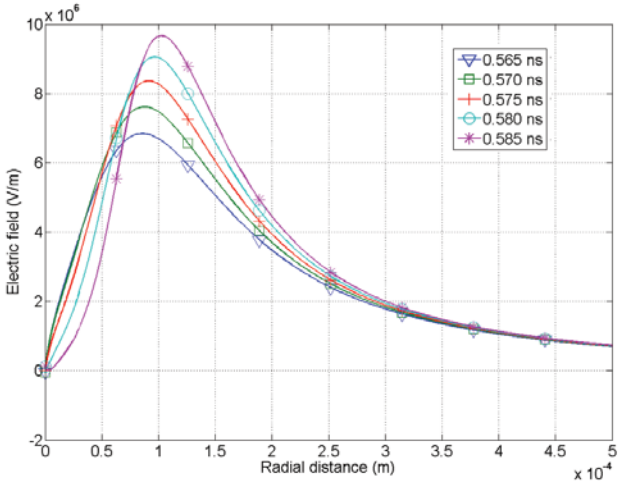

Fig. 7. *Radial electric field distribution at various times in phase I at 50μm above the dielectric surface*

out over the dielectric in the 2D axial symmetry space dimension, the plot of the radial field against distance at 50μm above the dielectric surface at various times was investigated. This plot is shown in Fig. 7. As can be observed, the radial field increases at a fast rate when the streamer approaches the dielectric. After 0.575ns, the streamer starts to move radially indicated by the movement of the electric field peak and the drop in the field near the symmetry axis. The radial field at 0.575ns was hence used as the driving force for the second phase of the simulation. The field peak reaches 8.2×10^6V/m at this time instant.

4.2. Phase II

Phase II of the simulation starts by using the radial field obtained at 0.575ns from the first phase as the initial electric field. It should be noted that measured streamers branch out from the centre of the insulator hence this phase only simulates the development of one streamer. It was assumed that the cylindrical streamer channel propagates directly above the BSO surface. All other parameters were kept the same as specified in phase I including the initial density conditions. The simulation results of the streamer propagating along the dielectric surface are shown in Fig.s 8 - 11. The first observation is that the streamer has the same ionising wave structure as in phase I. The streamer comes to a stop at around 3mm after 106ns with the specified parameters. At this point, the streamer head field is lower than the ionisation level in air (approximately 3×10^6V/m). As the streamer head field collapses, the field near the symmetry axis tends to increase back to the initial field due to the reduced effect of the space charge. The velocity plot (Fig. 9) clearly shows that the streamer in this phase undergoes two different stages during its propagation: the acceleration and deceleration. Near the origin, the streamer accelerates away until the maximum velocity of 8×10^4m/s is reached at around 0.6mm. It is then followed by the deceleration regime when streamer reaches the decaying tail of the initial field. The velocity in phase II is about 15 times less than that found in phase I. This can be accounted for by the fact that in phase I the initial applied field is much stronger (approximately 10 times) over a much shorter gap and also because of the field enhancement effect when the streamer interacts with the dielectric in phase I. The maximum velocity calculated in phase II is in good agreement with the experimentally measured values reported in [10, 29]. The electron and positive ion density profiles at three selected instants in time are shown in Fig. 10. It is evident that using the FCT algorithm the charge profiles are much smoother than those obtained from the finite element method in phase I. The positive ion density ($3 - 8 \times 10^{19}$m^{-3}) is clearly higher than the electron density everywhere due to the high mobility of electrons and their movement towards the left boundary. Both the electron and positive ion densities drop as the streamer advances. The negative ion density in this phase is of the order of 10^{17} m^{-3} and does not play a role in the streamer propagation as in the previous phase. The charge density in this phase is lower than that obtained in the previous phase due to the difference in the magnitude of the initial field.

The net charge density distribution presented in Fig. 11 evidently shows its correlation with the streamer head field. The net charge distribution is characterised with a high gradient spike at the front and a quasi-constant lower-density charge distribution in the stem. Near the origin, there is a negative charge region due to the high concentration of negative ions at low electric field. At 4 ns, the net charge spike has a sharp gradient and high magnitude (6×10^{19}m^{-3}). As the streamer develops, the spike becomes shorter and less sharp. After 90ns, the streamer

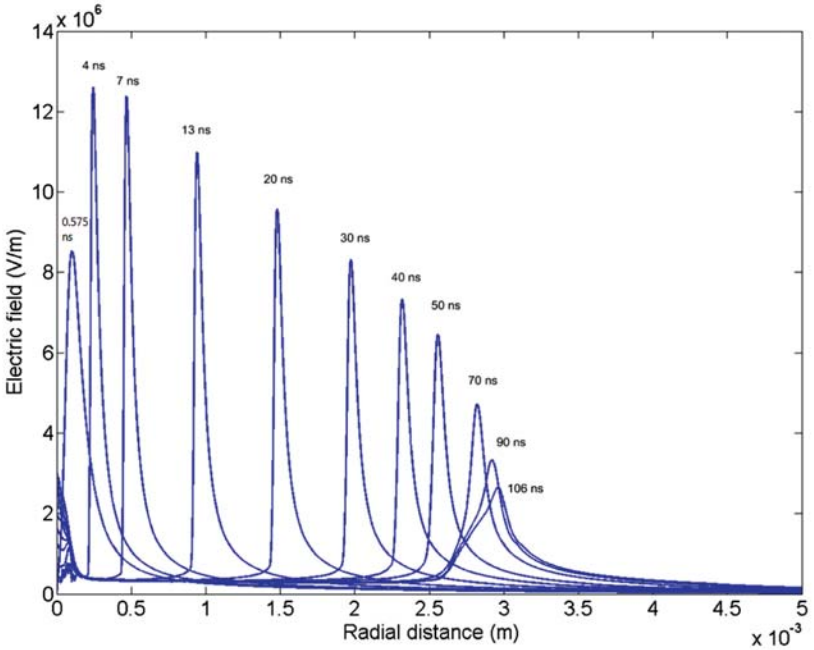

Fig. 8. *Electric field distribution at various times in phase II*

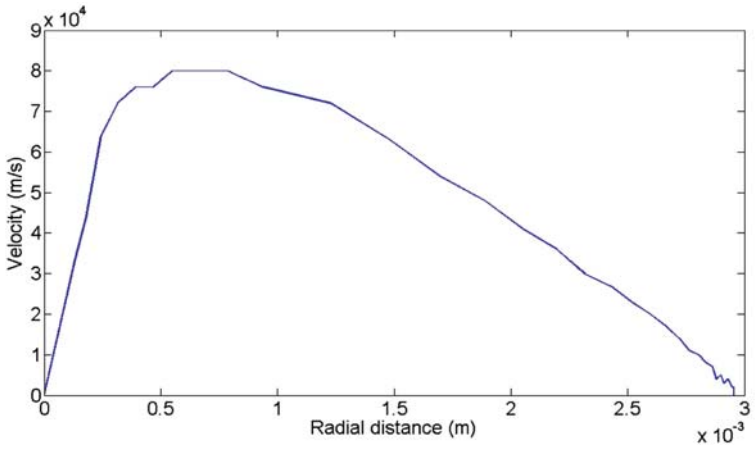

Fig. 9. *Streamer velocity versus distance in phase II*

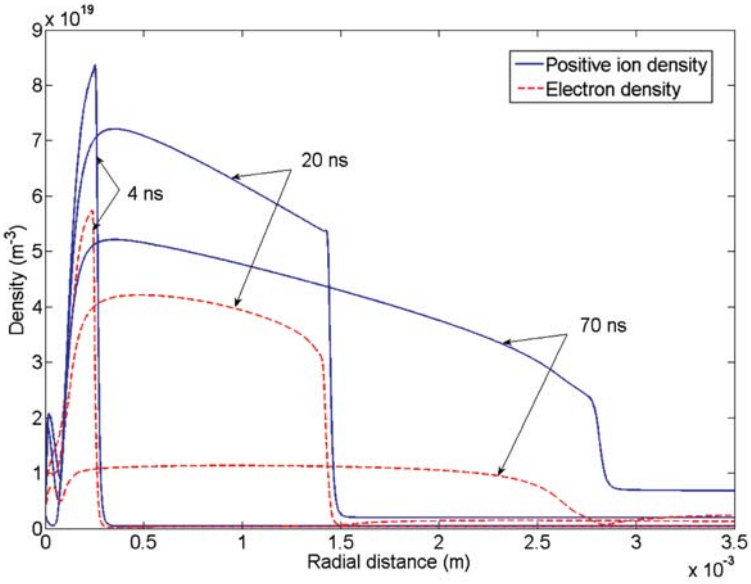

Fig. 10. *Electron and positive ion density distributions at 4, 20 and 70ns in phase II*

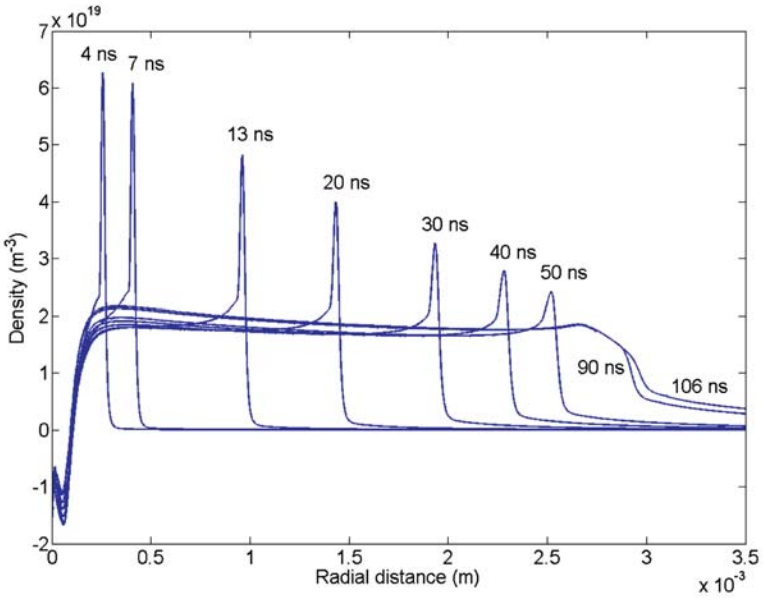

Fig. 11. *Net charge density distributions in phase II*

has travelled around 3mm and the net charge spike has a value lower than the maximum density in the stem of the streamer channel. The streamer totally collapses after 106ns; at this instant the net charge spike flattens and the streamer head field drops below 3×10^6V/m. The streamer length in this case is calculated as 3 mm which is in reasonable agreement with experimental results [10].

5. Comparison with experimental measurements

The Pockels method has been used to measure surface discharge under 4kV magnitude and 5ms square voltage waveform at atmospheric pressure. The 2D surface charge density distribution is shown in Fig. 12(a) while the line charge density along the dashed line (XY) is shown in Fig. 12(b). The discharge produces streamers of 4.5mm long and 0.7nCmm^{-2} density in average. The model proposed earlier predicts a streamer length of about 3mm. Nonetheless, the effects of the background ionisation and streamer radius have been investigated and it is confirmed that the streamer length is inversely dependent on the variation of these parameters. Hence in order to match the experimental streamer length a smaller background ionisation value or a smaller streamer radius can be used. As the streamer radius of 50μm has been widely used in the literature, this section presents a result comparison for the case of the background ionisation reduced to 5×10^{25}m^{-3}s^{-1}.

Fig. 13 demonstrates the evolution of the net charge density in the second phase of the model using this background ionisation value. It is clear that the streamer collapses at the distance of about 4.3 mm which is closer to the experimental measurement. Since the simulation provides the plasma space charge density, it is not possible to directly compare this quantity with the surface charge density measured from the Pockels experiment. However, comparison can be made between the electric field induced across the BSO crystal (*z*-component) due to the experimental surface charge and that due to the simulation space

charge. According to the electro-optic theory, this is the quantity the Pockels technique measures. The relationship between this electric field component and surface charge density takes the form

$$E_{z(x,y)} = \frac{\sigma_{(x,y)}}{2\varepsilon_0\varepsilon_r} \quad (5)$$

In order to calculate the *z*-component electric field due to the net space charge density, numerical modelling was required. The finite element method has been utilised in 3D for this analysis. The discharge geometry detailed in Fig. 2 was extended to 3D with a streamer set on top of the BSO layer - Fig. 14(a). The streamer is made of a 50μm radius and 4.3mm long cylinder. The charge density within this cylinder was set constant at $2 \times 10^{19} m^{-3}$ because this is the charge density in the stem of the streamer channel during both the acceleration and deceleration stages. The effect of the high density spike traversing across the dielectric surface is negligible since the streamer development duration (150ns) is much shorter than the camera exposure time (100 - 200μs). The recorded data is integrated images showing the field induced by the space charge density in the streamer stem. The *z*-component electric field was solved and the cross-sectioned distribution on the plane perpendicular to the BSO surface and going through the centre of the streamer is shown in Fig. 14(b). The impact of the space charge on the electric field across the BSO crystal is evident in this figure. Inspection of the *z*-component field along the *z* axis across the 160μm thick BSO shows that the field varies linearly. Hence the average electric field in the BSO can be found at a distance of 80μm below the top surface (dashed line in Fig. 14(b)). The plot of the electric field distributions obtained along this line and from the experimental surface charge is shown in Fig. 14(c). It can be seen that the simulation field is about one fifth of the experimental measurement. This fact suggests that charge injection into the insulator bulk is one of other factors contributing to the measured field.

6. Conclusion

The positive surface discharge has been simulated in two phases using the hydrodynamic drift-diffusion approximation. The first phase which involves the axial development of streamer in the gas gap was solved in 2D axial symmetry space dimension

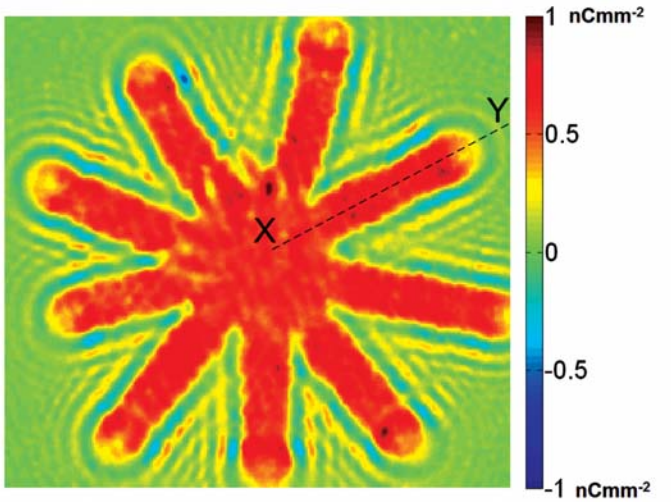

(a) 2D surface charge density distribution

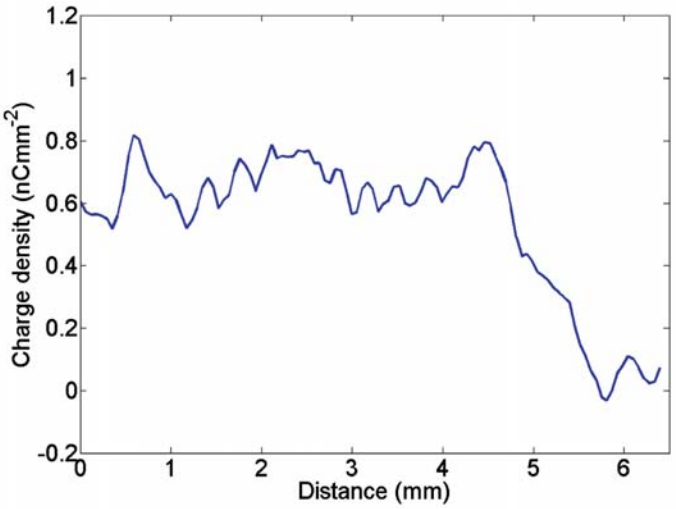

(b) Line charge density distribution

Fig. 12. *Experimental Pockels results obtained under 4kV magnitude 5ms duration positive square voltage waveform*

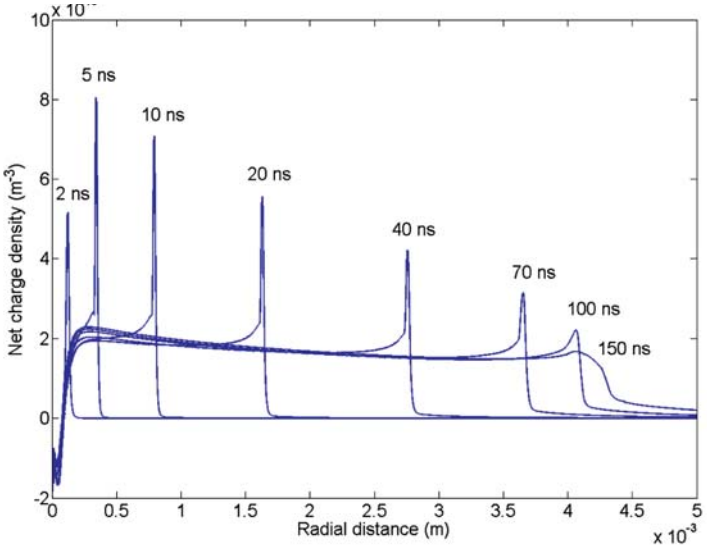

Fig. 13*. Phase II net charge density evolution for the positive surface discharge simulation obtained from* $S = 5 \times 10^{25} m^{-3} s^{-1}$

using the finite element analysis. The second phase uses the field results from the first phase and simulates the radial streamer propagation along the dielectric surface. This phase was simulated in 1D using the accurate FCT algorithm adopting some reasonable simplifications. The following observations have been made:

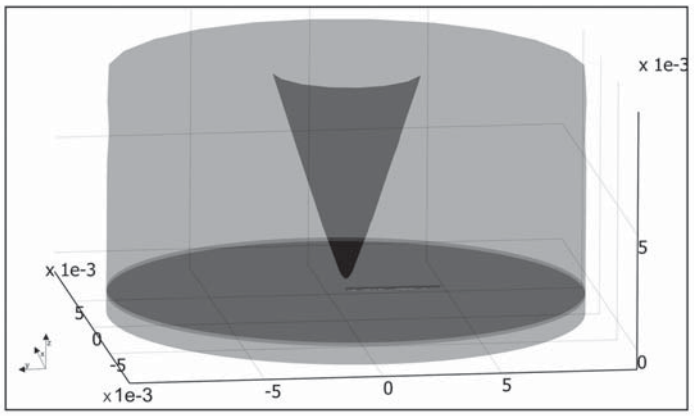

(a) 3D charge density distribution

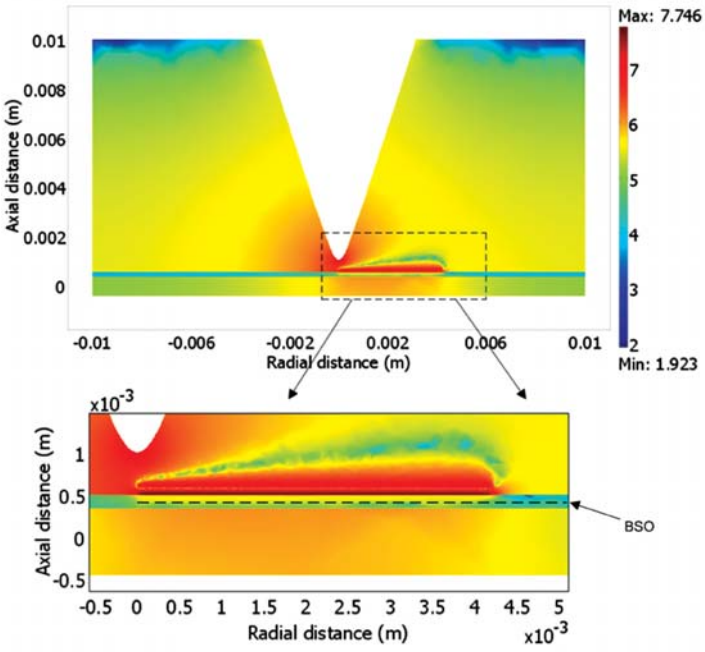

(b) Cross-sectioned z-component electric field distribution in log scale

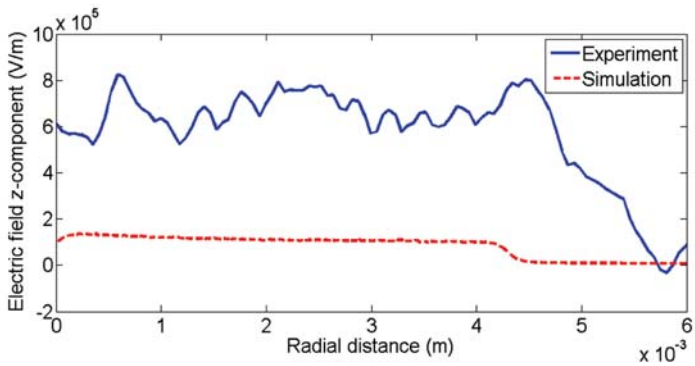

(c) z-component electric field distribution comparison

Fig. 14. *Comparison between simulation and experimental positive surface discharge results*

- The streamer shows the ionising wave structure in both phases. The streamer dynamics are strongly dependent on the electric field created by the dielectric barrier. In phase I, the streamer accelerates when it is about to interact with the dielectric surface.

- Phase II shows the acceleration stage followed by the deceleration. The field magnitude, charge densities and velocity are all smaller than in phase I.

- The simulation and experimental results have a good agreement in terms of streamer length when the ionisation source term of $5 \times 10^{25} m^{-3}$ is used. The *z*-component electric field obtained from the simulation is one fifth of the experimental measurement at atmospheric pressure.

References

1. Georghiou G E, Papadakis A P, Morrow R and Metaxas A C. *Numerical modelling at atmospheric pressure leading to plasma production* J. Phys. D: Appl. Phys. 2005; 38: p. 303 - 328.

2. Kogelschatz U. *Dielectric-barrier discharges: their history, discharge physics, and industrial applications*. Plasma Chemistry and Plasma Processing. 2002; 23: p. 1 - 46.

3. Lagmich Y, Callegari T, Pitchford L and Boeuf J. *Model description of surface dielectric barrier discharges for flow control*. J. Phys. D: Appl. Phys. 2008; 41.

4. Manabe Y and Shimazaki T. *Formation mechanism of surface corona on dielectric plates under negative impulse voltage in atmospheirc air*. IEEE Transactions on Dielectrics and Electrical Insulation. 2004; 11(4): p. 631 - 637.

5. Celestin S, Allegraud K, Canes-Boussard G, Leick N, Guaitella O and Rousseau A. *Patterns of plasma filaments propagating on a dielectric surface*. IEEE Transactions on Plasma Science. 2008; 36 (4): p. 1326 - 1327.

6. Tanaka D, Matsuoka S, Kumada A and Hidaka K. *Two-dimensional potential and charge distributions of positive surface streamer* J. Phys. D: Appl. Phys. 2009; 42 075204.

7. Timatkov V V, Pietsch G J, Saveliev A B, Sokolova M V and Temikov A G. *Influence of solid dielectric on the impulse discharge behaviour in a needle-to-plane air gap*. J. Phys. D: Appl. Phys. 2005; 38: p. 877.

8. Akyuz M, Cortet P P and Cooray V. *Positive streamer discharges along liquid dielectric surfaces: effect of dielectric constant and surface properties*. IEEE Transactions on Dielectrics and Electrical Insulation. 2005; 12 (3): p. 579 - 585.

9. Sam Y L, Lewin P L, Davies A E, Wilkinson J S, Sutton S J and Swingler S G. *Surface discharge measurements of polymeric materials*. IEE Proceedings: Science, Measurement and Technology. 2003; 150: p. 43 - 52.

10. Murooka Y, Takada T and Hidaka K. *Nanosecond surface discharge and charge density evaluation, part i: review and experiments*. IEEE Electrical Insulation Magazine. 2001; 17 (2): p. 6 16.

11. Tran T N, Golosnoy I O, Lewin P L and Georghiou G E. *Numerical modelling of negative discharges in air with experimental validation*. J. Phys. D: Appl. Phys. 2011; 44 015203.

12. I Gallimberti. *A computer model for streamer propagation* .J. Phys. D: Appl. Phys. 1972; 5: p. 2179 - 2189.

13. Morrow R and Lowke J. *Streamer propagation in air*. J. Phys. D: Appl. Phys. 1996; 30: p. 614 - 627.

14. Ducasse O, Papageorghiou L, Eichwald O, Spyrou N and Yousfi M. *Critical analysis on two-dimensional point-to-plane streamer simulations using the finite element and finite volume methods.* IEEE Transactions on Plasma Science. 2007; 35 (5): p. 1287 - 1298.

15. Papageorghiou L, Panousis E, Loiseau J, Spyrou N and Held B. *Two-dimensional modelling of a nitrogen dielectric barrier discharge (DBD) at atmospheric pressure: filament dynamics with the dielectric barrier on the cathode*. J. Phys. D: Appl. Phys. 2009; 42 (8): p. 105201 - 105210.

16. Kumara S, Serdyuk Y and Gubanski S. *Charging of polymeric surfaces by positive impulse corona*. IEEE Transactions on Dielectrics and Electrical Insulation. 2009; 16 (3): p. 726 - 733.

17. Celestin S, Bonaventura Z, Guaitella O, Rousseau A and Bourdon A. *Influence of surface charges on the structure of a dielectric barrier discharge in air at atmospheric pressure: experiment and modeling European Physical*. Journal Applied Physics. 2009; 47 (2): p. 22810 - 22815.

18. Hallac A, Georghiou G and Metaxas A. *Secondary emission effects on streamer branching in transient non-uniform short-gap discharges* J. Phys. D: Appl. Phys. 2003; 36: p. 2498 - 2509.

19. Tran T N. *Surface discharge dynamics: theory, experiment and simulation*. PhD Thesis, University of Southampton, UK. 2010.

20. O'Sullivan F M. *A model for the initiation and propagation of electrical streamers in transformer oil and transformer oil based nanofluids.* PhD Thesis, MIT. 2007.

21. Lee S H, Lee S Y, Chung Y K and Park I H. *Finite-element analysis of corona discharge onset in air with artificial diffusion scheme and under Fowler-Nordheim electron emission.* IEEE Transactions on Magnetics. 2007; 43: p. 1453 - 1456.

22. Georghiou G E, Morrow R and Metaxas A C. *An improved finite-element flux-corrected transport algorithm*. Journal of Computational Physics. 1999; 148: p. 605 - 620.

23. Boris J and Book D. *Flux-corrected transport. iii. minimal-error FCT algorithms.* Journal of Computational Physics. 1976; 20: p. 397 - 431.

24. Davies A, Evans C and Jones F. *Electrical breakdown of gases: the spatiotemporal growth of ionisation.* In fields distorted by space charge Proceedings of the Royal Society of London. 1964; 281 (A): p. 164 - 83.

25. Tanaka M, Murooka Y and Hikada K. *Nanosecond surface discharge development using the computer simulation method*. J. Appl. Phys. 1987; 61 (9): p. 4471 - 4478.

26. Georghiou G. *Gas discharge modelling using the finite-element flux-corrected transport method.* PhD Thesis. University of Cambridge, UK. 2000.

27. Dhali S and Williams P. *Two-dimensional studies of streamers in gases.* J. Appl. Phys. 1987; 62 (12): p. 4696 - 4707.

28. Vitello P, Penetrante B and Bardsley J. *Simulation of negative streamer dynamics in nitrogen*. Phys. Rev. E. 1994; 49 (6): p. 5574 - 5598.

29. Allen N and Mikropoulos P. *Streamer propagation along insulating surfaces.* IEEE Transactions on Dielectrics and Electrical Insulation. 1999; 6 (3): p. 357 - 362.

The impact of biorhythms in safety management in Vietsovpetro

Tran Hong Phong
Joint Venture "Vietsovpetro"

Research in rhythmic cyclic space science has proved that (suggested that) each person is born with a particular biological cycle, based on their birth date. The rhythm of physical, intellectual or emotional exercise of each person will continuously cycle, and , and that is their biorhythm.

Biorhythms are physiological cycles or intrinsic activity of living organisms in cycle time. Professor Whilliam Fliess, a German, plotted the outbreak of fever in children and confirmed the existence of cycles 23 and 28 days in the health of his patients.

In the 1920s, Dr. Alfred Teltscher observed cyclic fluctuations in terms of the intellectual energy of his students in 33 day cycles. Many subsequent studies have concluded a similar 33 day intellectual cycle. Studies during the 40s and 50s of the last century have shown that there is an increased tendency for accidents and mistakes at work due to human factors to coincide with lows in the biological cycle.

According to official statistics, in 2011, Vietsovpetro had 3639 employees working on offshore facilities, mainly divided into 2 shifts, in the fields of: drilling, exploration, construction and installation, mechanical and electrical operations. Most have to work in heavy conditions, mainly exposed to metal, metallic skids, piping and hazardous gases on vessels working under pressure. The primary jobs are transportation, installation, repair, welding and cutting, operation of mechanical equipment, electrical appliances, marine transport and diving work.

In the context of the marine environment, with waves and often fierce winds, people are very small and fragile. In harsh working conditions, requiring high levels of concentration, well organized labor and skilled workers, and accidents often occur unexpectedly. Accidents within Vietsovpetro, from inception to date, occur every year in spite of increasingly effective safety policy (Table 1). However, there are other factors affecting safety which have not been fully taken into account. One of these is the biorhythm. To clarify this issue, we need to point out the influence of biorhythms in risk management to work out synchronic solutions for controlling risks proactively and effectively.

In 2011, a total of 3639 Viesovpetro employees worked offshore. Thus, the number of employees at the same shift time working offshore is around 3639/2 = 1819.5 people. To calculate the risk caused by biorhythm, the average number of those people who have the same birthday should be calculated:

$$1819.5 : 365 = 4.98 \approx 5 \text{ persons/day}$$

The authors do not have research data on the law of distribution of birth dates of employees, so they assume

Table 1. *Statistics of accidents at work in Vietsovpetro*

Year	Number of employees involved	Year	Number of employees involved	Year	Number of employees involved	Year	Number of employees involved
1983	05	1991	26	1999	16	2007	08
1984	14	1992	25	2000	18	2008	02
1985	10	1993	23	2001	14	2009	03
1986	17	1994	24	2002	16	2010	06
1987	32	1995	27	2003	15	2011	03
1988	19	1996	19	2004	13		
1989	23	1997	10	2005	12		
1990	24	1998	11	2006	13		

Source: Vietsovpetro J.V.

in this case that birth dates are evenly distributed. If there are official figures that show a different distribution rule then will be adjusted later.

Thus, in the offshore fields of Vietsovpetro, a daily average of 5 persons have the same lowest biorhythm. Characteristic of low biorhythms are a lack of concentration and depression but not illness.

Risk probability of individuals working 2 shifts at workplaces are:

$$2.3148 \times 10^{-5}$$

Probability of risks on the biorhythm of offshore facilities works:

$$1.13425 \times 10^{-4}$$

This is the probability of risks occurring due to random factors, it is small enough to be considered safe if the job is normal without demanding a high concentration.

In Vietsovpetro, the job scale is normally large volume and high complexity, and to coordinate various parts the "Organizational - Technical Measures "(OTM) must be made in which assignment of teams and labor groups have already taken account of the safety factor. For work in which volume is smaller than the above mentioned, job safety analysis (JSA) is necessary to be undertaken and implemented. So that, we should know what extent of work is necessary to perform safety analysis to minimize risks to the labor collectively by human factors.

The probability of biorhythm risk when employees need the time to focus their attention on peforming jobs:

$$1.13425 \times 10^{-4} \times 30 = 3.47222 \times 10^{-3}$$

This probability is greater than "As Low As Reasonable Possibility" (ALARP) that has affected safety when performing work. According to the statistics law of large numbers, that probability shows that *it* ***is likely that four accidents or incidents caused by biorhythm will occur in 3 years***. This limit is dangerous.

To minimize the risk caused by biorhythms, we first need to define the offshore work in which continuous high concentration is necessary for over 30 seconds. That would include: moving goods by crane, piping assembly, welding and cutting, repair of technological equipment, piping string operations in drilling, well work-over etc. just to mention some typical and regular working tasks. In fact, even when performing work under the OTM,

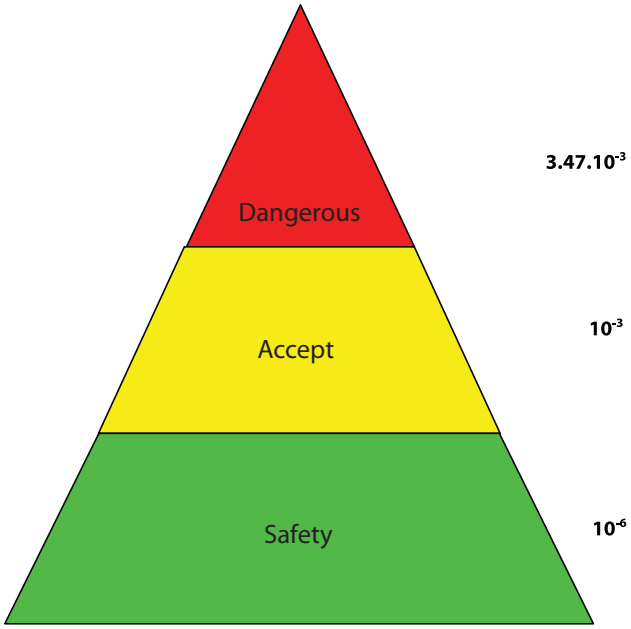

there is also a need to identify the small parts of jobs needing high concentration before proceeding. On the other hand, workers should also have good physical and daily activities as a healthy lifestyle is less affected by bio rhythms. For leadership necessary to divide the work needed to coordinate precision and high concentration over 30 seconds of workers into the small and otherwise, perform each task individual serial.

In addition to biorhythms, the risk is of course effected by many other factors that we have incorporated into solutions in order to achieve impressive results in recent years.

Reality has proven that complete safety from accidents and incidents in the E&P industry is rare and very fortunate achieved. (Vietsovpetro had reached 2 for 2008 with probability of occurrence 0.08). This additional risk identified by the biorhythm is a complementary solution to achieve an even greater result in the future.

For sustainable development, the slogan "Safety first" should be instilled into all and become the safety culture of Vietsovpetro. We have hopes in the near future, it will be achieved with no accidents, incidents (with probabilities of occurrence about 0.003 - 0.006) and continously ten million injury-free labor hours.

PETROVIETNAM NEWS

Vietnam, Peru, Venezuela boost energy cooperation

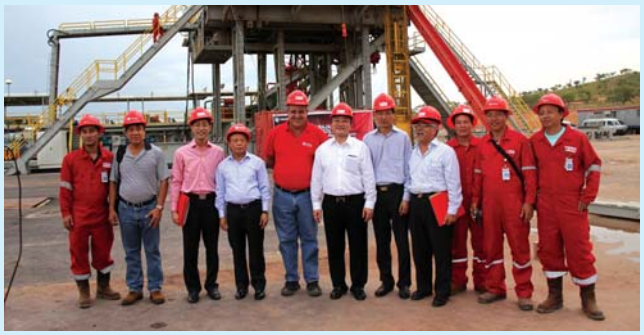

The Deputy Prime Minister Hoang Trung Hai and other senior officials of the two countries witnessed the first drill of Petromacareo's drilling platform PDV-39. Photo: PVEP

In his official visit to the Republic of Peru, the Deputy Prime Minister Hoang Trung Hai placed emphasis on increasing cooperation in the field of oil and gas. On 16 April, he met with the leaders of Peruvian National Oil Company (Perupetro), the partner of Petrovietnam/PVEP in the petroleum contracts for blocks Z47 of offshore Peru and 162 of onshore Peru. Perupetro President & CEO briefed the Vietnamese government leader and his high ranking delegation on the Peruvian oil and gas industry. He highly appreciated the investment activities by Petrovietnam in Peru. Particularly, he thanked the Government of Vietnam for supporting the development of oil and gas cooperation between the two countries.

The Deputy Prime Minister Hoang Trung Hai stressed that economic cooperation, particularly in the oil and gas industry, will lay a long term and solid foundation for Vietnamese and Peruvian bilateral relationships. He, therefore, urged the two oil and gas industries to further strengthen ties and support each other in further expanding petroleum activities into other projects. During this visit, the Deputy Prime Minister met with leaders of two leading petroleum companies in Peru, Perenco of England and Repsol of Spain, who have been working with Petrovietnam/PVEP in other projects in Peru. The Deputy Prime Minister took this occasion to visit PVEP Peru, a member company of PVEP.

After the successful visit to Peru, the Deputy Prime Minister Hoang Trung Hai continued his trip to Venezuela, attended the 2nd meeting of the Vietnam - Venezuela Inter-governmental Committee. On this occasion, the Deputy Prime Minister Hoang Trung Hai and other senior officials of the two countries witnessed the first drill of Petromacareo's drilling platform PDV-39 (a joint venture between PVN/PVEP and PDVSA). The platform is located at Block Junin 2 in Eastern Venezuela's Orinoco River Delta, 800km away from the Venezuelan capital of Caracas. Dr. Do Van Hau - President & CEO of Petrovietnam said at the event: "It is estimated that next year PDV-39 platform will produce some 7,000 barrels of heavy crude oil per day, whereas Block Junin 2 will reach a total output of more than 200,000 barrels or 10 million tons of crude oil per day".

Thu Huong

Load out and sail-away ceremony for Te Giac Trang field H4 topsides

Recently, the Petroleum Equipment Assembly & Metal Structure Joint Stock Company (PVC-MS), in its role as main contractor and investor Hoang Long JOC held the load out and sail-away ceremony for Te Giac Trang field H4 topsides, at PVC-MS Port in Vung Tau.

Te Giac Trang field H4-Wellhead platform topsides is invested in by Hoang Long JOC. It is the first EPCI contract of PVC-MS, with a capital of over 44.4 million USD, and commenced on 4th July 2012. H4 topside has a total weight of structures, systems and equipments of about 2,000 tons. The content of the contract includes design, construction, procurement of part of equipment and materials, fabrication, installation, pre-trial operation, loading out, fastening, sailing away, connection for operation, trial operation, checking and handing over.

Te Giac Trang field H4 topsides has been launched successfully. Photo: PVC

With the determined instructions and close attention of Petrovietnam and with tireless efforts, creativeness, and knowledged of H4 Project Management as well as of PVC-MS and Hoang Long JOC, the project completed construction onshore 20 days ahead schedule, saving several USD millions.

Minh Phuong

World Gas Conference 2012:
Gas sustaining future global growth

Dr. Do Van Hau had bilateral meetings with leaders of many international oil companies. Photo: PVN

The mission of Vietnam Oil and Gas Group (Petrovietnam) led by Dr. Do Van Hau - President & CEO of Petrovietnam attended the 25th World Gas Conference (WGC) 2012 in Malaysia from 4th to 6th June. Hosted by Petronas and organized by the International Gas Union (IGU), the WGC conference and exhibition has become the most important international meeting of the sector, with the aim to establish the pathway to a sustainable energy future.

Themed "Gas: Sustaining Future Global Growth", the 25th World Gas Conference 2012 showcased major achievements and milestones accomplished by the global gas industry. It also draws on critical inputs from an array of global gas professionals to chart new strategies for the natural gas industry. Dr. Abdul Rahim Hashim, IGU's President (2009 - 2012), said, "Natural gas has a key role in achieving a low carbon economy. The credentials of natural gas are indisputable. Supply security is no longer an issue with the abundance of both conventional and unconventional gas and globalization of the LNG trade. Yet, natural gas faces challenges and obstacles in positioning itself as a key energy source, particularly in the policy arena. As the spokesperson for the gas industry, IGU has initiated efforts towards advocating natural gas, so that it will regain its appropriate policy voice, consistent with its merits and potential".

In addition, Petrovietnam's President & CEO had bilateral meetings with Mr. Datuk Shamsul Azhar Abbas - Petronas's CEO; Ms. Melody Meyer - President of Chevron Asia Pacific Exploration and Production Company; Mr. Alexey Miller - Chairman of Gazprom; Murphy Oil's CEO Roger Jenkin and ExxonMobil's Director General Tom Walker...

Pham Xuan

FSO PTSC Bien Dong 01 keel-laying ceremony

Petrovietnam Technical Services Corporation (PTSC) and PVN's subsidiary - Bien Dong Petroleum Operating Company (Bien Dong POC) - held the keel-laying ceremony for the FSO PTSC Bien Dong 01 on 30th May 2012, in Korea. FSO PTSC Bien Dong 01 - with the capacity of 350,000 barrels - is the sixth FSO/FPSO that PTSC invested and the first FSO ever to be new built by PTSC from the engineering, construction supervision, transportation, installation and commissioning to operational stages. The engineering, construction supervision at Sungdong Shipyard has been performed by PTSC's skillful, experienced engineers and executives, strictly in accordance with the standards of international classification society ABS.

The keel-laying ceremony was on-schedule and marked a remarkable milestone of the FSO PTSC Bien Dong 01 project promising the on-schedule vessel hand-over at the year end of 2012. FSO PTSC Bien Dong 01 willl operate in Hai Thach - Moc Tinh condensate field, block

The keel - laying ceremony for the FSO PTSC Bien Dong 01. Photo: PTSC

05.02, 05.03 in the Nam Con Son Basin, offshore Vietnam; and about 340km Southeast of Vung Tau. The keel-laying ceremony saw presences of many leaders, representatives from Vietnam Register, PetroVietnam Technical Services Corporation, Bien Dong Petroleum Operating Company and Sungdong Shipyard.

Do Khanh

PVEP expands operations in South America

The Petrovietnam Exploration and Production Corporation (PVEP) has expanded its presence in South America by acquiring over 50 percent of a project to explore for oil in Peru, from the London based oil and gas company Perenco SA. PVEP and Perenco SA signed the deal for 52.6 percent of Block 67 in London on June 21. This brings the number of exploration projects which PVEP has in overseas markets to 19 so far.

PVEP and Perenco SA signed the deal for 52.6 percent of Block 67 in London on June 21. Photo: PVEP

When speaking at the signing, Jean Michel Jacoulot, Perenco's CEO, said that he hopes the joint operation will be the first of many between the two companies. As he congratulated his new partners PVEP, he added that he is impressed with PVEP's previous operations and he has a high regard for the company's specialists, technicians and workers. "We found a good partnership can be established", he said. Jacoulot also said he hopes that the first oil will flow from Block 67 by the middle of next year.

The President & CEO of PVEP, Dr. Do Van Khanh, said that the expansion of PVEP's operations in the South American country played an important role in its strategy to reach out further into overseas markets. The output of oil from this project will help to ensure national energy security, he said.

Currently, PVEP, one of Petrovietnam's key companies, has 44 domestic projects in operation and 19 overseas in 15 countries around the world.

Ha Phong *(VNA)*

PTSC and Lam Son JOC signed contract to supply FPSO

The vessel will have a designed capacity of storing at least 350,000 barrels of crude oil and processing 18,000 barrels per day. Photo: PTSC

Petrovietnam Technical Services Corporation (PTSC) has just signed a contract to supply a floating production, storage and offloading (FPSO) vessel for the Thang Long - Dong Do field development project with Lam Son Joint Operating Company (Lam Son JOC). The vessel will have a designed capacity of storing at least 350,000 barrels of crude oil and processing 18,000 barrels per day and non-docking for more than 10 years at field. When completed, this vessel shall be one of the highest - technology FPSO in Vietnam. The vessel is tentatively scheduled tol receive its first oil at the year end of 2013.

Mr. Nguyen Hung Dung - General Director of PTSC emphasized that this contract "again re-affirms Petrovietnam's development strategy in stransforming PTSC to a leading oil and gas services provider not only for the Vietnamese market but also overseas, especially in the field of offshore floating facilities named FSO, FPSO and MOPU accordingly". Mr. Dung added, "It requires our merged spirit of fulfilling and meeting the timeline of the project and ensuring all standard operating procedures and quality services. That contributes an effort into production performance, ensures national energy as well as pushing up the economical effectiveness of PTSC and partners".

Khanh Linh

DQS organized inauguration and delivery ceremony of the 104,000 DWT crude oil tanker

PVT Mecury is one of the largest obtained by PVTrans. Photo: DQS

After completion of building the vessel, on 3rd June 2012, Dung Quat Shipyard (DQS) together with ship Owner PVTrans organized inauguration and delivery ceremony of the 104,000DWT crude oil tanker, PVT Mercury. It is one of the largest obtained by PV Trans with a length of 245m, width of 43m, height of 20m, draft of 11.7m and speed of 14.7 nautical miles/hour. The ship's average speed is 15 knots per hour. This vessel specializes in crude oil transportation with the largest tonnage ship built in Vietnam.

The 104,000DWT crude oil tanker is the first big deadweight ton, as well as most modern vessel constructed in Vietnam. This newbuild required a great deal of precision engineering and complicated equipment installation as well as skillful labor and high technology to be applied in its construction. According to DQS, the 104,000DWT sea trial vessel was under supervision, monitoring, inspection of DQS, ship owner and ABS Registry. All specifications of PVT Mercury vessel have been tested with more than 20 items of technical requirements such as main engine system, generators, air navigation facilities, electrical systems, steering system, control room, signal system and ballast pump...

Tran Minh

Successful load-out Vietnam's largest jacket

Vietsovpetro Joint Venture (Vietsovpetro) has successfully performed the load-out of the Hai Thach jacket to the barge by the skidding method. The Hai Thach jacket is the largest and deepest jacket in Vietnam ever made by Offshore Construction Division, installed in 131m deepwater it has a length of 140m and weighs 7,500 tons, beating the record of the Moc Tinh jacket (6,500 tons). Hai Thach jacket was completely fabricated onshore ahead of the assigned schedule, satisfying safety, quality, and contributing to cost reduction and time savings for the investor and construction unit.

Hai Thach jacket is the largest and deepest jacket in Vietnam. Photo: VSP

Khanh Ha

Major equipment contract for thermoelectricity plant signed

A contract for the design and supply of equipment and technological services for the Thai Binh 2 Thermoelectricity Plant Project was signed between the Petrovietnam Construction Joint Stock Corporation (PVC) and the Sojitz-Daelim contractors (SDC). The contract included equipment supply and a detailed design for the turbine and generator areas. It also gave technical consultancy and guidance for the equipment installation and pilot operation. The Thai Binh 2 Thermoelectricity Plant, with the capacity of 1,200MW and a total investment of 1.6 billion USD, is expected to commence operation in 2015 with output of about 6.7 billion kWh per year.

Thu Huong

OIL & GAS GLOBAL MARKET

Oil prices

Global oil and gas production in the first half of 2012 remains approximately at the same level as in 2011 and the supply - demand balance fluctuation depends mainly on the tension in the Middle-East region but the market looks to have been sufficiently stable.

Spot prices for dated Brent crude oil averaged $109/bbl during the fourth-quarter of 2011 and increased to $118/bbl during the first-quarter of 2012. Spot prices for dated Brent increased by about $15/bbl during the first-quarter of 2012 and averaged $125/bbl in March. Prices began to weaken in April and the slide accelerated during May. At June 16, 2012 it remains at $96/bbl only. Although the slow-down in the oil price trend is evident, many analysts believe that this event is not stable.

According to statistics published by the US Commodities Futures Trading Commission (CFTC) for 68 - 73% of total open interest in the NYMEX crude oil futures contract during the fourth-quarter of 2011 and the first-quarter of 2012, large traders in the managed money category boosted net-long positions (holding of long contracts minus short contracts) to a peak of 228,000 contracts in last February from 126,000 contracts in early October 2011. The 81% increase in net long positions by managed money accounts coincided with a $28/bbl increase in WTI and $20.68/bbl increase in dated Brent spot prices.

Crude oil production was disrupted by military conflicts in Syria and Yemen during the fourth-quarter of 2011 and into the first-quarter of 2012. Political tensions between Iran, the US and major European countries resulted in the embargo of crude oil imports from Iran. The embargo was officially scheduled to begin in June but Iran announced its decision to discontinue crude oil sale to European countries immediately. The early loss of Iranian crude oil supplies into the European markets also contributed to a tightening supply-demand balance and bullish pressure on crude oil prices. The price increases of 20 - 30% during fourth-quarter of 2011 and the first-quarter 2012 is also due to economic growth in Europe, the US, China and the Japan disaster and the cold season. The global economic recession and other negative factors caused the slow-down of the oil prices at the present time. If the tensions between opposed countries increase and OPEC cuts production to prevent oil prices from falling too low during the third quarter of 2012, these events will have a marked influence on the oil price development in the fourth-quarter 2012.

Gas development

As is well known, before 2000, the main gas reserves of our planet are located in Russia, the Middle-East, the US and this category of energy develops rapidly.

Recently, beside the US shale oil-gas development which radically transforms the scientific concepts concerning natural gas in the world, there is another potentially large source of supply from Eastern African countries and China.

In Mozambique, Sasol Petroleum International has started up its 63 million gigajoule/year (158/MMscfd) expansion at the Temane gas processing plant. Capacity now is 458MMscfd. The gas plant has begun full-scale production and is connected to the South African market via a 865km cross border pipeline. In the Asia-Pacific region, until the end of 2010, the cumulative proved gas

reserves of China were 1,544Tcf; the cumulative gas production was 282.7Tcf, the remaining gas reserves were 1,261.5Tcf and the reserves/production ratio was 4:1. The total undiscovered recoverable gas resources of China are in the range of 756.3 - 1,307.5Tcf, with a mean of 990Tcf. At the end of 2030 the cumulative proven degree of gas resources will be 42% in this country.

In ASEAN countries, Petronas makes FID (final investment decision) for liquefaction off Sarawak. A second project to build a floating natural gas liquefaction facility has received approval.

Australia's coal seam gas and China's shale gas resources hold great promise for future global gas supplies.

While there is no doubt these abundant gas reserves around the world can be tapped, operators should not underestimate the substantial investment and highly complex technology required to do so in a safe and responsible way.

The growth in oil and gas production from shale plays in recent years in the US is spectacular. US companies hope to sell US gas to higher-price markets elsewhere beside exporting to Europe. Recent US prices are less than $3/MMBtu while Asian LNG prices are at 4-year highs of about $18/MMBtu.

World crude oil prices

OPEC reference basket wkly.avg. June 1, 2012: 97.44$/bbl

Crude oil	March 11- $/bbl	April 12/2012 - $/bbl
OPEC reference basket	122.97	118.18
Arabia light - Saudi Arabia	123.43	118.94
Basrah light - Iraq	121.96	116.26
Bonny light 37° - Nigeria	127.98	122.36
Es Sider - Libya	126.03	120.71
Girassol - Angola	126.30	121.32
Iran heavy	122.46	117.78
Kuwait export	122.32	117.53
Marine - Qatar	122.80	117.39
Merey - Venezuela	112.07	108.62
Murban - UEA	125.61	120.44
Oriente - Ecuador	118.26	118.86
Saharan blend 44° - Algeria	126.13	120.81
Minas 34°- Indonesia	133.85	130.15
Fateh 32° - Dubai	122.47	117.30
Brent 38° - UK	120.46	116.04
Isthmus 38° - Mexico	118.41	114.07
Tia Juana light 31° - Venezuela	125.33	119.71
Urals - Russia	122.41	117.69
Differential		
WTI/Brent	-19.02	-16.36
Brent/Dubai	2.86	2,41

Source: OPEC Monthly Oil Market Report

Nymex us gas futures

Contract month	June 4 - $/MMBtu	May 25 - $/MMBtu
July 2012	2.415	2.627
August	2.467	2.678
September	2.512	2.718
October	2.601	2.789
November	2.846	3.001
December	3.144	3.281
January 2013	3.293	3.430
February	3.313	3.443
March	3.292	3.416
April	3.280	3.386
May	3.316	3.416
June	3.361	3.461

Source: OGJ June 16, 2012

Spot LNG exporter netbacks at key markets worldwide

Netback in $/MMBtu Exporters	North East Asia	South West Europe	UK (WGI NBP spot price as.)	Belgium
Qatar	15.59	10.80	5.39	5.49
Oman	15.81	10.50	5.73	5.66
Abu Dhabi	15.64	10.35	5.49	5.53
Indonesia	16.94	9.33	4.57	4.30
Malaysia	16.88	9.43	4.69	4.78
Australia	16.61	9.27	4.56	4.48
Russia	17.59	8.73	4.10	4.19
Trinidad	13.05	11.18	6.35	6.40
Algeria	14.06	12.13	6.92	6.97
Egypt	14.64	11.67	6.52	6.62
Nigeria	14.01	11.12	6.22	6.27
Eq.Guinea	14.10	11.19	6.25	6.34

Source: WGI June 6, 2012

Vietnam fertilizer market

Category	Price	On
Urea granular	FOB - $/ton	June 15, 2012
Urea Baltic	410 - 430	
Urea Yuzhny	410 - 430	
Southeast Asia	480 - 490	
China	460 - 470	
Urea opaque particles	FOB - $/ton	June 15, 2012
Southeast Asia	460 - 470	
China	465 - 475	
Domestic	VND/kg (1$ = 20,000VND)	June 15, 2012
Phu My fertilizer	11,300	
Urea China	11,300	
DAP China (brown)	14,400	
Kali Russia	12,300	
NPK Philippines	11,800	

Source: Vietnamnet.vn June 15, 2012

Ha Phong

VIET NAM MARITIME COMMUNICATION AND ELECTRONICS LLC

Add: No 2, Nguyen Thuong Hien Street, Hong Bang District, Hai Phong City– Tel: 84.31.3746 464 – Fax: 84.31.3747 062
Email: contact@vishipel.com.vn – Website: www.vishipel.com.vn

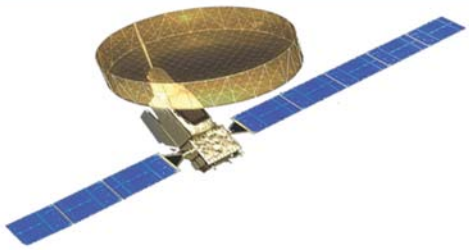

VISHIPEL

inmarsat
Distribution Partner

Viet Nam Maritime Communication and Electronics Single-Member Limtited Liability Company (VISHIPEL), Inmarsat Silver partner, is Vietnam's leading supplier of satellite service with the main activities:

inmarsat Silver SERVICE PROVIDER

Provide satellite telecommunication services and equipments: Fleet Broadband(FBB), BGAN, Isatphone Pro, Fleet phone, Isatphone Link, VSAT...

Consult, install, maintain and repair of communication equipment, navigation equipment.

An Accounting Authority with code VT02 - VISHIPEL offers the international accounting service VT02 for customers in Maritime Industry

A Point of Service Activation (PSA) for inmarsat service VISHIPEL provide and manager MMSI, IMN.

RESEARCH AND DEVELOPMENT CENTRE FOR PETROLEUM SAFETY AND ENVIRONMENT (CPSE)

Head office:
G1, Thanh Da Hotel, Ward 27, Binh Thanh District, Hochiminh City, Vietnam
Tel. 84 8 35566075 Fax. 84 8 35566076 Email. cpse@vpi.pvn.vn
Website: http://www.cpse.com.vn

Solution for Sustainable Development

Safety

- Safety management and reliability of industrial equipment
- Researching, surveying, and assessing occupational health and safety
- Consultancy in establishing and getting certificates for HSE management system
- Non-destructive testing (NDT)

Environment

- Preparing reports of Environmental and Social Impact Assessment (EIA, ESIA)
- Establising reports of Oil Spill Response Plan (OSRP)
- Establishing Environmental Sensitivity Map
- Performing programs of environmental monitoring-surveys, samplings, analysis and assessment
- Ecotoxicological testing for industrial chemicals and wastes
- Advising, designing and installing waste treatment systems
- Other specialized environmental researches and analyses

VIETNAM PETROLEUM INSTITUTE

Research & Development Center for Petroleum Processing

Director: MSc. Phan Minh Quoc Binh

- Formulate strategies and master plans for the development of petroleum processing and petrochemicals;
- Formulate, consult and appraise market studies, potential reports, pre-FSs, FSs for refineries, petrochemical complexes and gas processing plants;
- Conduct scientific and technological research for the implementation of refining, petrochemical and gas processing projects (selection of technologies, feedstocks, managerial, technical and technological solutions for operation and maitanance);
- Simulate, optimize process operation; study scientific-technological and energy saving solutions to improve the economical efficiency for operating oil and gas processing plants;
- Research for the production of new, alternative, clean energy forms; Study on the new products from oil and gas resources.

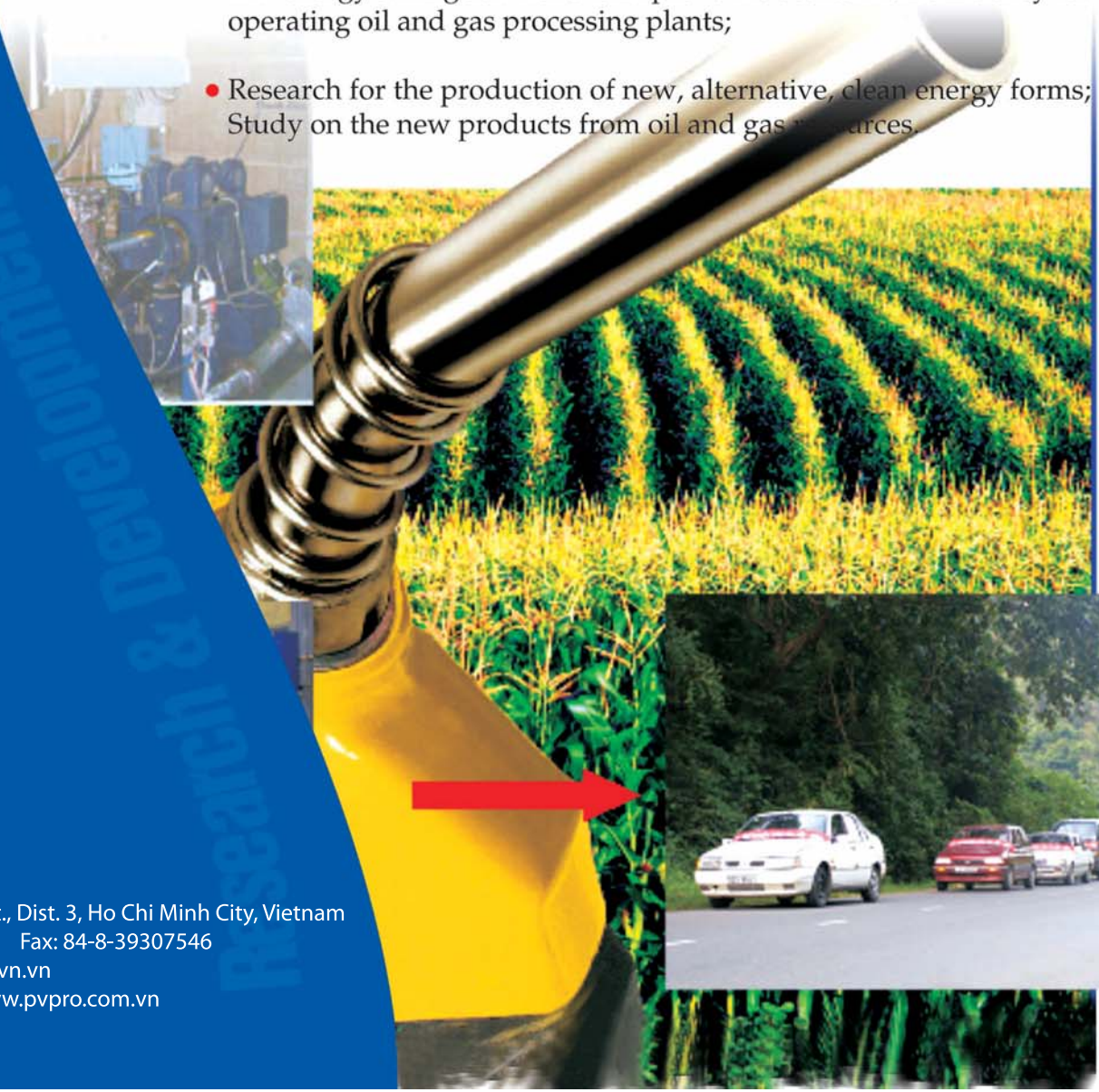

Head office:
4 Nguyen Thong St., Dist. 3, Ho Chi Minh City, Vietnam
Tel: 84-8-39303323 Fax: 84-8-39307546
Emal: pvpro@vpi.pvn.vn
Website: http://www.pvpro.com.vn